Frequency-domain design for non-conventional Active Vibration Control

Kaczmarek, M.B.

Important note
To cite this publication, please use the final published version (if applicable).
Please check the document version above.

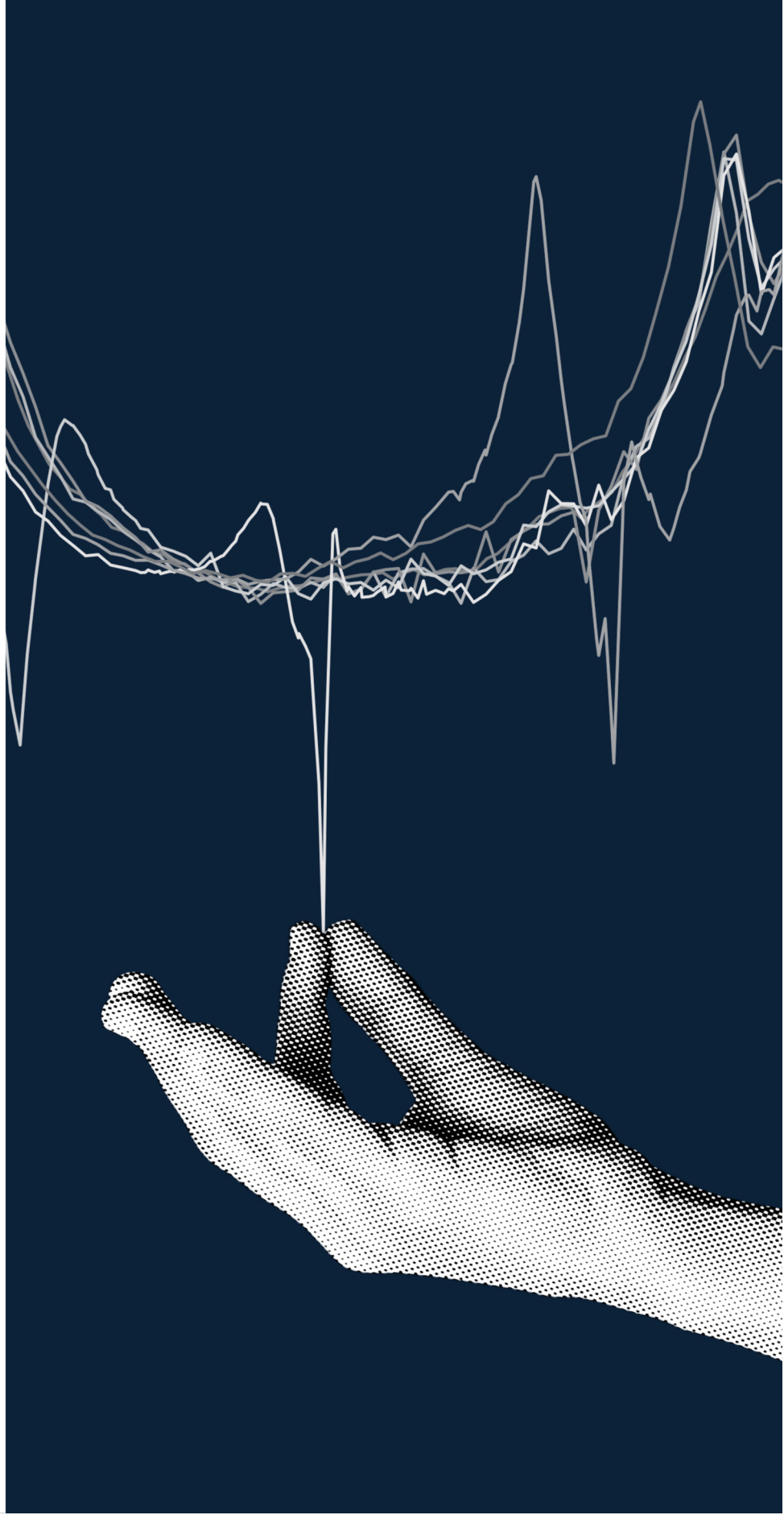# Frequency-domain design for non-conventional Active Vibration Control

Marcin Brunon Kaczmarek

Frequency-domain design for non-conventional

Active Vibration Control

Frequency-domain design for non-conventional

Active Vibration Control

Dissertation

for the purpose of obtaining the degree of doctor
at Delft University of Technology,
by the authority of the Rector Magnificus Prof.dr.ir. T.H.J.J. van der Hagen,
chair of the Board for Doctorates,
to be defended publicly on
Friday 13 June 2025 at 12.30 o'clock.

by

Marcin Brunon KACZMAREK

Master of Science in Mechanical Engineering
and
Master of Science in Systems and Control,
Delft University of Technology, The Netherlands,
born in Poznań, Poland.

This dissertation has been approved by the promotors.

Composition of the doctoral committee:

Rector Magnificus,	Chairperson
Dr. S.H. Hossein Nia Kani,	Delft University of Technology, promotor
Prof.dr.ir. J.L. Herder,	Delft University of Technology, promotor

Independent members:

Prof.dr. V. Feliu Batlle,	University of Castilla-La Mancha
Prof.dr. M. Ghandchi Tehrani,	University of Groningen
Prof.dr.ir. W.B.J. Hakvoort,	University of Twente
Prof.dr. I. Podlubný,	Technical University of Košice
Prof.dr.ir. J.W. van Wingerden,	Delft University of Technology

TUDelft
Delft
University of
Technology

All models are wrong, but some are useful.

Contents

Summary

Vibrations deteriorate the performance of machines and instruments, especially when high precision and efficiency are required. Multiple approaches for vibration mitigation exist, mostly constituting separate bodies of research. This thesis establishes a connection between the active vibration control practice, advances in other control fields, and metamaterials research. To this end, three research gaps are addressed.

First, in Chapter 2, the design requirements of active vibration control are expressed in the frequency domain, using the loop-shaping approach commonly used in motion control. The use of the proposed approach is shown in the experimental evaluation of a vibration isolation system based on piezoelectric stack actuators.

Second, the loop-shaping approach is related to the design for bandgap in active metastructures. Chapter 3 adopts a modal analysis approach for finite metamaterial beams, relating the underlying control problem to the active damping of a single-degree-of-freedom system by assuming an infinite number of infinitesimally small transducer pairs distributed along a beam. This allows the application of design methods developed in the preceding chapter. The experiments demonstrate that controllers initially developed for damping resonance peaks can effectively induce bandgaps, even in structures featuring a small number of sparsely placed transducer pairs. Chapter 4 studies when the obtained models and approximations are accurate, highlighting the correlation between the minimal number of transducers required for model accuracy and the dominant vibration mode within the controller's targeted frequency range.

Third, the frequency-domain approach is applied for the design of fractional order and reset controllers for vibration mitigation to relax the limitations imposed using low-order linear controllers. In Chapter 5, a design for a fractional-order resonant element tailored for AVC, which preserves the characteristics of its integer-order counterpart but provides greater design freedom, is presented and evaluated in a simplified vibration isolation system. In Chapter 6, the same element is implemented within a unit cell of a granular metamaterial. For such a fractional-order metamaterial, both the dispersion characteristics of the infinite structure and the transmissibility of a finite chain are presented.

The use of nonlinear elements, like reset systems, poses additional challenges in vibration control. Since an exact frequency-domain representation of such elements does not exist, their behaviour is approximated using the describing functions. While this enables the loop-shaping design, the describing function approximation does not represent the system well in the presence of wide-band excitations and multiple resonance peaks in the plant. Chapter 7 explores how such conditions influence the reset elements and how to ensure that the use of reset is still beneficial. Additionally, assessing the stability of a reset system solely based on controller dynamics and experimentally measured plant frequency response is an open problem. To address this, the Negative Imaginary systems approach for stability analysis, originally developed for AVC of flexible systems with uncertain dynamics, is extended to reset systems in Chapter 8.

Samenvatting

Trillingen verslechteren de prestaties van machines en instrumenten, met name wanneer hoge precisie en efficiëntie vereist zijn. Er bestaan meerdere benaderingen voor het reduceren van trillingen, die grotendeels afzonderlijke onderzoeksgebieden vormen. Dit proefschrift legt een verband tussen de praktijk van actieve trillingsonderdrukking, ontwikkelingen in andere controlegebieden en onderzoek naar metamaterialen. Hiertoe worden drie onderzoekshiaten behandeld.

Ten eerste worden in Hoofdstuk 2 de ontwerpeisen voor actieve trillingsonderdrukking geformuleerd in het frequentiedomein, gebruikmakend van de zogeheten loop-shaping methode, die gangbaar is in motion control. Het gebruik van de voorgestelde aanpak wordt aangetoond in de experimentele evaluatie van een trillingsisolerend systeem gebaseerd op piëzo-elektrische stapelactuatoren.

Ten tweede wordt de loop-shaping benadering gerelateerd aan het ontwerp van bandgaps in actieve metastructuren. Hoofdstuk 3 hanteert een modale analyse voor eindige metamateriaalbalken, waarbij het onderliggende regelprobleem wordt gerelateerd aan de actieve demping van een systeem met één vrijheidsgraad. Dit gebeurt onder de aanname van een oneindig aantal infinitesimaal kleine transducerparen, gelijkmatig verdeeld over een balk. Deze benadering maakt het mogelijk om de in het voorgaande hoofdstuk ontwikkelde ontwerpmethoden toe te passen. De experimenten tonen aan dat regelaars die oorspronkelijk zijn ontworpen om resonantiepieken te dempen, effectief bandgaps kunnen opwekken, zelfs in structuren met een beperkt aantal schaars geplaatste transducers. Hoofdstuk 4 onderzoekt onder welke omstandigheden de verkregen modellen en benaderingen nauwkeurig zijn. Daarbij wordt aangetoond dat er een verband bestaat tussen het minimale aantal transducers dat nodig is voor modelnauwkeurigheid en de dominante trillingsmodus binnen het beoogde frequentiebereik van de regelaar.

Ten derde wordt de frequentiedomeinaanpak toegepast bij het ontwerp van fractionele-orde- en resetregelaars voor trillingsreductie, met als doel de beperkingen van lineaire regelaars van lage orde te omzeilen. In Hoofdstuk 5 wordt een ontwerp gepresenteerd voor een resonantie-element van fractionele orde, specifiek afgestemd op actieve trillingsonderdrukking. Dit element behoudt de eigenschappen van zijn tegenhanger van gehele orde, maar biedt meer ontwerpvrijheid. De effectiviteit wordt geëvalueerd in een vereenvoudigd trillingsisolerend systeem. In Hoofdstuk 6 wordt hetzelfde element geïmplementeerd in een eenheidscel van een granulair metamateriaal. Voor dit fractionele-orde metamateriaal worden zowel de dispersiekenmerken van de oneindige structuur als de transmissie van een eindige keten geanalyseerd.

Het gebruik van niet-lineaire elementen, zoals resetregelaars, brengt extra uitdagingen met zich mee op het gebied van trillingsonderdrukking. Omdat er geen exacte representatie van dergelijke elementen in het frequentiedomein bestaat, wordt hun gedrag benaderd met behulp van beschrijvende functies. Hoewel dit het mogelijk maakt om ontwerp via loop-shaping toe te passen, geeft deze benadering geen nauwkeurige weergave van het systeem bij breedbandsignalen en meerdere resonantiepieken in het plantmodel. Hoofdstuk 7 onderzoekt hoe dergelijke omstandigheden de werking van reset-elementen beïnvloeden en hoe men kan waarborgen dat hun toepassing toch voordelen oplevert. Bovendien is het beoordelen van de stabiliteit van een resetsysteem op basis van enkel de dynamiek van de regelaar en experimenteel gemeten frequentierespons van het systeem nog een open vraagstuk. In Hoofdstuk 8 wordt hiervoor de zogeheten Negative Imaginary-

systeemtheorie, oorspronkelijk ontwikkeld voor de stabiliteitsanalyse van flexibele systemen met onzekerheden, uitgebreid naar resetsystemen.

1

Introduction

This chapter provides background on vibration control strategies, setting the stage for this work, and explores the problems related to active methods that motivated this research. Research gaps that will be addressed, as well as the aims of this work, are discussed together with the approach taken. Finally, the structure of the dissertation is outlined, showing how different chapters interrelate.

1

1.1 Background

Vibrations deteriorate the performance of machines and instruments, especially when high precision and efficiency are required [1]. Steady-state vibrations, caused, for example, by continuous floor vibrations transmitted through an instrument, reduce the achievable precision of positioning [2]. In consequence, they lead to blurry images created in microscopes [3] or deteriorate the operation of gravitational wave detectors and particle colliders [4]. Transient vibrations, caused, for example, by impact forces acting on a machine, often slow down system operations and lower productivity, as dwell intervals must be introduced for the excessive motions to settle [5]. In precision motion systems, the resonance peaks associated with vibration modes limit the maximal achievable bandwidths [6], which are closely related to systems performance.

If the vibration problems cannot be avoided, common practice is to incorporate passive components to mitigate them. To isolate the system from external disturbance, it can be placed on soft mounts [4]. Additionally, applying viscoelastic materials [7] in a component to boost damping levels or tuned mass dampers [8–10] to enhance energy dissipation at specific frequencies can effectively attenuate vibrations from both floor vibrations and forces acting directly on a structure and reduce the time needed for the vibrations to settle.

Unfortunately, passive solutions are not applicable in all situations. Moreover, passive damping in isolation systems can worsen disturbance transmission at higher frequencies. Most viscoelastic materials are only effective in attenuating vibrations at specific frequency ranges, and their efficacy is tied to the amount of added mass. The same applies to tuned mass dampers, making them challenging to implement in compact designs.

When passive methods are unsatisfactory, active vibration control (AVC) can be a solution [11]. A typical active system consists of a control unit that defines the influence of actuators on the object to attain desired behaviour based on measured signals. Unlike passive systems, the performance of such a system is not solely dictated by component size and placement but also by controller characteristics. This leads to greater design freedom and makes it possible to adjust controller parameters to suit specific circumstances.

While various AVC strategies have been a topic of active research [12], practical applications are predominantly limited to vibration isolation systems implemented as a standalone device or a mount connecting a subsystem to other machine components. The dynamics of such systems are characterized by a single dominant resonance peak, accompanied by some high-frequency modes, usually seen as parasitic dynamics. While these high-frequency dynamics strongly influence system performance, they can be neglected in the early design of the controller.

Beyond vibration isolation, integrating AVC solutions on a component level did not find a wider practical adoption. This is the case despite the availability of suitable transducers, like piezoelectric patch elements. The research on the topic did not extend beyond laboratory experiments and considered narrowly defined performance that does not align with industrial expectations.

Despite years of developments in the research on control, the majority of feedback controllers in the AVC systems are based on velocity feedback [13], possibly with additional bandpass filters. While reliable, this strategy limits the achievable performance. When the floor vibrations are the major concern in the system, their rejection can be significantly

improved using disturbance feedforward strategies [14]. This approach, however, is not effective in dealing with direct disturbances.

A fresh perspective on vibration control problems is offered by the research on metamaterials [15–17], precisely engineered to have properties rarely observed in natural substances. However, these new ideas were not translated into practice in the AVC context. One unique property developed in metamaterials is the ability to create bandgaps [15] – ranges of frequency where transmission of vibrations is prohibited. While the application of metamaterials in passive vibration isolation is a subject of ongoing research [17–19], the practical application of active metamaterials remains underexplored. Thanks to the special properties, metamaterial-inspired AVC systems could be an alternative to traditional vibration isolation techniques, offering the potential for compact integration into components.

1.2 Research gaps

The view on the AVC field presented above indicates an opportunity to establish a connection between the active vibration control practice, advances in other control fields, and rapid developments in metamaterials research, since the insights from those adjacent domains are not fully exploited. Bridging these gaps would allow us to advance beyond conventional active vibration control, integrate it within industrial components, and introduce new control approaches to this discipline.

The gaps to be bridged are illustrated in Fig. 1.1. Dotted lines illustrate connections that will not be explored here, as they have been sufficiently developed or are a topic of ongoing research. The solid lines show the ones addressed in this thesis, with the focus on feedback control techniques.

Firstly, to facilitate practical adoption, the design methods for AVC systems will be presented in line with the current industrial practice, where techniques based on frequency response measurements are used. To this aim, the AVC problem will be related to the results from motion control, a field more developed and widely adopted in practical applications. Traditionally, distinct design approaches are employed in these two fields. Motion control commonly relies on frequency-domain data-based design and loop-shaping techniques (e.g. [6, 43, 44]). In contrast, AVC design leans towards model-based methods such as pole placement (e.g. [11]). We propose to present both motion control and AVC in the same design framework so that insights from one can be used in the other.

Secondly, bridging the gap between AVC findings and research on active metamaterials will enable the use of insights from the control research for metamaterial design. Conversely, knowledge gained from metamaterial research on systems with multiple transducers could inform the advancement of over-sensing and over-actuation in motion control systems. Again, we propose using the frequency-domain approach, which aligns with industrial practice.

Third, we propose to develop a systematic approach to designing non-conventional AVC controllers. The constraints imposed by low-order linear controllers limit the design freedom. A potential solution involves investigating fractional-order controllers, offering greater design flexibility while retaining the advantages of linear control. Moreover, we propose to also explore other possibilities since all linear controllers are subject to limita-
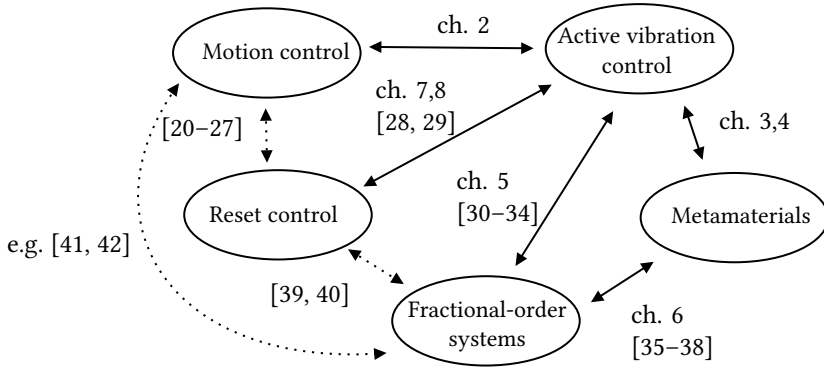
Figure 1.1: Illustration of the scope of this work in the context of research on motion control, active vibration control and metamaterials. Dashed lines indicate the relations not explored in this thesis.

tions stemming from the Waterbed effect and Bode's magnitude and phase relationship. An effective remedy lies in the adoption of reset systems, whose efficacy in alleviating such constraints has been demonstrated in motion control research (e.g. [20–24]).

1.3 Objective of this thesis

In this thesis, we propose to use the frequency-domain loop-shaping techniques to design feedback controllers in AVC systems and active metamaterials for bandgap generation. In this way, we make the rational design of unconventional, fractional-order, and reset controllers possible in AVC applications. As the dynamics of the studied nonlinear controller cannot be fully captured in the frequency domain, we develop tools for the design and stability analysis to complement the loop-shaping approach.

1.4 Outline

The objective is achieved by connecting pairs of studied fields one by one. The insights obtained this way are then synthesized in the concluding chapter of this thesis.

The first research gap is addressed in Chapter 2, where we relate the design requirements of active vibration control to the loop-shaping used in motion control. This chapter is written in a tutorial style and presents an approach used in the rest of the thesis. Simple mass-spring-damper systems are considered, and the desired loop shapes for AVC are defined. We show the use of the proposed approach in the experimental evaluation of a vibration isolation system based on piezoelectric stack actuators.

The second research gap is tackled in Chapters 3 and 4, where our focus is creating bandgaps in continuous structures utilising piezoelectric patch sensors and actuators to implement resonant dynamics within the feedback loop actively. In Chapter 3, we adopt a modal analysis approach for finite metamaterial beams, relating the underlying control problem to the active damping of a single-degree-of-freedom system by assuming an infinite number of infinitesimally small transducer pairs distributed along a beam. This allows the application of design methods developed in the preceding chapter. Moreover,

we demonstrate experimentally that controllers initially developed for damping resonance peaks can effectively induce bandgaps, even in structures featuring a small number of sparsely placed transducer pairs. Chapter 4 studies when the obtained models and approximations are accurate, highlighting the correlation between the minimal number of transducers required for model accuracy and the dominant vibration mode within the controller's targeted frequency range.

The third research gap is addressed in Chapters 5, 6, 7, and 8, focusing on two categories of non-conventional systems. Leveraging insights from the loop-shaping design method established in Chapter 2, we introduce a design for a fractional-order resonant element tailored for AVC, which preserves the characteristics of its integer-order counterpart but provides greater design freedom. Chapter 5 evaluates its use in a simplified vibration isolation system. In Chapter 6, the same element is implemented within a unit cell of a granular metamaterial. For such a fractional-order metamaterial, we study both the dispersion characteristics of the infinite structure as well as the transmissibility of a finite chain.

The use of nonlinear elements, like reset systems, poses additional challenges in vibration control. Since an exact frequency-domain representation of such elements does not exist, their behavior is approximated using the describing functions. While this enables the loop-shaping design, the describing function approximation does not represent the system well in the presence of wide-band excitations and multiple resonance peaks in the plant. Chapter 7 explores how such conditions influence the reset elements and how to ensure that the use of reset is still beneficial.

Additionally, assessing the stability of a reset system solely based on controller dynamics and experimentally measured plant frequency response is an open problem. To address this, we extend the Negative Imaginary systems approach for stability analysis, originally developed for AVC of flexible systems with uncertain dynamics, to reset systems in Chapter 8.

The contributions of the thesis and the obtained insights are discussed in the concluding Chapter 9. The chapter also recommends new research directions, both as a direct continuation of this work or promising adjacent projects.

1

References

[1] C. G. Gordon, "Generic criteria for vibration-sensitive equipment," in *Vibration Control in Microelectronics, Optics, and Metrology*, vol. 1619, pp. 71–85, SPIE, 2 1992.

[2] M. Heertjes, K. de Graaff, and J. G. van der Toorn, "Active vibration isolation of metrology frames; A modal decoupled control design," *Journal of Vibration and Acoustics*, vol. 127, pp. 223–233, 6 2005.

[3] A. I. Oliva, M. Aguilar, and V. Sosa, "Low- and high-frequency vibration isolation for scanning probe microscopy," *Measurement Science and Technology*, vol. 9, pp. 383–390, 3 1998.

[4] C. Collette, S. Janssens, K. Artoos, and C. Hauviller, "Active vibration isolation of high precision machines," *Diamond Light Source Proceedings*, vol. 1, no. MEDSI-6, 2010.

[5] M. El Ajjaj, M. B. Kaczmarek, M. van den Hurk, and S. H. HosseinNia, "Vibration suppression of a state-of-the-art wafer gripper," in *EUSPEN SIG : PMSC*, 2022.

[6] R. M. Schmidt, G. Schitter, A. Rankers, and J. van Eijk, *The Design of High Performance Mechatronics*. Amsterdam: IOS Press, 2 ed., 2014.

[7] D. I. G. Jones, *Handbook of viscoelastic vibration damping*. Wiley, 2001.

[8] J. P. Den Hartog, *Mechanical Vibrations*. New York: McGraw-Hill Book Company, Inc., 1940.

[9] O. Nishihara and T. Asami, "Closed-form solutions to the exact optimizations of dynamic vibration absorbers (minimizations of the maximum amplitude magnification factors)," *Journal of Vibration and Acoustics, Transactions of the ASME*, vol. 124, no. 4, pp. 576–582, 2002.

[10] K. Verbaan, S. van der Meulen, and M. Steinbuch, "Broadband damping of high-precision motion stages," *Mechatronics*, vol. 41, pp. 1–16, 2 2017.

[11] A. Preumont, *Vibration Control of Active Structures*, vol. 246 of *Solid Mechanics and Its Applications*. Cham: Springer International Publishing, 4 ed., 2018.

[12] Z. R. Wani, M. Tantray, E. Noroozinejad Farsangi, N. Nikitas, M. Noori, B. Samali, and T. Y. Yang, "A Critical Review on Control Strategies for Structural Vibration Control," 1 2022.

[13] M. J. Balas, "Direct Velocity Feedback Control of Large Space Structures," *Journal of Guidance and Control*, vol. 2, pp. 252–253, 5 1979.

[14] M. A. Beijen, "Disturbance feedforward control for vibration isolation systems : analysis, design, and implementation," tech. rep., 2018.

[15] M. I. Hussein, M. J. Leamy, and M. Ruzzene, "Dynamics of phononic materials and structures: Historical origins, recent progress, and future outlook," *Applied Mechanics Reviews*, vol. 66, 7 2014.

[16] F. Zangeneh-Nejad and R. Fleury, "Active times for acoustic metamaterials," 11 2019.

[17] S. Dalela, P. S. Balaji, and D. P. Jena, "A review on application of mechanical metamaterials for vibration control," *Mechanics of Advanced Materials and Structures*, vol. 29, no. 22, pp. 3237–3262, 2022.

[18] J. U. Schmied, C. Sugino, A. Bergamini, P. Ermanni, M. Ruzzene, and A. Erturk, "Toward structurally integrated locally resonant metamaterials for vibration attenuation," in *Active and Passive Smart Structures and Integrated Systems 2017* (G. Park, ed.), vol. 10164, p. 1016413, SPIE, 4 2017.

[19] N. G. Rocha de Melo Filho, *Vibro-acoustic resonant metamaterials : from concept to engineering solution.* PhD thesis, 2020.

[20] Y. Zheng, Y. Chait, C. V. Hollot, M. Steinbuch, and M. Norg, "Experimental demonstration of reset control design," *Control Engineering Practice*, vol. 8, pp. 113–120, 2 2000.

[21] Q. Chen, Y. Chait, and C. V. Hollot, "Analysis of reset control systems consisting of a fore and second-order loop," *Journal of Dynamic Systems, Measurement and Control, Transactions of the ASME*, vol. 123, no. 2, pp. 279–283, 2001.

[22] O. Beker, C. V. Hollot, and Y. Chait, "Plant with integrator: An example of reset control overcoming limitations of linear feedback," *IEEE Transactions on Automatic Control*, vol. 46, pp. 1797–1799, 11 2001.

[23] D. Wu, G. Guo, and Y. Wang, "Reset integral-derivative control for HDD servo systems," *IEEE Transactions on Control Systems Technology*, vol. 15, pp. 161–167, 1 2007.

[24] G. Zhao, D. Nešić, Y. Tan, and C. Hua, "Overcoming overshoot performance limitations of linear systems with reset control," *Automatica*, vol. 101, pp. 27–35, 2019.

[25] N. Karbasizadeh, A. A. Dastjerdi, N. Saikumar, D. Valerio, and S. H. Hossein Nia, "Benefiting from linear behaviour of a nonlinear reset-based element at certain frequencies," in *2020 Australian and New Zealand Control Conference, ANZCC 2020*, pp. 226–231, Institute of Electrical and Electronics Engineers Inc., 11 2020.

[26] N. Karbasizadeh, N. Saikumar, and S. H. HosseinNia, "Fractional-order single state reset element," *Nonlinear Dynamics*, vol. 104, pp. 413–427, 3 2021.

[27] D. Caporale, L. F. van Eijk, N. Karbasizadeh, S. Beer, D. Kostic, and S. H. Hossein-Nia, "Practical Implementation of a Reset Controller to Improve Performance of an Industrial Motion Stage," *IEEE Transactions on Control Systems Technology*, vol. PP, pp. 1–12, 2024.

[28] R. T. Bupp, D. S. Bernstein, V. S. Chellaboina, and W. M. Haddad, "Resetting Virtual Absorbers for Vibration Control," *Journal of Vibration and Control*, vol. 6, pp. 61–83, 1 2000.

1

1

[29] M. A. Mohan, M. B. Kaczmarek, and S. H. Hosseinnia, "Resetting Velocity Feedback: Reset Control for Improved Transient Damping," in *2022 European Control Conference, ECC 2022*, pp. 1421–1428, Institute of Electrical and Electronics Engineers Inc., 2022.

[30] A. San-Millan, V. Feliu-Batle, and S. S. Aphale, "Application of a fractional order integral resonant control to increase the achievable bandwidth of a nanopositioner.," *IFAC-PapersOnLine*, vol. 50, no. 1, pp. 14539–14544, 2017.

[31] L. Marinangeli, F. Alijani, and S. H. Hosseinnia, "Fractional-order positive position feedback compensator for active vibration control of a smart composite plate," *Journal of Sound and Vibration*, vol. 412, pp. 1–16, 2018.

[32] W. Niu, B. Li, T. Xin, and W. Wang, "Vibration active control of structure with parameter perturbation using fractional order positive position feedback controller," *Journal of Sound and Vibration*, vol. 430, pp. 101–114, 9 2018.

[33] W. Niu, B. Li, Z. Gao, and W. Wang, "Fractional order control of vertical tail vibration based on first-order PPF," *Hangkong Xuebao/Acta Aeronautica et Astronautica Sinica*, vol. 39, 8 2018.

[34] D. Feliu-Talegon, A. San-Millan, and V. Feliu-Batlle, "Fractional-order integral resonant control of collocated smart structures," *Control Engineering Practice*, vol. 56, pp. 210–223, 11 2016.

[35] Y. Liu, D. Yu, H. Zhao, J. Wen, and X. Wen, "Theoretical study of two-dimensional phononic crystals with viscoelasticity based on fractional derivative models," *Journal of Physics D: Applied Physics*, vol. 41, p. 065503, 2 2008.

[36] M. Cajić, D. Karličić, S. Paunović, and S. Adhikari, "A fractional calculus approach to metadamping in phononic crystals and acoustic metamaterials," *Theoretical and Applied Mechanics*, vol. 47, no. 1, pp. 81–97, 2020.

[37] S. Sepehri, M. M. Mashhadi, and M. M. S. Fakhrabadi, "Wave propagation in fractionally damped nonlinear phononic crystals," *Nonlinear Dynamics*, vol. 110, pp. 1683–1708, 10 2022.

[38] W. Ding, J. P. Hollkamp, S. Patnaik, and F. Semperlotti, "On the fractional homogenization of one-dimensional elastic metamaterials with viscoelastic foundation," *Archive of Applied Mechanics*, vol. 93, pp. 261–286, 1 2023.

[39] S. H. Hosseinnia, I. Tejado, and B. M. Vinagre, "Basic properties and stability of fractional-order reset control systems," in *2013 European Control Conference, ECC 2013*, pp. 1687–1692, 2013.

[40] L. Chen, N. Saikumar, S. Baldi, and S. H. Hosseinnia, "Beyond the Waterbed Effect: Development of Fractional Order CRONE Control with Non-Linear Reset," in *Proceedings of the American Control Conference*, vol. 2018-June, pp. 545–552, Institute of Electrical and Electronics Engineers Inc., 8 2018.

1

[41] A. A. Dastjerdi, N. Saikumar, and S. H. HosseinNia, "Tuning guidelines for fractional order PID controllers: Rules of thumb," *Mechatronics*, vol. 56, pp. 26–36, 12 2018.

[42] A. A. Dastjerdi, B. M. Vinagre, Y. Q. Chen, and S. H. HosseinNia, "Linear fractional order controllers; A survey in the frequency domain," 1 2019.

[43] M. Steinbuch and M. L. Norg, "Advanced Motion Control: An Industrial Perspective," *European Journal of Control*, vol. 4, pp. 278–293, 1 1998.

[44] M. F. Heertjes, H. Butler, N. J. Dirkx, S. H. Van Der Meulen, R. Ahlawat, K. O'Brien, J. Simonelli, K. T. Teng, and Y. Zhao, "Control of Wafer Scanners: Methods and Developments," in *Proceedings of the American Control Conference*, vol. 2020-July, pp. 3686–3703, Institute of Electrical and Electronics Engineers Inc., 7 2020.

2

Loop-shaping for AVC

This chapter presents loop-shaping as a tool for designing active vibration control (AVC) systems, laying the foundations for the rest of this dissertation. Given that loop-shaping is extensively used in practical design for motion control, we start by linking the AVC to this field. We then analyze the closed-loop transfer functions of a general AVC system using a simple model. From these transfer functions, we derive the desired open-loop shape of the control system and show how the popular AVC methods relate to them. We demonstrate the application of the proposed loop-shaping approach through an experimental evaluation of an ultra-stiff vibration control system.

2.1 Motion and vibration control overview

To provide a foundation for further analysis, we revisit motion control, as presented in the context of wafer scanner systems in [1]. In motion control, but also in other control applications, two primary problems are identified. The first is the servo (or tracking) problem, where the output of the controlled system must closely follow a known reference trajectory. The second is the regulator (or disturbance rejection) problem, where the output of the controlled system, when subjected to unknown disturbances, should remain as close to zero as possible.

The two control problems are generally addressed by two different approaches, as illustrated in Figure 2.1. If the dynamics of the system are well known, the tracking problem can be solved by feedforward control [2], where the controller ideally matches the plant inverse $C_{FF} \rightarrow P^{-1}$. As the feedforward control is responsible for the majority of control forces in motion systems and associated performance [3], it remains an active field of research.

For disturbance rejection, it is crucial to minimize the sensitivity of the control system to noise or disturbance forces, particularly within the frequency range of interest. In the precision industry, this is typically achieved using PID feedback control. The role of the feedback controller is also to compensate for errors originating from the mismatch between the models used for the feedforward design and actual plant dynamics. Such feedback controllers are designed in the frequency domain to maximize the controller bandwidth, defined as the first unity crossing of the open-loop magnitude frequency response while adhering to constraints on closed-loop frequency responses. This method is embodied in manual loop-shaping [4, 5], which serves as an initial controller design tool, is widely understood within the motion control community, and offers insights into potential controller enhancements beyond the LTI control domain, possibly using nonlinear elements (we discuss this further in Chapters 7 and 8).

Vibration control systems address the disturbance rejection problem. To illustrate this, consider a mass-spring system on a shaking base, as shown in Figure 2.2a. In this system, x_m represents the position of the mass m, which should remain unaffected by base vi-
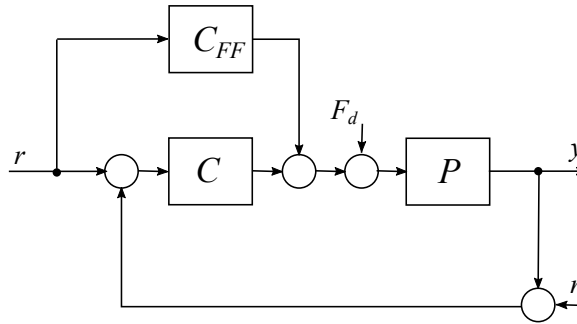
Figure 2.1: Block diagram of a motion system. P represents the plant to be controlled, C_{FF}, C correspond to the feedforward and feedback controllers. r is the reference to be followed by the output y, while the force disturbance F_d and measurement noise n act on the system.

(a) Mechanical model   **(b)** Block diagram
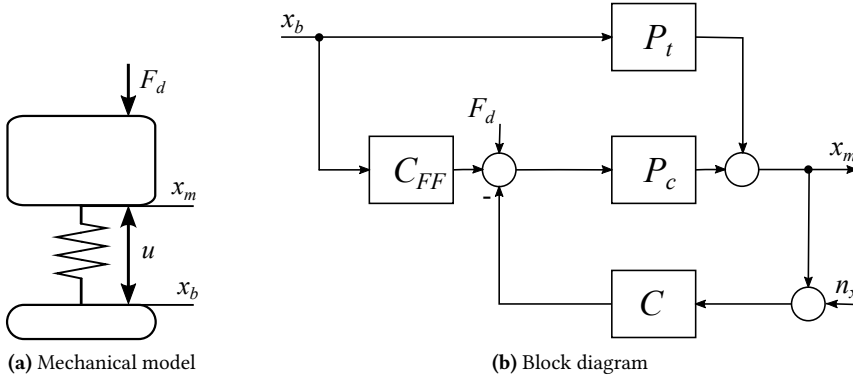
Figure 2.2: Mechanical model (a) and block diagram (b) of an AVC system. P_t and P_c correspond to the transmissibility and compliance of the plant. The position of the isolated mass x_m should remain steady in presence of the base motion x_b and direct forces F_d. u represents the control forces generated by the controllers. For absolute measurements, $n_x = n$, and for relative measurements, $n_x = n - x_b$ indicates the relationship of the measured signal to the base displacement.

brations x_b and direct disturbances F_d. To achieve this, the control system generates an actuator force u based on available measurements. This simple model is useful for presenting control concepts. However, in practical control system design, actual system dynamics and the presence of sensors and actuators must be considered, especially to guarantee the stability of the system.

The available measurements often distinguish motion control systems from vibration control systems. Generally, metrology systems for motion control are designed to measure the position of the controlled object relative to a reference relevant to the specific application. For instance, in a wafer scanner, the position of the wafer stage is measured relative to a metrology frame that supports the projection optics. In the remainder of this chapter, we will use the term *absolute* to refer to such measurements, as illustrated in Figure 2.2a by x_m. In AVC, however, a broader variety of quantities are measured, such as displacements, velocities, accelerations, or forces. These measurements are often not taken with respect to the relevant reference frame but rather *relative* to the system's base, which can also be a significant source of disturbances. In Figure 2.2a, such a measurement corresponds to the displacement $x_m - x_b$.

For the remainder of this chapter, we will simplify the comparison of approaches with different sensors by relating all signals to position measurements x_m and x_b. Necessary elements for converting between different quantities are included within the controller dynamics. For example, a controller in a system where the acceleration signal is integrated will be considered equivalent to one in a system where the position measurement is differentiated. The differences between these systems can be represented by the parasitic dynamics and characteristics of disturbance and noise sources.

The difference between motion control and AVC can also be explained using the High Authority Control (HAC) and Low Authority Control (LAC) concepts [6]. In motion control, the feedback controller usually significantly changes the system's dynamics. It can be

said that it strongly influences the structure and belongs to the HAC approach. In contrast, the objective of AVC systems is often only active damping, which aims to shift the poles of the system slightly. Such a system is an example of LAC. However, the division of the strategies used in the two applications is not sharp. LAC also finds application in motion control, for example, as active damping of resonance peaks in piezoelectric nanopositioning stages [7, 8], and HAC strategies may be efficient for disturbance rejection, which makes them a possible choice for AVC applications.

2.2 Closed-loop description of an AVC system

The equation of motion for the system in the Figure 2.2a is

$$m\ddot{x}_m(t) + c(\dot{x}_m(t) - \dot{x}_b(t)) + k(x_m(t) - x_b(t)) = F_d(t) - u(t). \tag{2.1}$$

After the Laplace transformation of the equation and rearranging it, the position x_m can be shown

$$x_m(s) = P_c(s)(F_d(s) - u(s)) + P_t(s)x_b(s), \tag{2.2}$$

$$P_c(s) = \frac{x_m(s)}{F_d(s)} = \frac{1}{ms^2 + cs + k}, \tag{2.3}$$

$$P_t(s) = \frac{x_m(s)}{x_b(s)} = \frac{cs + k}{ms^2 + cs + k}. \tag{2.4}$$

The two transfer functions characterise the system in the absence of control and indicate two problems AVC should tackle. The compliance $P_c(s)$ describes the influence of the external forces on the system and is the function seen by the controller. The transmissibility $P_t(s)$ describes the influence of the base displacement. The two transfer functions also illustrate the well-known trade-off for passive vibration isolation, as increasing the stiffness k leads to smaller compliance and increased transmissibility at higher frequencies.

As in motion control, the two problems related to transmissibility and compliance can be tackled separately, in the architecture presented in Fig. 2.2b. If the base displacement is known, it is possible to minimise its influence on the system using feedforward control $C_{FF}(s)$. The feedforward approach is beneficial irrespective of whether absolute or relative measurements are used for feedback and is well explored in the literature. The use of feedforward also does not influence the behaviour of the system's compliance. While feedforward is an essential tool for high-performance vibration isolation, it is not the focus of this work.

Feedback control can improve the system's response to unknown disturbances. As the closed-loop behaviour of the system with feedback will differ if absolute or relative measurements are used, we consider the two cases separately. The difference between the cases can be easily illustrated by considering a mechanical analogue of the control system. The controllers using absolute measurements can be represented by mechanical components attached between the body with position x_m and the "sky", with the "sky-hook" damping as a well-known example. With relative measurements, the control system is represented by components between the mass with x_m and the base. Using such mechanical analogues can provide an intuitive understanding of the behaviour of the system.

2.2.1 Absolute measurements

Consider the AVC system in Fig. 2.2b with feedback based on absolute measurements only ($C_{FF}(s) = 0$). The control signal in this case is $u(s) = C(s)(x_m(s) + n(s))$. Substituting into (2.1) we have

$$x_m(s) = -P_c(s)C(s)x_m(s) - P_c(s)C(s)n(s) + P_c(s)F_d(s) + P_t(s)x_b(s), \tag{2.5}$$

$$\frac{x_m(s)}{x_b(s)} = \frac{P_t(s)}{1 + P_c(s)C(s)} = P_t(s)S(s), \tag{2.6}$$

$$\frac{x_m(s)}{F_d(s)} = \frac{P_c(s)}{1 + P_c(s)C(s)} = P_c(s)S(s), \tag{2.7}$$

$$\frac{x_m(s)}{n(s)} = \frac{-P_c(s)C(s)}{1 + P_c(s)C(s)} = S(s) - 1. \tag{2.8}$$

The closed-loop transmissibility and compliance are determined by the open-loop transfer functions and the sensitivity $S(s)$. For this reason, the sensitivity is referred to as the "vibration reduction ratio" in a part of vibration control literature [9–11].

First, let's consider a HAC approach for AVC, explored already in [12]. Since the compliance and the transmissibility have low-pass characteristics and the sensitivity of the system has high-pass characteristics with the corner frequency determined by the bandwidth, HAC system can provide large rejection of x_b and F_d. For best transmissibility reduction, the resonance frequency of the plant $\omega_p = \sqrt{k/m}$ should be as small as possible. For improved compliance, increasing the stiffness of the plant is beneficial. Increasing the bandwidth of the control system is beneficial for the rejection of both the direct F_d and indirect x_b disturbances. The HAC approach, however, is not always applicable, even if absolute measurements are available. Constructing a HAC controller based on measurements related to velocities or accelerations is an open challenge. Moreover, low-frequency noise or drift n influence the x_m directly, as (2.8) shows.

An LAC controller can be designed to lower the transfer functions locally, for example, to attenuate a selected resonance peak only. To achieve this, as can be seen in (2.6) and (2.7), sensitivity $S(s)$ should have a shape of a notch filter, with a magnitude equal to 1, except for a targeted range of frequencies, where it should be small to reduce the magnitude of the responses. This target frequency will often be the resonance frequency of the structure or a frequency where disturbances are especially problematic. Obtaining such a shape of S would also limit the problems caused by noise n, as shown in (2.8). The design of a controller to obtain such sensitivity will be discussed later in this chapter.

2

2.2.2 Relative measurements

An AVC system with relative measurements is represented by the same block diagram in Fig. 2.2b, with a difference that the x_b is subtracted from the input signal of the controller, leading to $u(s) = C(s)(x_m(s) - x_b(s) + n(s))$ and

$$x_m(s) = -P_c(s)C(s)x_m(s) + P_c(s)C(s)x_b(s) + P_c(s)F_d(s) + P_t(s)x_b(s), \qquad (2.9)$$

$$\frac{x_m(s)}{x_b(s)} = \frac{P_t(s) + P_c(s)C(s)}{1 + P_c(s)C(s)} = P_t(s)S(s) + P_c(s)C(s)S(s), \qquad (2.10)$$

$$\frac{x_m(s)}{F_d(s)} = \frac{P_c(s)}{1 + P_c(s)C(s)} = P_c(s)S(s), \qquad (2.11)$$

$$\frac{x_m(s)}{n(s)} = \frac{-P_c(s)C(s)}{1 + P_c(s)C(s)} = S(s) - 1. \qquad (2.12)$$

The influence of the feedback on compliance is the same as that of the system with absolute measurements. The use of a high bandwidth HAC controller would lead to improved rejection of disturbance force F_d but could lead to the direct transmission of low-frequency noise and drift to the relevant position x_m.

In the case of transmissibility, however, using a HAC controller leads to tracking of the base displacement x_b by x_m, which is evident from the complementary sensitivity $P_c(s)C(s)S(s)$ appearing in the closed-loop relationship. To simplify the analysis, we relate the gain of the controller to the low-frequency gain of compliance $C(s) = kC^*(s)$ and ignore the damping of the plant, taking $c = 0$. We have then

$$\frac{x_m(s)}{x_b(s)} = \frac{P_t(s)(1 + C^*(s))}{1 + P_t(s)C^*(s)} = P_t(s)(1 + C^*(s))S(s), \qquad (2.13)$$

since $P_t(s) = kP_c(s)$ in the absence of damping. The transfer function $(1 + C^*(s))S(s)$ is characteristic of systems with relative measurements.

Similarly to the AVC with absolute measurements, the aforementioned problems with the direct influence of noise n and base displacement x_b on x_m are reduced when a LAC strategy leading to notch-shaped sensitivity $S(s)$ is used. We discuss the design of such a controller in the next section.

2.3 Loop-shaping for AVC - triangular loop shape

In both cases considered in the previous section, the sensitivity $S(s)$ has a role of vibration reduction ratio. This allows us to define the loop-shaping requirements for the AVC systems, illustrated in Fig. 2.3, where the close-loop compliance $T_c(s) = x_m(s)/F_d(s)$ is considered for simplicity. To reduce the response amplitude at a selected frequency range, we require $|S(s)| \ll 1$. At the same time, to avoid excitation of the structure by noise, the $|S| \approx 1$ is required at all other frequencies. This means that the desired sensitivity for LAC should have the shape of a notch filter.
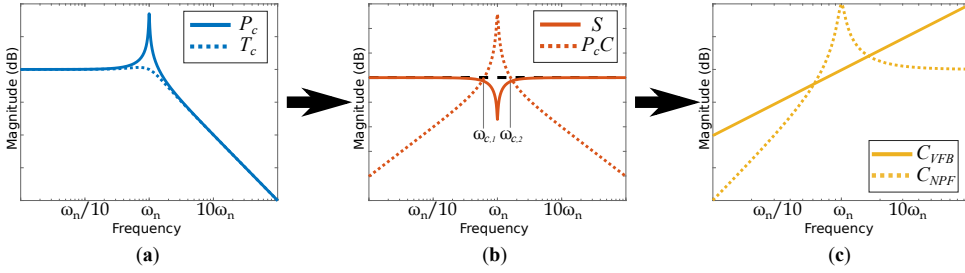
Figure 2.3: Illustration of the concept of loop-shaping. Based on the knowledge of the plant dynamics P_c and the desired response T_c (a), we can deduce the necessary shape of the sensitivity S (b). The needed shape of the loop gain $P_c C$ follows from the definition of S. Knowing the overall requirements, the designer has the freedom to choose the controller shape (c), as long as the gain $|P_c C|$ at the target frequency is high and sufficient phase margins at the crossover frequencies $\omega_{c,1}, \omega_{c,2}$ are assured. The choice of controller dynamics is discussed further in Section 2.4.

Based on the definition

$$S(s) = \frac{1}{1 + P_c(s)C(s)},$$

we can deduce that the loop-gain $P_c(s)C(s)$ to should have a triangular shape, with a positive slope below the targeted frequency and a negative above. The triangular loop shape leads to two cross-over frequencies $\omega_{c,1}, \omega_{c,2}$ that require designers' attention to ensure that the system is stable. To assure the stability, the phase at the cross-over frequencies should remain between $\pm 180°$. If the phase at any of the crossover frequencies approaches the stability limits, a new resonance peak is created in the closed loop, with the damping related to the phase margin. The desired loop-gain $P_c(s)C(s)$, together with the knowledge of plant compliance $P_c(s)$, allows us to define the requirements for the controller. Commonly used controllers fitting in these requirements are discussed in the next section.

In practice, plants in AVC have a large number of high-frequency resonance modes. Moreover, they are often characterised by parameter uncertainty or variations and may have unmodelled dynamics. The characteristics of sensors and actuators used bring additional complexity. Therefore, the stability analysis should be robust in the presence of such effects. While this problem is simplified to some extent by using collocated sensors and actuators [6], caution is required and the designer should always know how the actual system fits the idealized approximations used in stability proofs. The robustness properties of AVC systems for flexible structures can be captured by negative-imaginary (NI) systems theory. This theory is closely related to positive-real systems and passivity, can be used to analyse MIMO systems and has been extended to encompass some classes of nonlinear systems. The NI approach is presented in detail more in Chapter 8; we also refer interested readers to [13, 14].

2.4 Overview of common AVC controllers

In this section, we present an overview of commonly used AVC approaches. As mentioned before, we simplify the comparison of controllers with different sensors by relating all sig-

nals to position measurements. For each control approach, while the loop shapes obtained with different measurements used are the same, the controller dynamics that have to be implemented differ. We focus only on controllers for which the negative imaginary systems theory can be used for assessing the stability (that is, the phase of the loop-shape with the plant (2.1) does not extend beyond ±180) and we limit the considerations to single-input and single-output (SISO) control strategies.

Traditionally, combinations of different measured signals and controllers leading to the same loop gain dynamics are presented in the literature as different control strategies. Moreover, a common, well-established naming convention for AVC controllers does not exist. Therefore, we do our best to refer to possible alternative names for each of the presented cases. Figure 2.4 compares the behaviour of the considered AVC controllers on plant (2.1) with absolute and relative measurements. The characteristics of each of the considered controllers are discussed in the following sections.

Several modified versions of each presented controller can be found in the literature. Some modifications are limited to placing the basic controllers presented here in parallel [15, 16]. In other, nonlinear terms are added to the controllers to deal with plant non-linearity [17–20] or to increase the efficiency of damping for LTI plants [21, 22]. In this thesis, we discuss the fractional-order alternatives for vibration controllers in Chapter 5 and augmenting AVC systems with reset elements in Chapter 7.

In the literature, a large effort is taken to derive optimal tuning conditions for specific controllers with simplified systems. However, such tuning parameters are only an indication for an initial design, as they are not optimal in the presence of parasitic dynamics, time delays or significant levels of damping in the plant. For this reason, we do not focus on such derivations.

2.4.1 Velocity Feedback

Velocity feedback (VFB) [23] is the simplest active vibration control strategy and aims to emulate the viscous damping in the systems. The controller, in this case, is

$$C_{VFB}(s) = k_{VFB}s, \tag{2.14}$$

with k_{VFB} denoting the gain of the controller. The loop-gain $C_{VFB}(s)P_c(s)$ has a +1 slope at frequencies $\omega < \omega_p$ and −1 slope at $\omega > \omega_p$, which leads to perfect notch-shaped sensitivity. When relative measurements are used, the system's high frequency transmissibility increases, which is evident from (2.12). This does not happen for compliance or when absolute measurements are used ("sky-hook damping").

The velocity feedback is often combined with band pass filters (VBP)

$$C_{VBP}(s) = k_{VBP}s \frac{s}{s + \omega_H} \frac{1}{s/\omega_L + 1} \tag{2.15}$$

which increases the slope of the loop-gain to +2 at $\omega < \omega_H$ and −2 at $\omega > \omega_L$. This reduces the phase margins at the cross-over frequencies, depending on the relation of ω_H and ω_L to the crossover frequencies, may lead to the increase of sensitivity magnitude above 1 and the creation of parasitic resonance peaks, as can be seen in Fig. 2.4c. Using the low-pass filter also allows for limiting the increase of the transmissibility at high frequencies when relative measurements are used, as in Fig. 2.4f.

The velocity feedback is often implemented by integrating acceleration signals, measuring velocities directly with geophones or by differentiating position measurements. Similar characteristics can be obtained with force measurements (related to the relative acceleration between the base and the mass) when integral force feedback (IFF) [6] is implemented.

2.4.2 Negative Position Feedback

To increase the magnitude of the loop gain at a narrow range of frequencies, a lightly damped resonance peak is introduced to the controller in the Negative position feedback (NPF) [11, 24] strategy. The advantage of such a design is clearly visible by comparing the loop gains in Fig. 2.4a. At the target frequency, both the VF and NPF lead to the same magnitude, while the curve for the NPF controller has significantly lower magnitudes at lower and higher-frequency regions. To achieve this, the controller has the form

$$C_{NPF}(s) = \frac{k_{NPF}s^2}{s^2 + 2\zeta_{NPF}\omega_{NPF}s + \omega_{NPF}^2},\tag{2.16}$$

where $k_{NPF}, \omega_{NPF}, \zeta_{NPF}$ denote the controller gain, resonance frequency and damping coefficient, respectively. The dynamics of the controller are closely related to the dynamics of a tuned mass damper (TMD) [25]. The same dynamics characterize systems damped with the Negative derivative feedback (NDF) [26, 27] controllers, where velocities of the structure are filtered by a band-pass filter with a resonance peak.

The controllers are tuned such that $\omega_{NPF} \approx \omega_p$, with the optimal shift between the corner frequencies dependent on the selected gain of the controller. The controllers' gain k_{NPF} can be seen as equivalent to the mass ratio μ in the TMD [28]. Let's assume $\omega_{NPF} = \omega_p$ for simplicity. The loop-gain $C_{NPF}(s)P_c(s)$ has a +2 slope at frequencies $\omega < \omega_{NPF}$ and −2 slope at $\omega > \omega_{NPF}$. For small ζ_{NPF}, the phase margins at the crossover frequencies are small, leading to the creation of large resonance peaks in a closed loop and "peak splitting", typical also for lightly damped TMDs and visible in Fig. 2.4c-f. Increasing the damping coefficient ζ_{NPF} leads to increased phase margins and reduction of the resonance peaks, with the price of lesser attenuation at the target frequency.

2.4.3 Positive position feedback

The VF and NPF controllers implemented in systems with position measurements are characterised by large gains at high frequencies and do not "roll off" as frequencies increase. Consequently, they are often not robust and lead to low performance in systems with multiple resonance peaks. To address these problems, a positive position feedback (PPF) controller was introduced [29]. The controller has the transfer function

$$C_{PPF} = \frac{-k_{PPF}\omega_{PPF}^2}{s^2 + 2\zeta_{PPF}\omega_{PPF}s + \omega_{PPF}^2}\tag{2.17}$$

where $k_{PPF}, \omega_{PPF}, \zeta_{PPF}$ denote the controllers gain, corner resonance frequency and damping coefficient, respectively. Note that the negative sign placed before the controller's gain is introduced to represent the positive feedback in the standard control loop. While the

controller is characterized by low-pass dynamics, the negative sign "shifts the phase" by 180°, as can be seen in Fig. 2.4a, making it similar to that of NPF.

The loop gain obtained with the PPF controller is not triangular, as it has a low-pass shape with steep roll-off at high frequency (Fig. 2.4b). While this helps to make the controller more robust to high-frequency dynamics, the high gain of the controller at low frequencies negatively influences system performance. In terms of mechanical analogues, the low-frequency gain acts as "negative stiffness", softening the structure. This leads to the amplification of low-frequency transmissibility above 1 when absolute measurements are used (Fig. 2.4e and an increase in compliance with both the absolute and relative measurements (Fig. 2.4d).

Similar to the NPF and mechanical TMD, the best results are achieved with the corner frequency ω_{PPF} shifted with respect to the resonance of the structure [30]. The damping ratio ζ_{PPF} influences the phase margins at the crossover frequencies, and the low values lead to "peak splitting". For the stability of the system, the low-frequency magnitude of the loop gain should be smaller than one $|C_{PPF}(0)P_c(0)| < 1$. The stability condition is clear once one considers the Nyquist plot of the system. The condition can also be supported by mechanical analogy. The system becomes unstable when the stiffness of the plant is cancelled by the "negative stiffness" of the controller. Note, that this stability condition is only valid for ideal plants. In practice, the stability can be checked more reliably by using the Nyquist plot.

2.4.4 Integral resonance control

As an alternative to PPF, a first-order low-pass filter can be used for active damping. In a SISO case, such a strategy is equivalent to the integral resonant control (IRC). In the literature [31, 32], the IRC has been introduced in a more complex architecture involving feedthrough terms and possibly more complex dynamics, which is especially relevant for MIMO systems. However, in the simplest case, the dynamics are reduced to

$$C_{IRC} = \frac{-k_{IRC}}{s/\omega_{IRC} + 1} \tag{2.18}$$

with the k_{IRC}, ω_{IRC} denoting the controllers gain and corner frequency.

Like the PPF, the IRC can provide robust performance for systems with position measurements and multiple resonance peaks. The use of IRC also leads to the "softening" of the system and an increase in low-frequency compliance due to the "negative stiffness" (Fig. 2.4d). Consequently, a condition on the low-frequency magnitude of the loopgain $|C_{IRC}(0)P_c(0)| < 1$ should be obeyed for systems stability. The low-frequency amplification can also be seen in the transmissibility when absolute measurements are used (Fig. 2.4e). While the controller's gain can not be increased with a resonance peak, one may attempt to dampen multiple resonances of the plant with a single controller, as the phase of the controller is equal to 90° at a wide range of frequencies, which can be seen in Fig. 2.4a.
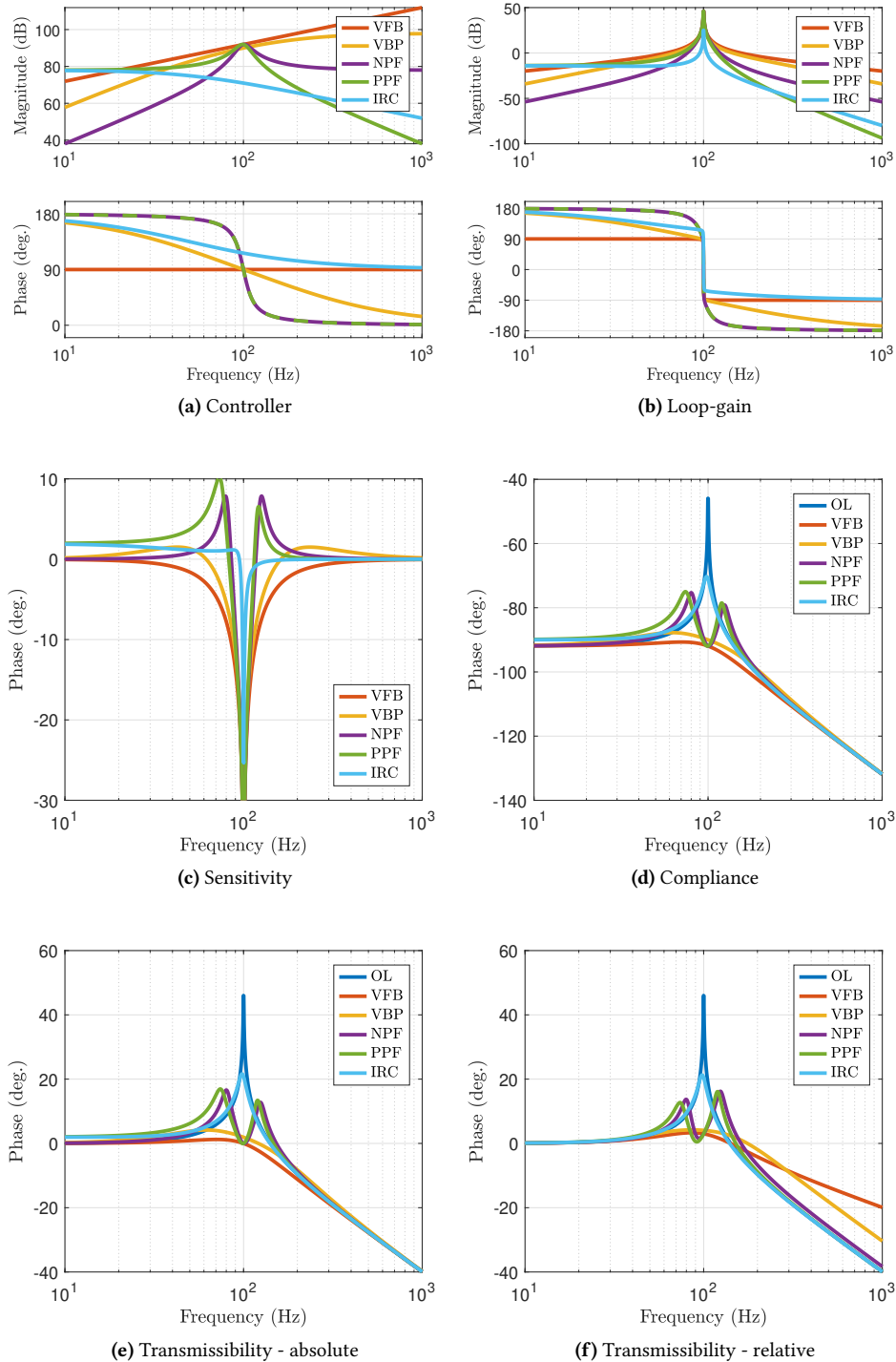
(a) Controller

(b) Loop-gain

(c) Sensitivity

(d) Compliance

(e) Transmissibility - absolute

(f) Transmissibility - relative

Figure 2.4: Overview of the controllers and resulting closed-loop characteristics

2.5 Application in the evaluation of ultra-hard vibration isolation mount

In this section, to show the loop-shaping approach in AVC, we evaluate a hard mount system's performance with different control strategies. The role of the mount in precision equipment is not only supporting and levelling a machine but also coping with disturbances. When the floor vibrations are the primary concern, the mount can be designed as a soft vibration isolation system [33]. The low stiffness and the corresponding low resonance frequency of the system (typically below 5Hz) are advantageous in this context, as above the resonance, the transmissibility of vibration is attenuated. This, however, comes at the cost of problems with levelling, sagging and increased force disturbance sensitivity [34]. Hard mounts have been proposed to address these issues [35]. Using a higher stiffness mount leads to much-decreased sensitivity to direct disturbances [12] and a higher resonance frequency of the system, reaching 35 Hz [34]. In consequence, the system is more susceptible to indirect vibrations.

Here, we focus on applications where the direct disturbances acting on the system are large and position stability is especially important. To assure it, an *ultra hard* mount based on piezoelectric stack actuators is proposed. The high stiffness of the piezoelectric stack prevents the excitation of the structure by direct disturbances. Thanks to the capability of exerting high forces, an active solution can be created to deal with both direct and indirect disturbances effectively. Additionally, piezoelectric stacks are proven technology in the high-tech industry, have low energy consumption in static operation, and produce no magnetic fields that can interfere with sensitive equipment [36].

We evaluate the achievable performance with AVC strategies based on three sensors: accelerometers, capacitive position probes, strain gauges and different controller dynamics. Because of the high resonance frequency, the system's passive structure is ineffective in isolating the floor vibrations. To address this, we investigate using a rudimentary feedforward based on stiffness compensation. While more advanced strategies are available in the literature (see [34, 37–39]), we want to find out how big performance improvement is possible with simple means.

2.5.1 System description

A single-axis experimental setup, presented in Fig.2.5, is used to represent the ultra hard mount system. A platform with adjustable mass represents the payload to be supported. The main stack actuator (model *P-843.20*) has a stiffness of 27×10^6 N/m, and constitutes the ultra hard mount and connects the payload to the shaking base. This shaking base is actuated by another stack actuator (model *P-235.1S*), with a higher stiffness of 860×10^6 N/m. Motion of all elements of the setup is constrained to a single degree of freedom using flexures. The abstraction of the setup is also presented in Fig. 2.5. Accelerations $\ddot{x}_1, \ddot{x}_2$ are measured using *PCB Synotech 393B05* accelerometers. Absolute displacement of m_1 is measured with a *PIseca D-510.021* and the the absolute displacement of m_2 with a *D-050* capacitive sensor. Finally, relative measurements are taken with the integrated strain gauge sensors of the stack actuators. In the configuration used in this paper, the resonance frequency of the system is ω_p = 103 Hz. This can be adjusted to a higher or lower frequency by adjusting the mass m_2.
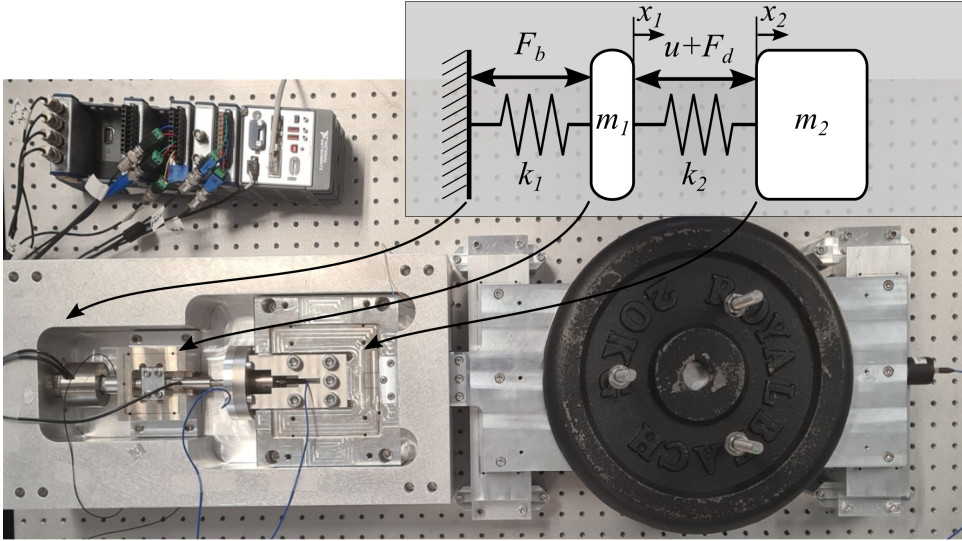
Figure 2.5: Overview of the experimental setup and an approximate mass-spring-damper model of the system.

To study the response of a system to floor vibrations, a vibration profile based on the VC-C curve from [40] is applied to the shaking base. Direct disturbances are applied to the main stack actuator, also used for active vibration control, with the force profile starting at 10 N at low frequencies and descending with −1 slope from 5 Hz onwards.

The goal of vibration control is to minimize the motion of the mass $\ddot{x}_2$. To calculate the total error, the Power Spectrum Density (PSD) of the signals is integrated to obtain the Cumulative Power Spectrum (CPS):

$$\text{CPS}(f) = \int_0^f \text{PSD}(v)\, \mathrm{d}v \tag{2.19}$$

The CPS visualizes the contribution to the total error at each frequency. The final value of the CPS is equal to the square of the root-mean-square (RMS) of the signal [41].

2.5.2 Controller tuning

The controllers were tuned based on rules from literature and experimental observations. Because acceleration $\ddot{x}_2$ was used as an input signal, the velocity feedback controller (VFB) was implemented as an imperfect integrator, which corresponds to (2.15) with the corner frequency of the high-pass filter $\omega_H = 10$ rad/s and without the low-pass term ($\omega_L \rightarrow \infty$). In the case of velocity band-pass controller (VBP), the corner frequencies were set at $\omega_H = \omega_p/2$ and $\omega_L = 3\omega_p$ as it was found this gave a good trade-off between damping and low noise amplification. The tuning of the negative acceleration controller (NAF) as in (2.16) was based on [42]. Tuning of both positive position feedback (PPF) controllers (2.17) was based on the tuning in [20]. The damping coefficient for relative position feedback was

2
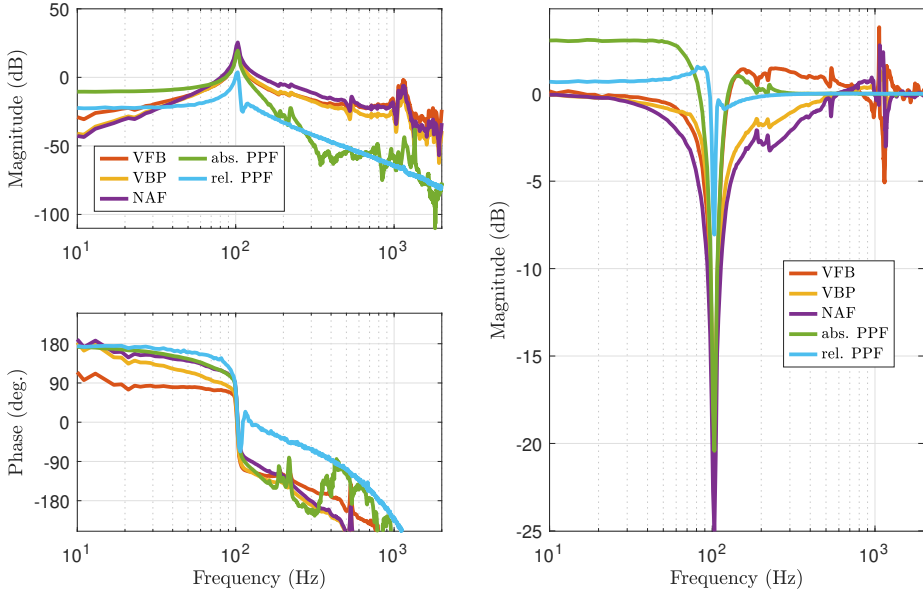
(a) Open-loop gain of the different AVC strategies.   (b) Sensitivities obtained with different AVC strategies.

Figure 2.6: The open-loop gain and transmissibility plots of the different implemented strategies.

halved as experiments showed this improved performance. For each controller, the gain was found by performing a sweep on the experimental setup, and the value leading to minimal RMS amplitude of vibrations was selected.

The open-loop gains obtained with the different controllers and sensors are presented in 2.6a. Due to the parameter sweep procedure used for the selection of the controllers' gains, the magnitudes of loop gains show significant differences. Especially, the low gain leading to optimal results for the PPF based on relative measurements obtained with a strain gauge indicates significant noise introduced by the sensor to the system, when compared with other control architectures. The low loop gain, corresponds to a narrow "notch" in the sensitivity, as demonstrated in Fig. 2.6b. At lower frequencies, the sensitivities obtained with the PPF controllers have magnitudes greater than 1, indicating the "softening" of the plant.

The feedforward controller is used to decrease the transmissibility of vibrations from the base of the mount. By calculating the system's reaction to the measured indirect disturbance, their effect can be diminished with an opposing control force. The most basic approach is stiffness compensation feedforward. With this method only the stiffness is accounted for and combined with a low-pass filter to avoid feeding noise into the system:

$$K_{ff} = -k \frac{\omega_{lp}}{s + \omega_{lp}}. \tag{2.20}$$
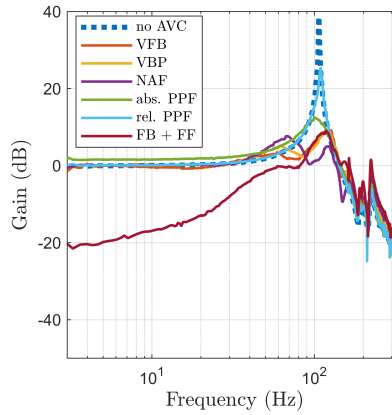
Figure 2.7: Transmissibility from x_1 to x_2 of the system with no AVC and with different strategies implemented, showing the damping performance of the different methods.

Note that the position of the base (x_1) is used for feedforward signal generation. For best results, feedback for active damping and feedforward are used simultaneously.

2.5.3 Closed-loop results

The closed-loop transmissibility with each strategy was measured by exciting the system and measuring the response from x_1 to x_2, with results plotted in Fig. 2.7. The response in the absence of control is characterized by a sharp resonance peak at 103 Hz. All the tested strategies achieve a significant reduction of the resonance peak, with the best results achieved using the acceleration-based methods (VFB, VBF, NAF). When PPF with absolute position measurement is used, base vibration transmission at low frequencies is amplified. A significant transmissibility reduction is obtained with the feedforward strategy. Due to the simplistic nature of the method used, it is mainly effective in a narrow range of frequencies. This, however, is sufficient to improve the performance of the system significantly, as will be demonstrated.

Fig. 2.8a shows the CPS of the response of the system to combined direct and indirect disturbances. Without control, large contributions are caused by the resonance peak at 103 Hz and high-frequency modes of the system around 1100 Hz. With active damping, the contribution of the resonance is significantly decreased. However, visible from the increase before the resonance frequency compared to the open-loop, the influence of the noise on the system is amplified. Furthermore, the high-frequency parasitic modes at around 1100 Hz are excited by the controllers, leading to a slight increase in vibrations. This shows the trade-off existing with these controllers: an increase in gain leads to both increased damping, amplified influence of noise and excitation of high-frequency modes. This behaviour limits the achievable reduction of vibrations.

The performance of the PPF using absolute position measurements approaches the performance of velocity feedback. This is achieved despite the amplification of the base-vibration transmissibility and smaller resonance peak reduction, thanks to smaller excita-

2
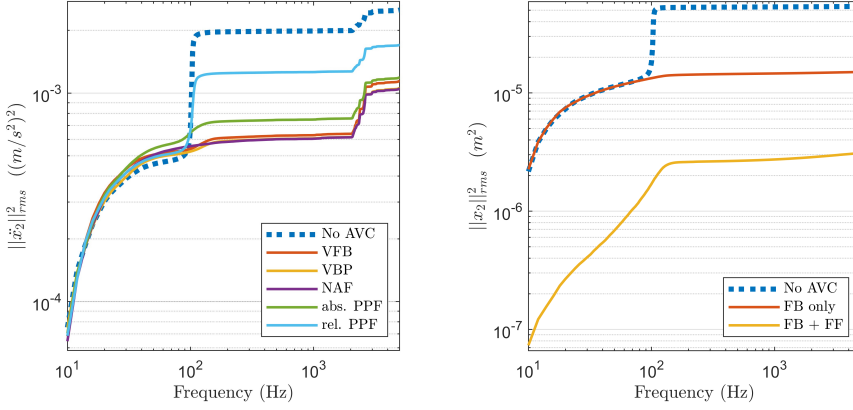
(a) CPS of $\ddot{x}_2$ showing the system response to direct and indirect disturbance excitation without AVC and with different feedback strategies implemented.

(b) CPS of x_2 showing the system response to indirect disturbance excitation without AVC, with only feedback, and feedback combined with stiffness compensation feedforward.

Figure 2.8: Cumulative Power Spectra obtained from the experimental results.

tion of the high-frequency dynamics. The PPF with relative position measurements is not able to achieve similar performance, probably due to the higher noise levels introduced by the strain sensor used, which requires further investigation. It can be seen that relative PPF has high open-loop gain at low frequencies without a significant peak at the resonance frequency. As a result, it is not possible to dampen the resonance without also strongly amplifying low-frequency disturbances. The results are summarized in Table 2.1, which shows the results numerically in terms of the RMS of $\ddot{x}_2$.

The position of the isolated mass x_2 is used as a performance indicator when evaluating feedforward since position feedforward was implemented. To show the influence of feedforward on the reduction of indirect disturbances, only these were used to excite the

Table 2.1: Numerical results of experimental evaluation of different AVC feedback strategies showing the RMS of the acceleration of the isolated mass $\ddot{x}_2$ of each strategy and the percentage with respect to no AVC.

Method	RMS of $\ddot{x}_2$ (m/s^2)	% of No AVC
No AVC	2.5007e-03	100%
VFB	1.1426e-03	45.69%
VBP	1.0572e-03	42.27%
NAF	1.0489e-03	41.94%
abs. PPF	1.1877e-03	47.49%
rel. PPF	1.7018e-03	68.05%

Table 2.2: Numerical results of experimental evaluation of indirect disturbance rejection with feedback and feedforward showing the RMS of the position of the isolated mass x_2 and the percentage with respect to no AVC.

Method	RMS of x_2 (m)	% of No AVC
No AVC	5.3778e-05	100%
FB only	1.5021e-05	27.93%
FB + FF	3.0984e-06	5.76%

2

system. In Fig. 2.8b the obtained CPS are plotted. While the feedback control, to a large extent, removes the amplification of vibration due to the resonance, it does not influence the low-frequency vibration transmission. When feedforward is used, the low-frequency contributions are reduced, which results in an almost 95% decrease in the final vibration magnitude. This shows that even straightforward stiffness compensation feedforward can greatly improve system performance. These results can be found numerically in Table 2.2.

2.6 Conclusion

This chapter presented loop shaping as a tool for designing AVC systems. The problems in AVC were first related to the ones in a more established field of motion control and studied in two cases: with absolute and relative measurements. Based on the closed-loop transfer functions and the knowledge of plant dynamics, we deduced the desired shapes of controllers. Subsequently, the commonly used AVC strategies from the literature were presented in the loop shaping framework. Finally, the use of the approach was presented in an experimental evaluation of an ultra-hard mount system. The concepts presented in this chapter will be used in the remainder of this thesis, demonstrating that loop shaping is an effective strategy for the analysis and design of practical AVC controllers.

References

[1] M. F. Heertjes, H. Butler, N. J. Dirkx, S. H. Van Der Meulen, R. Ahlawat, K. O'Brien, J. Simonelli, K. T. Teng, and Y. Zhao, "Control of Wafer Scanners: Methods and Developments," in *Proceedings of the American Control Conference*, vol. 2020-July, pp. 3686–3703, Institute of Electrical and Electronics Engineers Inc., 7 2020.

[2] G. M. Clayton, S. Tien, K. K. Leang, Q. Zou, and S. Devasia, "A review of feedforward control approaches in nanopositioning for high-speed spm," 2009.

[3] M. Heertjes, D. Hennekens, and M. Steinbuch, "MIMO feed-forward design in wafer scanners using a gradient approximation-based algorithm," *Control Engineering Practice*, vol. 18, pp. 495–506, 5 2010.

[4] M. Steinbuch and M. L. Norg, "Advanced Motion Control: An Industrial Perspective," *European Journal of Control*, vol. 4, pp. 278–293, 1 1998.

[5] R. M. Schmidt, G. Schitter, A. Rankers, and J. van Eijk, *The Design of High Performance Mechatronics*. Amsterdam: IOS Press, 2 ed., 2014.

[6] A. Preumont, *Vibration Control of Active Structures*, vol. 246 of *Solid Mechanics and Its Applications*. Cham: Springer International Publishing, 4 ed., 2018.

[7] C. Ru, X. Liu, and Y. Sun, *Nanopositioning technologies: Fundamentals and applications*. 2015.

[8] Z. Chen, X. Zhong, J. Shi, and X. Zhang, "Damping-enabling technologies for broadband control of piezo-stages: A survey," 1 2021.

[9] V. Sethi, M. A. Franchek, and G. Song, "Multimodal active vibration suppression of a flexible structure by loop shaping," in *Smart Structures and Materials 2005: Smart Structures and Integrated Systems*, vol. 5764, p. 348, SPIE, 5 2005.

[10] S. M. Kim, S. Wang, and M. J. Brennan, "Dynamic analysis and optimal design of a passive and an active piezo-electrical dynamic vibration absorber," *Journal of Sound and Vibration*, vol. 330, pp. 603–614, 2 2011.

[11] S. M. Kim, S. Wang, and M. J. Brennan, "Comparison of negative and positive position feedback control of a flexible structure," *Smart Materials and Structures*, vol. 20, 1 2011.

[12] S. Ito and G. Schitter, "Comparison and classification of high-precision actuators based on stiffness influencing vibration isolation," *IEEE/ASME Transactions on Mechatronics*, vol. 21, pp. 1169–1178, 4 2016.

[13] I. R. Petersen and A. Lanzon, "Feedback Control of Negative-Imaginary Systems," *IEEE Control Systems*, vol. 30, no. 5, pp. 54–72, 2010.

[14] I. R. Petersen, "Negative imaginary systems theory and applications," *Annual Reviews in Control*, vol. 42, pp. 309–318, 1 2016.

[15] S. Nima Mahmoodi and M. Ahmadian, "Active vibration control with modified positive position feedback," *Journal of Dynamic Systems, Measurement and Control, Transactions of the ASME*, vol. 131, pp. 1–8, 7 2009.

[16] E. Omidi and N. Mahmoodi, "Hybrid Positive Feedback Control for Active Vibration Attenuation of Flexible Structures," *IEEE/ASME Transactions on Mechatronics*, vol. 20, pp. 1790–1797, 8 2015.

[17] J. Warminski, M. Bochenski, W. Jarzyna, P. Filipek, and M. Augustyniak, "Active suppression of nonlinear composite beam vibrations by selected control algorithms," *Communications in Nonlinear Science and Numerical Simulation*, vol. 16, pp. 2237–2248, 5 2011.

[18] E. Omidi and S. N. Mahmoodi, "Nonlinear vibration control of flexible structures using nonlinear modified positive position feedback approach," in *ASME 2014 Dynamic Systems and Control Conference, DSCC 2014*, vol. 3, pp. 835–849, Kluwer Academic Publishers, 1 2014.

[19] E. Omidi and S. N. Mahmoodi, "Nonlinear integral resonant controller for vibration reduction in nonlinear systems," *Acta Mechanica Sinica/Lixue Xuebao*, vol. 32, pp. 925–934, 10 2016.

[20] G. Zhao, A. Paknejad, G. Raze, A. Deraemaeker, G. Kerschen, and C. Collette, "Nonlinear positive position feedback control for mitigation of nonlinear vibrations," *Mechanical Systems and Signal Processing*, vol. 132, pp. 457–470, 10 2019.

[21] M. Heertjes, S. Van Den Eijnden, B. Sharif, M. Heemels, and H. Nijmeijer, "Hybrid integrator-gain system for active vibration isolation with improved transient response," in *IFAC-PapersOnLine*, vol. 52, pp. 454–459, Elsevier, 1 2019.

[22] M. A. Mohan, M. B. Kaczmarek, and S. H. Hosseinnia, "Resetting Velocity Feedback: Reset Control for Improved Transient Damping," in *2022 European Control Conference, ECC 2022*, pp. 1421–1428, Institute of Electrical and Electronics Engineers Inc., 2022.

[23] M. J. Balas, "Direct Velocity Feedback Control of Large Space Structures," *Journal of Guidance and Control*, vol. 2, pp. 252–253, 5 1979.

[24] S. M. Kim, M. J. Brennan, and G. L. Abreu, "Narrowband feedback for narrowband control of resonant and non-resonant vibration," *Mechanical Systems and Signal Processing*, vol. 76-77, pp. 47–57, 8 2016.

[25] S. M. Kim, S. Wang, and M. J. Brennan, "Optimal and robust modal control of a flexible structure using an active dynamic vibration absorber," *Smart Materials and Structures*, vol. 20, p. 045003, 3 2011.

[26] G. Cazzulani, F. Resta, F. Ripamonti, and R. Zanzi, "Negative derivative feedback for vibration control of flexible structures," *Smart Materials and Structures*, vol. 21, p. 075024, 7 2012.

2

[27] H. H. Syed, "Comparative study between positive position feedback and negative derivative feedback for vibration control of a flexible arm featuring piezoelectric actuator," *International Journal of Advanced Robotic Systems*, pp. 1–9, 7 2017.

[28] O. Nishihara and T. Asami, "Closed-form solutions to the exact optimizations of dynamic vibration absorbers (minimizations of the maximum amplitude magnification factors)," *Journal of Vibration and Acoustics, Transactions of the ASME*, vol. 124, no. 4, pp. 576–582, 2002.

[29] C. J. Goh and T. K. Caughey, "On the stability problem caused by finite actuator dynamics in the collocated control of large space structures," *International Journal of Control*, vol. 41, no. 3, pp. 787–802, 1985.

[30] J. Dietrich, G. Raze, A. Deraemaeker, C. Collette, and G. Kerschen, "H∞ Tuning Rules for Positive Position Feedback Controllers: The Single-Degree-Of-Freedom Case and Beyond," *Journal of Vibration and Control*, vol. 0, p. 0, 7 2024.

[31] S. S. Aphale, A. J. Fleming, and S. O. Reza Moheimani, "Integral resonant control of collocated smart structures," *Smart Materials and Structures*, vol. 16, pp. 439–446, 2 2007.

[32] M. Namavar, A. J. Fleming, M. Aleyaasin, K. Nakkeeran, and S. S. Aphale, "An analytical approach to integral resonant control of second-order systems," *IEEE/ASME Transactions on Mechatronics*, vol. 19, no. 2, pp. 651–659, 2014.

[33] C. Collette, S. Janssens, and K. Artoos, "Review of Active Vibration Isolation Strategies," *Recent Patents on Mechanical Engineeringe*, vol. 4, no. 3, pp. 212–219, 2012.

[34] T. Van Der Poel, J. Van Dijk, J. B. Jonker, and H. M. Soemers, "Improving the vibration isolation performance of hard mounts for precision equipment," in *IEEE/ASME International Conference on Advanced Intelligent Mechatronics, AIM*, 2007.

[35] D. Tjepkema, J. Van Dijk, and H. M. Soemers, "Sensor fusion for active vibration isolation in precision equipment," *Journal of Sound and Vibration*, vol. 331, pp. 735–749, 2 2012.

[36] PI Ceramic, "Properties of Piezo Actuators: Electrical Operation of Piezo Actuators," 2021.

[37] M. A. Beijen, M. F. Heertjes, H. Butler, and M. Steinbuch, "H∞ feedback and feedforward controller design for active vibration isolators," in *IFAC-PapersOnLine*, vol. 50, pp. 13384–13389, Elsevier, 7 2017.

[38] L. van de Ridder, W. B. Hakvoort, D. M. Brouwer, J. van Dijk, J. C. Lötters, and A. de Boer, "Coriolis mass-flow meter with integrated multi-DOF active vibration isolation," *Mechatronics*, vol. 36, pp. 167–179, 6 2016.

[39] W. B. Hakvoort, G. J. Boerrigter, and M. A. Beijen, "Active vibration isolation by model reference adaptive control," in *IFAC-PapersOnLine*, vol. 53, pp. 9144–9149, Elsevier, 1 2020.

[40] C. G. Gordon, "Generic vibration criteria for vibration-sensitive equipment," in *Optomechanical Engineering and Vibration Control*, vol. 3786, pp. 22–33, SPIE, 9 1999.

[41] L. Jabben and J. Van Eijk, "Perfomance analysis and design of mechatronic systems," *Mikroniek*, vol. 51, no. 2, pp. 5–12, 2011.

[42] A. Paknejad, G. Zhao, M. Osée, A. Deraemaeker, F. Robert, and C. Collette, "A novel design of positive position feedback controller based on maximum damping and H2 optimization," *JVC/Journal of Vibration and Control*, vol. 26, pp. 1155–1164, 8 2020.

2

3

Active metamaterials for vibration control

The previous chapter presented a frequency-domain loop-shaping approach for the design of SISO AVC systems. Here, this approach is related to the design of active metamaterial structures with piezoelectric sensors and actuators for bandgap generation. The main challenge is the high number of control inputs and outputs characterizing active metamaterial structures. Counter-intuitively, the problem is simplified by assuming that the structure consists of infinitely many transducer pairs. The control of the metamaterial is then related in the modal domain to the simpler problems studied in the previous chapter. With these insights, the bandgap design is simplified, which we show experimentally in a setup with a few sparsely placed piezoelectric transducers.

Creating bandgaps in active piezoelectric slender beams through positive position feedback control

3

Abstract *Bandgaps - frequency ranges with reduced vibration transmissibility in elastic structures, are an opportunity for vibration control originating from the research on elastic metamaterials. In this paper, we study the design for bandgap in slender beams with collocated piezoelectric patch transducers. While creating bandgaps using shunted transducers is a well-established research field, using structures with piezoelectric sensors, actuators, and feedback controllers for the same application has not been thoroughly explored. This paper aims to study the use of the tools originating from the active vibration control (AVC) field for bandgap generation in finite beams with collocated piezoelectric sensors and actuators. Lightly damped second-order low-pass filters are used as controllers in the same configuration as positive position feedback (PPF), widely used for active damping. To facilitate the understanding of systems behaviour, we propose a simplified model based on the Euler-Bernoulli beam theory. A modal analysis approach and an assumption of an infinite number of transducers of infinitesimal length distributed along the structure are used to predict the frequency range of the locally resonant bandgap in closed form. The experimental part of the work demonstrates the feasibility of the proposed approach for creating bandgaps in practice. Thanks to the insights from AVC, the control system can be designed purely based on experimental frequency response data without the need for a parametric model of the system. We also show that the uniform distribution of actuators is not necessary for creating bandgap, which can be achieved in a structure with a relatively small number of sparsely placed actuators and compare the obtained results with analytical predictions for ideal metastructure. Low-frequency bandgaps placed between 10 and 320 Hz are obtained in experiments.*

3.1 Introduction

A bandgap, in the context of flexible structures, refers to a specific range of frequencies where the magnitude of the structures transmissibility is lower than 1. The idea originates from the research on elastic metamaterials but is promising for applications beyond this narrow field, for example, in vibration isolation of structures excited by narrow-band disturbances. Here, we focus on creating bandgaps in finite slender beams. For such structures, using piezoelectric patch transducers to obtain a bandgap is an appealing solution. Compact, highly integrated designs with such transducers can easily be created using

existing, well-established technologies, and piezoelectric patch transducers can be easily retrofitted on existing components. Moreover, such a structure can have high stiffness, which is beneficial in many applications [1].
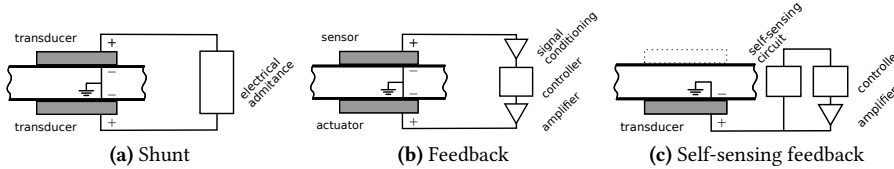
Figure 3.1: Different configurations for vibration control in slender structures with piezoelectric transducers. In (a), all the transducers have the same role and the shunt is designed as an electrical impedance. In (b), transducers are divided into sensors and actuators, and the feedback controller can be seen as generalized stiffness. In configuration (c), only actuators are used in the system and the displacements at their locations, necessary to implement the feedback loop, are recovered using dedicated circuits.

The methods for vibration control in piezoelectric smart structures can be divided into three categories, depending on the transducers' role, as illustrated in Fig. 3.1. While our focus is on feedback systems presented in 3.1b, we also provide a description of the two remaining, with some representative examples from literature. Active and passive electronic elements and discrete controllers can be used in all the configurations. All the configurations can be used to implement tuneable or adaptive systems. Moreover, in all cases, careless design and ignoring parasitic dynamics or time delays present in the system may result in instability.

In the approach presented in Fig. 3.1a, piezoelectric transducers are shunted using electric or electronic circuits [2]. The majority of the results on bandgap creation in systems with piezoelectric transducers can be assigned to this category. Since the related literature is vast, we do not aim to provide an extensive review. Instead, we refer to a few selected papers with representative examples. All the transducers used in such a structure have the same role and are influenced in the same manner by the presence of the shunt (this is clearly seen when compared with feedback systems in Fig. 3.1b, see e.g. the section on modeling in [3]). Single or connected transducers (like in Fig.3.1a) can be used. The structure dynamics are altered due to the coupling with the shunt dynamics, which are often seen as a relationship between currents and voltages acting on the transducers. Active shunts can be implemented as "voltage-controlled current-sources" [4, 5], which offer greater design freedom and stronger influence on the structure's properties, for example, when "negative capacitance" shunts are used [6–9].

In the structure presented in Fig. 3.1b, transducers are divided into two groups: sensors and actuators, which operate under different conditions. Here, we only provide a brief description of the category and elaborate on the examples from the literature that fit it later in this section. The charge measured on the sensor is related to generalized displacement at its location. The external voltage applied to the actuator results in a generalized force applied to the structure [10]. The relationship between the signals of actuators and sensors can be seen as generalized stiffness. In the electronic circuits used to implement

such a structure, subsystems for sensor signal conditioning, implementation of controller dynamics, and amplification of actuator signals can be identified. Both collocated and non-collocated sensors and actuators can be used.

In the approach presented in Fig. 3.1c, the transducers are used in the self-sensing mode. The self-sensing refers to a single component acting as a sensor and actuator in a control system. While the term *self-sensing* is sometimes used to describe shunt circuits, like the one presented in Fig. 3.1a [11], there are other ways to implement this concept in vibration control with piezoelectric transducers. An overview of available methods can be found in [12]. While all the transducers in the system have the same role, the voltages applied to transducers are calculated based on the generalized displacements recovered by dedicated electronic circuits. For this reason, the same design approaches as for feedback systems presented in Fig. 3.1b can be used. To the best of our knowledge, this approach has not been used yet for the creation of bandgap in slender structures.

While the use of piezoelectric structures with shunts for bandgap creation is well-researched, the two other options have been neglected. The few results utilising feedback are based on simple control methods, where the voltage of the sensor is proportional to the sensor voltage (related to generalised displacements) [13], its derivative w.r.t. time (related to generalised velocities), its second derivative w.r.t. time (related to generalised accelerations) [14, 15] or a linear combination of those terms [16] are used. In this way, the unit cells' effective stiffness, damping or inertia are altered. Numerical analyses presented in these papers demonstrate widened bandgap regions, dependent on the controller gains when active feedback is used. While all aforementioned papers use collocated sensors and actuators, non-collocation is used to obtain non-reciprocal properties in [17].

In the scope of the classification presented in Fig. 3.1, the results utilising enhanced shunting circuits should also be categorised as feedback systems. The enhanced circuits presented in [3, 18, 19] consist of two collocated piezoelectric patch transducers. While the properties of one (the actuator) are influenced by the resonators present in the circuits, the other remains uninfluenced and acts as a sensor. In [19], the feedback loop consisting of a charge amplifier for sensor signal conditioning, a microprocessor for implementation of a digital controller and an actuator amplifier is studied. Feedback loops implemented in structures with collocated sensors and actuators using only analogue electronic elements have been used in [3, 18]. In all three papers, the influence of the feedback system on the structure was modelled by introducing frequency-dependent elastic moduli of the actuators, defined by the feedback loop dynamics. Dispersion properties of infinite metamaterial were analyzed using Bloch's boundary condition, and the behaviour of finite metastructures was shown experimentally.

Generating bandgaps in structures with sensors and actuators by actively implementing resonant dynamics in the feedback loop is a neglected research direction with great potential. The use of such smart structures for resonance peak damping, which is a closely related topic to bandgap creation, is well researched, and this knowledge can be translated to the bandgap problem (see examples in [10, 20]). While the feedback configuration is an alternative to commonly used shunt circuits, we do not claim it is better in any sense. We expect each configuration to have benefits and drawbacks depending on the application.

In this paper, we study bandgap generation in finite beams with collocated piezoelectric patch sensors and actuators, with the controller implemented digitally. To the best

of our knowledge, the only paper studying such a configuration is [19]. What differentiates this work from [19] are the modeling and control approaches used. Lightly damped second-order low-pass filters are used as controllers, in the same configuration as in the positive position feedback (PPF) [10, 21] widely used for active damping. From the control theory perspective, bandgap generation in a finite structure is a rather simple problem, and the stability of the system can be easily assured using the Negative Imaginary (NI) systems theory if the underlying assumptions are satisfied [22]. For this reason, these aspects are not presented in the paper. The major advantage of the proposed control approach is that the practical design of the controller can be based on the experimental frequency domain data, without a need for a parametric model of the system. The paper's contributions focus on modelling the system, predicting the bandgap region in a finite structure and implementing the proposed approach practically.

To facilitate the understanding of systems behaviour, we propose a simplified model based on the Euler-Bernoulli beam theory, where the influence of each of the actuators is represented by a pair of moments related to the signal of the corresponding sensor. Bandgap analysis and predictions in [19] are based on the assumption of travelling waves in an infinite medium. However, this approach ignores the characteristics of finite structures and does not take advantage of the modal representation typically used for the analysis of such structures [23]. A method to predict a locally resonant bandgap in piezoelectric beams in shunt configuration under the assumption of an infinite number of transducers applied was developed in [24]. The approach was extended to piezoelectric metamaterial plates in shunt configuration in [25]. As a contribution of this work, we adopt the method developed in [24] to the piezoelectric metamaterial beams in sensor-actuator configuration and estimate the influence of a feedback loop on such a structure in a closed form under the same assumptions. The estimation is valid for arbitrary feedback loop dynamics that can be designed for active damping, bandgap generation or other objectives.

In the experimental part of the paper, we demonstrate that bandgap (seen as a significant reduction of vibration transmissibility magnitude below 1 at a selected frequency range) can be created in practice with the sensor and actuator configuration and feedback control. To the best of our knowledge, we are first to report such an achievement, as in [19], only resonance peak attenuation was presented experimentally using the studied configuration. We also show that the uniform distribution of actuators is not necessary for creating bandgap, which can be achieved in a structure with a relatively small number of sparsely placed actuators. We also acknowledge the importance of parasitic effects, not captured in the theoretical models and show their influence on the obtained bandgap by conducting numerical analysis in parallel to experiments.

The structure of the paper is as follows. Section 3.2 presents the model of the studied structures and the considered control system architecture. In Section 3.3, we study the bandgap in metastructure using the assumption that an infinite number of transducers are placed on the structure. In Section 3.4, we focus on smart structures with sparsely placed transducers and creating bandgaps in practice. Section 3.5 concludes the paper.

3.2 System description

The purpose of the model derived here is to provide insights into the behaviour of the system. The controllers used in the physical setup and presented in Section 4 are tuned based on experimentally measured frequency response functions of the structure instead of analytical models. For this reason, a possibly simple model, not including the minute details of the system, is derived.

The system under consideration is schematically presented in Fig. 3.2. It consists of a beam with a rectangular cross-section embedded with S collocated piezoelectric sensor and actuator pairs. The objective of the control system is to limit the influence of base excitation and external disturbance forces on the vibrations of the structure at the point of interest at a targeted frequency range. The model of the structure, including the mechanical and electrical domains, which has been adopted from [24] by implementing the relationship between the sensor signal, controller and voltage applied to the actuator, is presented in subsection 3.2.1. Section 3.2.2 presents the control-related aspects of the system.

3.2.1 Model of the system

We assume the beam has a constant cross-section consisting of two continuous and symmetrically located piezoelectric layers sandwiching a central substrate. The piezoelectric layers are poled in the thickness direction. The electrodes are segmented, forming transducer pairs on opposite sides of the beam, such that transducers in one layer have the role of sensors and, in the other, act as actuators. The electrode layers and bonding layers are treated as having negligible thickness. The slender composite beam, subject to specified boundary conditions, is modelled based on the Euler-Bernoulli beam theory, presuming geometrically small oscillations and linear-elastic material behaviour. For simplicity, it is assumed that the beam is undamped; however, the modal damping can be easily introduced later in the analysis.

In the model, the bending centre is assumed to be located at the geometric centre of the beams cross-section. However, due to the use of the sensor and actuator configuration of the piezoelectric transducers, the response of the bottom piezoelectric patch would be strongly distinguished from the upper one, which leads to a mismatch of the geometric centre and the bending centre locations and limited accuracy of the model. Nevertheless, the model sufficiently captures the system behaviour.

For the structure excited by some base displacement $w_b(t)$ and external transverse force with density $f(x, t)$ with relative vibration $w(x, t)$, the governing equations in physical coordinates are

$$EI \frac{\partial^4 w}{\partial x^4} + m \frac{\partial^2 w}{\partial t^2} - k_A \vartheta \sum_{j=1}^{S} v_{2,j}(t) \frac{\mathrm{d}^2}{\mathrm{d}x^2} \left[H\left(x - x_j^L\right) - H\left(x - x_j^R\right) \right] = -m(x)\ddot{w}_b(t) + f(x, t)$$

$$\tag{3.1}$$

$$q_{1,j}(t) = k_S \vartheta \Delta w'_j \tag{3.2}$$

$$\ddot{y}(t) = \ddot{w}(x_T, t), \tag{3.3}$$
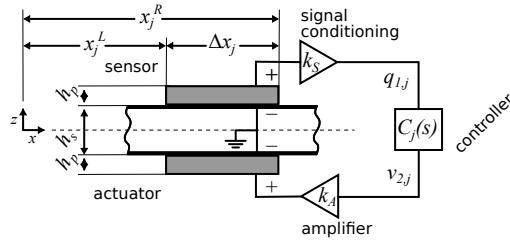
Figure 3.2: Schematic representation of the considered system. To simplify the modelling of the structure, the influence of the signal conditioning and actuator amplifiers are included in the model of the beam and represented by static gains. This approach is in line with the common practice in experimental system identification.

where $w(x, t)$ is the transverse displacement of the beam at position x and time t, and $H(x)$ is the Heaviside function. $\ddot{y}(t)$ denotes the acceleration at the point of interest x_T. The segmented electrodes are numbered $j = 1 \dots S$, with each electrode starting at $x = x_j^L$ and ending at $x = x_j^R$ with the total length $\Delta x_j = x_j^R - x_j^L$. The voltage $v_{2,j}(t)$ applied to the jth actuator is generated by an external amplifier with amplification factor k_A. The charge $q_{1,j}(t)$ measured at the jth sensor is proportional to the difference of slopes at the extremities of the transducer $\Delta w_j' = w'(x_j^R) - w'(x_j^L)$[10], with a factor dependent of the signal conditioning circuit k_S. Furthermore, EI is the short circuit flexural rigidity, m is the mass per length, and ϑ is the electromechanical coupling term in physical coordinates, given by

$$EI = \frac{2b}{3} \left(c_s \frac{h_s^3}{8} + \bar{c}_{11}^E \left[\left(h_p + \frac{h_s}{2} \right)^3 - \frac{h_s^3}{8} \right] \right) \tag{3.4}$$

$$m = b \left(\rho_s h_s + 2\rho_p h_p \right) \tag{3.5}$$

$$\vartheta = \bar{e}_{31} b \left(h_s + h_p \right) \tag{3.6}$$

where c_s, ρ_s, and h_s are the central substrate layer's elastic modulus, mass density, and thickness, respectively, while b is the width of the beam. The piezoelectric layers have mass density ρ_p, thickness h_p, width b, elastic modulus at constant electric filed $\bar{c}_{11}^E$, effective piezoelectric stress constant $\bar{e}_{31}$, and permittivity component at constant strain $\bar{\varepsilon}_{33}^S$, where the overbars indicate effective material properties for 1D thin layers reduced from 3D constitutive equations as

$$\bar{c}_{11}^E = \frac{1}{s_{11}^E} \qquad\qquad \bar{e}_{31} = \frac{d_{31}}{s_{11}^E}$$

where s_{11}^E is the elastic compliance at constant electric field, d_{31} is the piezoelectric strain constant.

Using an assumed-modes type expansion with N modes, the transverse displacement of

the beam is expanded as

$$w(x,t) = \sum_{r=1}^{N} \phi_r(x)\eta_r(t) \tag{3.7}$$

where $\eta_r(t)$ are the modal weighting and $\phi_r(t)$ are the mode shapes of the beam for a given set of boundary conditions (at short circuit) normalized such that

$$\int_0^L m\phi_r(x)\phi_s(x) = \delta_{r,s}, \quad r,s = 1,2,\dots \tag{3.8}$$

$$\int_0^L EI\phi_r(x)\frac{\mathrm{d}^4\phi_s}{\mathrm{d}x^4}\,dx = \omega_r^2\delta_{rs}, \quad r,s = 1,2,\dots \tag{3.9}$$

where L is the length of the beam, ω_r is the rth natural frequency, and δ_{rs} is the Kronecker delta. Note that (3.9) can be written in symmetric form

$$\int_0^L EI\frac{\mathrm{d}^2\phi_r}{\mathrm{d}x^2}\frac{\mathrm{d}^2\phi_s}{\mathrm{d}x^2}\,dx = \omega_r^2\delta_{rs}, \quad r,s = 1,2$$

Substituting (3.7) into (3.1)-(3.3), multiplying by some mode shape $\phi_k(x)$, and integrating across the beam, the governing equations can be obtained in modal coordinates as

$$\ddot{\eta}_r(t) + \omega_r^2\eta_r(t) - k_A\vartheta\sum_{j=1}^{S} v_{2,j}(t)\Delta\phi'_{r,j} = q_{w,r}(t) + q_{f,r}(t) \tag{3.10}$$

$$q_{1,j}(t) = k_S\vartheta\sum_{r=1}^{N} \Delta\phi'_{r,j}\eta_r(t) \tag{3.11}$$

$$\ddot{y}(t) = \ddot{w}_b(t) + \sum_{r=1}^{N} \phi_r(x_T)\ddot{\eta}_r(t) \tag{3.12}$$

where the free indices r and j are assumed to go from $1\dots N$ and $1\dots S$, respectively,

$$\Delta\phi'_{r,j} = \left(\frac{\mathrm{d}\phi_r}{\mathrm{d}x}\right)_{x_j^L}^{x_j^R} = \frac{\mathrm{d}\phi_r}{\mathrm{d}x}\left(x_j^R\right) - \frac{\mathrm{d}\phi_r}{\mathrm{d}x}\left(x_j^L\right)$$

is the difference in slope of the rth mode between the ends of the jth electrode and the modal forcing is given by

$$q_{w,r}(t) = -\ddot{w}_b(t)\int_0^L m\phi_r(x)dx, \tag{3.13}$$

$$q_{f,r}(t) = \int_0^L f(x,t)\phi_r(x)dx. \tag{3.14}$$

Taking the Laplace transform of the governing equations we obtain

$$\left(s^2 + \omega_r^2\right) H_r(s) - k_A \vartheta \sum_{j=1}^{S} V_{2,j}(s) \Delta\phi'_{r,j} = Q_{w,r}(s) + Q_{f,r}(s) \tag{3.15}$$

$$Q_{1,j}(s) = k_S \vartheta \sum_{r=1}^{N} \Delta\phi'_{r,j} H_r(s) \tag{3.16}$$

$$\ddot{y}(s) = \ddot{w}_b(s) + \sum_{r=1}^{N} \phi_r(x_T) s^2 H_r(s), \tag{3.17}$$

where, with some abuse of the notation, $H_r(s), V_{2,j}(s), Q_{1,j}(s), Y(s), Q_{w,r}(s), Q_{f,r}(s)$ denote Laplace transforms of the time signals $\eta_r(t), v_{2,j}(t), q_{1,j}(t), y(t), q_{w,r}(t), q_{f,r}(t)$.
To study the transmissibility of the system, it is beneficial to express the base excitation in terms of acceleration. This leads to the modal forcing in the Laplace domain

$$Q_{w,r}(s) = -\ddot{w}_b(s) \int_0^L m\phi_r(x)dx. \tag{3.18}$$

Focusing on the measurable signals we have then

$$Q_{1,j}(s) = k_S k_A \vartheta^2 \sum_{k=1}^{S} \sum_{r=1}^{N} \frac{\Delta\phi'_{r,j}\Delta\phi'_{r,k}}{s^2 + \omega_r^2} V_{2,k}(s) - k_S \vartheta \sum_{r=1}^{N} \frac{\Delta\phi'_{r,j}}{s^2 + \omega_r^2} \int_0^L m\phi_r(x)dx \; \ddot{w}_b(s) \tag{3.19}$$

$$\ddot{y}(s) = k_A \vartheta \sum_{k=1}^{S} \sum_{r=1}^{N} \frac{s^2 \phi_r(x_T)\Delta\phi'_{r,k}}{s^2 + \omega_r^2} V_{2,k}(s) + \ddot{w}_b(t) - \sum_{r=1}^{N} \frac{s^2 \phi_r(x_T)}{s^2 + \omega_r^2} \int_0^L m\phi_r(x)dx \; \ddot{w}_b(s). \tag{3.20}$$

Taking into account that

$$\sum_{r=1}^{N} \phi_r(x_T) \int_0^L m\phi_r(x)dx = 1 \tag{3.21}$$

we have

$$\frac{\ddot{y}(s)}{\ddot{w}_b(s)} = 1 - \sum_{r=1}^{N} \frac{s^2 \phi_r(x_T)}{s^2 + \omega_r^2} \int_0^L m\phi_r(x)dx = \sum_{r=1}^{N} \phi_r(x_T) \int_0^L m\phi_r(x)dx \frac{\omega_r^2}{s^2 + \omega_r^2}. \tag{3.22}$$

3.2.2 Control structure

The controller dynamics describe the relationship between the measured sensor outputs and actuation inputs. While various control architectures are available in the literature, we consider only a multi-SISO (single-input, single-output) structure, where the voltage applied to jth actuator $v_{2,j}(t)$ depends only on the charge measured at the corresponding jth sensor $q_{1,j}(t)$

$$V_{2,j}(s) = C_j(s)Q_{1,j}(s). \tag{3.23}$$

A positive feedback interconnection is used. When the piezoelectric sensor and actuator are collocated, the transfer function between the corresponding signals

$$G_{Q_j/V_j}(s) = \frac{Q_{1,j}(s)}{V_{2,j}(s)} = k_S k_A \vartheta^2 \sum_{r=1}^{N} \frac{\Delta\phi'_{r,j}\Delta\phi'_{r,j}}{s^2 + \omega_r^2} \tag{3.24}$$

has the characteristic pattern of alternating poles and zeros, which can be used to guarantee the stability of the SISO control system. In a MIMO (multiple-input, multiple-output) case, the stability properties of flexible structures with collocated sensors and actuators are captured by the negative-imaginary (NI) systems theory [22]. Transfer functions of finite flexible structures with collocated (generalized) force inputs and (generalized) position outputs, like the one of the system considered in this paper, are strictly negative imaginary [22].

A positive-position feedback (PPF)[10, 21] controllers in the SISO form are used, described by

$$C(s) = \frac{k_c}{s^2/\omega_c^2 + 2s\zeta_c/\omega_c + 1}, \tag{3.25}$$

where $\omega_c, \zeta_c, k_c > 0$. The transfer function of PPF is characterized by a resonance peak, and thanks to the roll-off at high frequencies, the controller can be implemented in practice, as this minimizes the risk of destabilizing the system in the presence of parasitic dynamics and time delays.

To simplify the design of the control system, controllers for all transducer pairs have the same strictly NI dynamics $C(s)$ with individually selected gains. We select the gain for each controller C_j to be equal to the inverse of the steady-state value of the transfer function between $Q_{1,j}$ and $V_{2,j}$

$$C_j(s) = g_j C(s), \quad g_j = G_{Q_j,V_j}^{-1}(0). \tag{3.26}$$

With this control structure, the stability of the closed-loop system can be concluded using the NI theory when $C(0) \leq 1$.

Any experimental system inevitably includes parasitic dynamics and time delays. It is, therefore, essential to ensure that the dynamics of the structure can be accurately captured by an NI model in the relevant frequency range. Additionally, evaluating the stability margins of the collocated pairs $G_{Q_j,V_j}(s)C_j(s)$ is a quick way to notice possible challenges for the systems stability.

3.3 Bandgap in active metastructures

In this section, we consider bandgap formation using the feedback approach in a metastructure, which is a finite structure consisting of repeated identical unit cells. In subsection 3.3.1, we provide an approximate analysis method under the assumption of the infinite number of transducers applied. In subsection 3.3.2, show the influence of the PPF controller on the bandgap generation. In subsection 3.3.3, we validate the developed method and show its applicability for structures with a finite number of transducers in a numerical analysis.

3.3.1 Ideal case with $S \to \infty$ and $\Delta x_j \to 0$

In this section, using the approach introduced in [24], we approximate the dynamics of the system as $S \to \infty$ and $\Delta x_j \to 0$. A closed-loop description of the considered control system can be obtained by substituting (3.26),(3.16) into (3.15)

$$\left(s^2 + \omega_r^2\right) H_r(s) - k_S k_A \vartheta^2 \sum_{j=1}^{S} \sum_{k=1}^{N} \Delta\phi'_{k,j} \Delta\phi'_{r,j} C_j(s) H_k(s) = Q_{w,r}(s) + Q_{f,r}(s) \tag{3.27}$$

The system of equations described by (3.27) cannot be readily solved for a simple analytical expression for the modal weightings $H_r(s)$ due to the coupling from the presence of transducers.

For each transducer pair, the gain of the controller is related to the steady-state value of the transfer function between the charge and voltage in the pair, as described in (3.26). Using (3.2) in the physical coordinates, for infinitesimally long transducers we have

$$\lim_{\Delta x_j \to 0} q_{1,j} = k_S \vartheta \Delta w'_j = k_S \vartheta \frac{\Delta w'_j}{\Delta x_j} \Delta x_j = k_S \vartheta \frac{d^2 w}{dx^2}(x_j)\Delta x_j. \tag{3.28}$$

The influence of the voltage $v_{2,j}$ applied to the jth actuator can be represented by a pair of moments $M_j = -k_A \vartheta v_{2,j}$ acting at the actuator's extremities [10]. The relationship between the voltage $v_{2,j}$ applied to the jth transducer and the local curvature of the beam is then

$$\frac{d^2 w}{dx^2}(x_j) = \frac{-1}{EI} M = k_A \frac{\vartheta}{EI} v_{2,j}. \tag{3.29}$$

Combining the two formulas we get

$$\lim_{\Delta x_j \to 0} q_{1.j} = k_S k_A \frac{\vartheta^2}{EI} \Delta x_j v_{2,j}, \tag{3.30}$$

$$\lim_{\Delta x_j \to 0} G_{Q/V,j}(0) = k_S k_A \frac{\vartheta^2}{EI} \Delta x_j. \tag{3.31}$$

By combining (3.27) with (3.26) and (3.31) we have

$$H_r(s)\left(s^2 + \omega_r^2\right) - k_S k_A \vartheta^2 \sum_{j}^{S} \sum_{k}^{N} \Delta\phi'_{k,j} \Delta\phi'_{r,j} \frac{EI}{k_S k_A \vartheta^2} \frac{1}{\Delta x_j} C(s) H_r(s) = Q_{w,r}(s) + Q_{f,r}(s) \tag{3.32}$$

$$H_r(s)\left(s^2 + \omega_r^2\right) - C(s) \sum_{k}^{N} \sum_{j}^{S} EI \frac{\Delta\phi'_{k,j}}{\Delta x_j} \frac{\Delta\phi'_{r,j}}{\Delta x_j} \Delta x_j H_r(s) = Q_{w,r}(s) + Q_{f,r}(s) \tag{3.33}$$

In the limit as $\Delta x_j \to 0$, $S \to \infty$

$$\lim_{S \to \infty} \lim_{\Delta x_j \to 0} \sum_{j}^{S} EI \frac{\Delta\phi'_{k,j}}{\Delta x_j} \frac{\Delta\phi'_{r,j}}{\Delta x_j} \Delta x_j = \int_0^L EI \frac{d^2\phi_k}{dx^2} \frac{d^2\phi_r}{dx^2} dx = \omega_r^2 \delta_{kr}. \tag{3.34}$$

Although this simplification is only exact in the limiting case, it can serve as a good approximation for a finite number of electrodes, as has been shown in [24] for piezoelectric structures with shunts. Equation (3.33) then becomes

$$H_r(s)\left(s^2 + \omega_r^2\right) - C(s)\omega_r^2 H_r(s) = Q_{w,r}(s) + Q_{f,r}(s).\tag{3.35}$$

The transfer function

$$\frac{H_r(s)}{Q_{w,r}(s)} = \frac{H_r(s)}{Q_{f,r}(s)} = \frac{1}{s^2 + \omega_r^2\left(1 - C(s)\right)}\tag{3.36}$$

can be used to predict the bandgap location for certain excitations, for example, see [24], where the vibrations of the beam are excited by one of the piezoelectric patch transducers. It can be interpreted as generalized compliance, where the presence of the piezoelectric transducers and control systems leads to a frequency-dependent dynamic modal stiffness $1 + C(s)$.

When the goal of the bandgap is to prevent the excitation of a system by base vibrations, the relationship between $\ddot{y}$ and $\ddot{w}_b$ has to be considered. Taking into account (3.17), (3.18) and (3.21) we get

$$\begin{aligned}
T(s) = \frac{\ddot{y}(s)}{\ddot{w}_b(s)} &= 1 - \sum_r^N \frac{s^2}{s^2 + \omega_r^2\left(1 - C(s)\right)}\phi_r(x_L)\int_0^L m\phi_r(x)dx \\
&= \sum_r^N \phi_r(x_L)\int_0^L m\phi_r(x)dx\left(\frac{\omega_r^2\left(1 - C(s)\right)}{s^2 + \omega_r^2\left(1 - C(s)\right)}\right).
\end{aligned}\tag{3.37}$$

The results presented in (3.36) and (3.37) represent the influence of controller dynamics on bandgap generation and are valid for arbitrary controllers designed as described in (3.26). Note, that the generalized compliance (3.36) can be rewritten as

$$\frac{H_r(s)}{Q_{f,r}(s)} = \frac{1}{s^2 + \omega_r^2}\frac{1}{1 - \frac{1}{s^2 + \omega_r^2}\omega_r^2 C(s)},\tag{3.38}$$

which is equivalent to a feedback interconnection of the dynamics of the structure in the absence of the controller and the term related to the controller $-\omega_r^2 C(s)$. Using this, suitable controllers for generating bandgap in considered systems can be found by using the loop-shaping approach demonstrated in [26]. The same relationships could be used to find optimal controllers for such an application.

3.3.2 Bandgap generation with PPF

This section shows the feasibility of creating a bandgap with a PPF controller using relations (3.36) and (3.37). For (3.25) we obtain

$$\frac{H_r(s)}{Q_{f,r}(s)} = \frac{s^2/\omega_c^2 + 2\zeta_c s/\omega_c + 1}{(s^2 + \omega_r^2)(s^2/\omega_c^2 + 2\zeta_c s/\omega_c + 1) - k_c\omega_r^2},\tag{3.39}$$

which is characterized by an anti-resonance at frequency ω_c and leads to bandgap boundaries

$$\omega_c \sqrt{1 - k_c} < \omega < \omega_c. \tag{3.40}$$

As in the classical active-damping case, the use of PPF leads to softening of the structure which can be seen by taking the steady-state value of (3.39) $\omega_r^{-2}(1 - k_c)^{-1}$. When the PPF controller (3.25) is used directly in (3.37) we obtain

$$T(s) = \sum_r^N \phi_r(x_L) \int_0^L m\phi_r(x)dx \left(\frac{\omega_r^2 \left(s^2/\omega_c^2 + 2\zeta_c s/\omega_c + 1 - k_c \right)}{(s^2 + \omega_r^2)(s^2/\omega_c^2 + 2\zeta_c s/\omega_c + 1) - k_c\omega_r^2} \right), \tag{3.41}$$

which, in the absence of damping, is characterized by an anti-resonance at $\omega_c \sqrt{1 - k}$. The poles of the transfer functions remain within the limits described in (3.40), so the bandgap will appear at the same range of frequencies. The relationship (3.40) suggests that with the gain $k_c = 1$ it is possible to create a marginally stable structure with a bandgap region spanning from the static regime to arbitrarily high frequency ω_c. However, due to time delays and parasitic dynamics present in any physical control system, the useable values of k_c and ω_c are limited for stability reasons.

The antiresonance in the transmissibility of a metastructure with a PPF controller not overlapping with the corner frequency of the controller ω_c may be inconvenient in many applications. For this reason, we propose a modified description for the controller

$$C(s) = \frac{k_c}{s^2/\omega_c^2 + 2s\zeta_c/\omega_c + 1 + k_c}, \tag{3.42}$$

which results in

$$\frac{H_r(s)}{Q_{f,r}(s)} = \frac{s^2/\omega_c^2 + 2\zeta_c s/\omega_c + 1 + k_c}{(s^2 + \omega_r^2)\left(s^2/\omega_c^2 + 2\zeta_c s/\omega_c + 1\right) + k_c s^2}, \tag{3.43}$$

$$T(s) = \sum_r^N \phi_r(x_L) \int_0^L m\phi_r(x)dx \left(\frac{\omega_r^2(s^2/\omega_c^2 + 2\zeta_c s/\omega_c + 1)}{\left((s^2 + \omega_r^2)(s^2/\omega_c^2 + 2\zeta_c s/\omega_c + 1) + k_c s^2\right)} \right). \tag{3.44}$$

In this case, the bandgap boundaries are

$$\omega_c < \omega < \omega_c \sqrt{1 + k_c}, \tag{3.45}$$

and an antiresonance at frequency ω_c appears in the transmissibility transfer function. The control system with (3.42) should be stable for any $k_c > 0$ in the absence of parasitic dynamics and time delays.

3.3.3 Finite number of transducers and validation of the bandgap size

In this subsection, we show that the infinite-transducer approximation and the resulting bandgap region predictions are accurate, for a sufficient number of uniformly distributed transducer pairs. All the controllers corresponding to the transducer pairs are tuned with the same parameters, as described in Subsection 3.2.2. Consider a uniform cantilever beam

of length L with S evenly spaced transducer pairs, such that $x_j^L = (j-1)L/S, x_j^R = jL/S$. The numerical studies presented here focus on the beam excited by the base motion. The systems response and the resonance frequencies can be obtained using the description in the modal domain (3.15),(3.16),(3.17) and common dynamical system techniques. Sets of plots showing the resonant frequencies and the transmissibility from base excitation to the tip acceleration for the cantilever beam are shown in Fig. 3.3 and Fig. 3.4.

Figure 3.3 shows the influence of the gain k_c on the width of the bandgap. The subsequent plots were generated using controllers with different values of k_c and the same remaining parameters. The bandgap region is indicated in the transmissibility plot by a reduction of magnitude over a range of frequencies. The solid lines in the plots highlight the resonant frequencies ω_S, ω_{S+1}, which according to [23] indicate the effective bandgap span. As S increases, the bandgap region converges to the theoretical prediction in (3.40). For increasing values of k_c the width of the badgap region increases in line with the prediction. What is interesting, for a structure with 4 transducer pairs, a wider region of transmissibility reduction can be seen, despite the presence of some resonance peaks within it.

Figure 3.4 shows the influence of the corner frequency ω_c on the behaviour of the system. The subsequent plots were generated using controllers with different values of ω_c and the same remaining parameters. The number of transducer pairs required for the limits of the bandgap region to converge to the theoretical prediction increases with the increasing ω_c. This may be related to the spatial resolution of the transducer array necessary for the shapes of the higher-frequency modeshapes.

In the studied cases of the active piezoelectric metastructure with a PPF controller, if the gain k_c is sufficiently high, the highest effective bandgap width achieved is the same as the theoretically predicted value (3.40). This is a different behaviour than in the case of metastructures with shunted piezoelectric transducers in [27] and metastructures with mechanical resonators in [23]. This may depend on the dynamics of the control element used and may require further investigation. Moreover, in some cases (for example Fig. 3.3b with $S = 4$) the transmissibility of the structure is lowered in a range of frequencies despite the presence of resonance peaks in the same range.

(a) $k_c = 0.1$

(b) $k_c = 0.5$

(c) $k_c = 0.9$
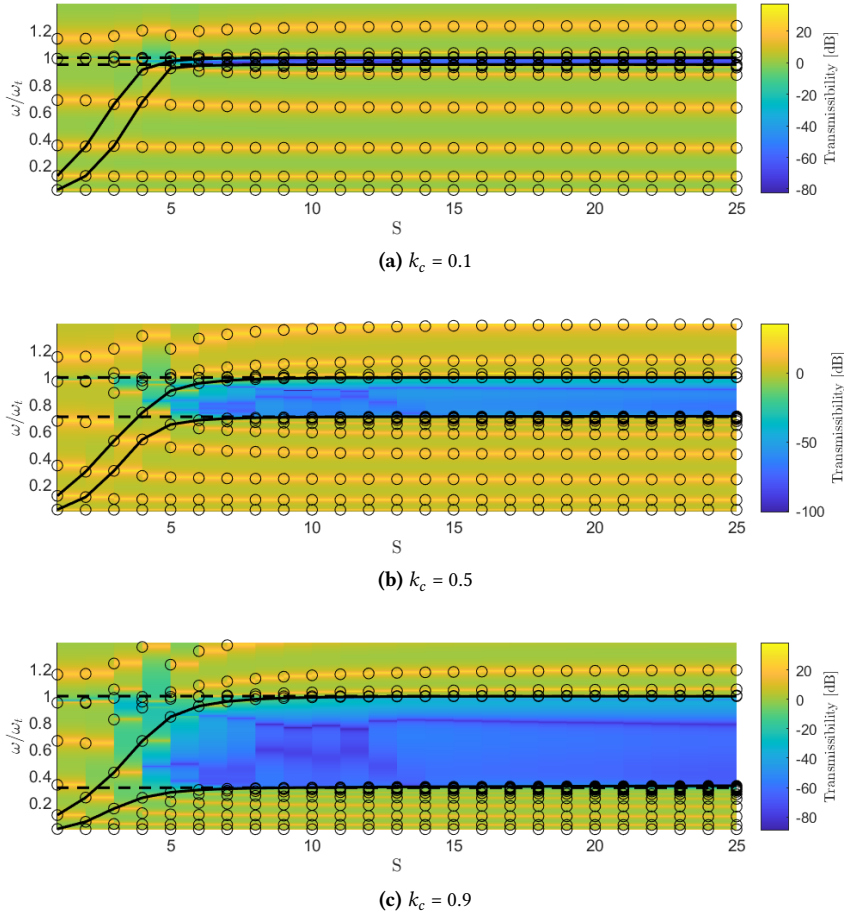
Figure 3.3: Transmissiblity and resonances of a finite length piezoelectric metastructure versus the number of unit cells S. Subfigures present the results for PPF controllers tuned target frequency $\omega_c = 50\omega_1$ with different controller gains k_c. Small circles indicate resonant frequencies of the full system, and the heatmap shows transmissibility on a log scale. Dashed lines show the expected bandgap edge frequencies for sufficiently large numbers of transducers. Solid lines track two resonances of the full system, ω_S and ω_{S+1}.

3

(a) $\omega_t = 5\omega_1$

(b) $\omega_t = 50\omega_1$

(c) $\omega_t = 300\omega_1$
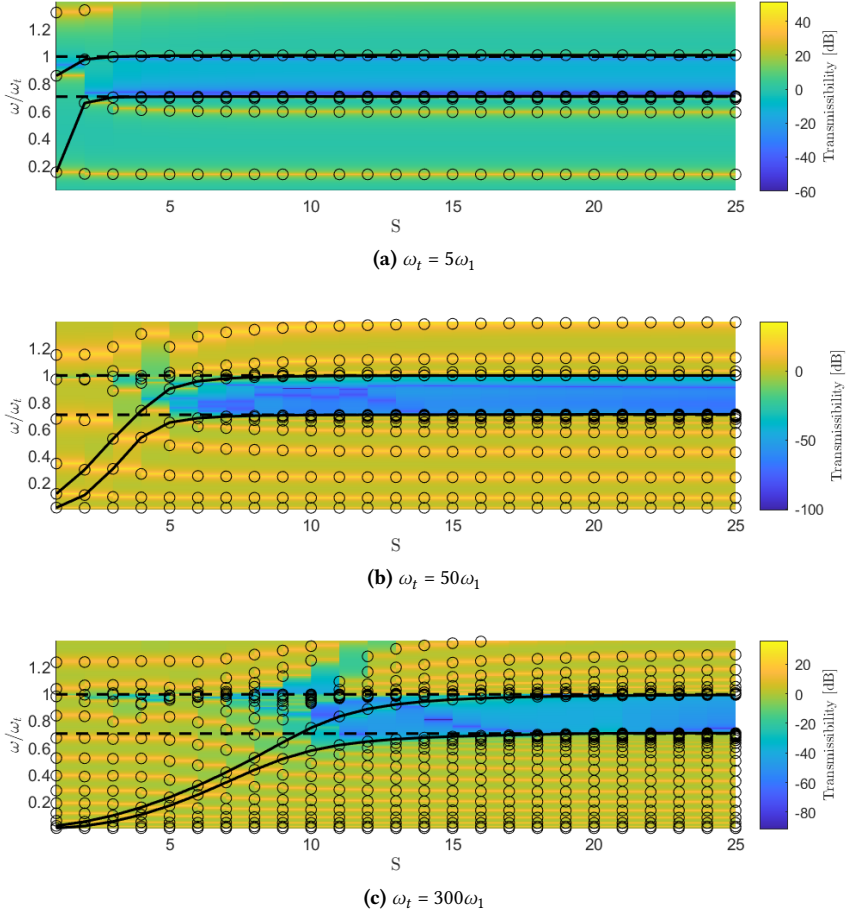
Figure 3.4: Transmissiblity and resonances of a finite length piezoelectric metastructure versus the number of unit cells S. Subfigures present the results for PPF controllers tuned with different target frequencies ω_c and the same controller gain $k_c = 0.5$. Small circles indicate resonant frequencies of the full system, and the heatmap shows transmissibility on a log scale. Dashed lines show the expected bandgap edge frequencies for sufficiently large numbers of transducers. Solid lines track two resonances of the full system, ω_S and ω_{S+1}.

3.4 Experimental structure with sparsely placed transducer pairs

This section demonstrates that the proposed feedback method can be used in practice for bandgap creation in structures with sensor and actuator configuration. The results presented here should not be seen as a validation of the approximation presented in Section 3.3. Instead, we intend to compare the bandgap crated in realistic conditions and the bandgap edge frequencies expected in an ideal metastructure. Covering the entire structure with multiple small transducer pairs, which is required for the theoretical predictions to hold, may be impractical in many cases. The use of a high number of transducer pairs leads to a need for a high number of amplifiers for actuators and sensor signal conditioning. This drives the cost of a setup up and would discourage the use of bandgap in many practical applications.

The idea that periodicity is a requirement for wave attenuation and bandgap formation was demystified in [28], with an example of a finite beam with shunted piezoelectric transducers. Here, we show a similar result in a system in the feedback configuration. What is more, we show that, in some cases, such an arrangement may produce much wider bandgaps than the commonly used periodic arrangements. For transparency, we conduct the analysis in parallel on an experimental setup and its numerical model proposed in Section 3.2. Despite the discrepancies, the model is sufficient to provide insights into system behaviour. The studied experimental setup is presented in Subsection 3.4.1. The open-loop characteristics are presented in Subsection 3.4.2. The obtained bandgaps are shown in Subsection 3.4.3.

(a) Experimental setup   **(b)** Drawing of the experimental setup with dimensions
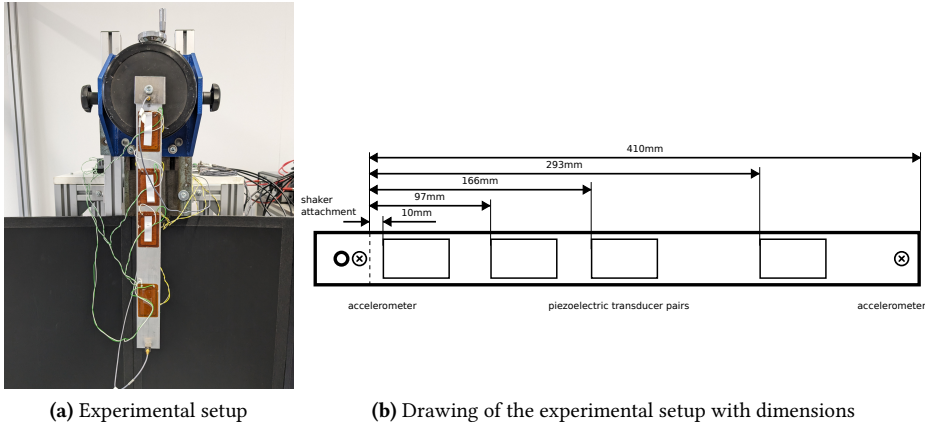
Figure 3.5: Illustration of the experimental setup. The main substrate of the structure is a slender aluminum alloy beam with thickness h_s = 2 mm and dimensions presented in 3.5b. ρ_s = 2700 kg/m^3 and c_s = 69 GPa assumed for simulations. Collocated piezoelectric patch transducers PI P-876.A15 DuraAct are used as both sensors and actuators.
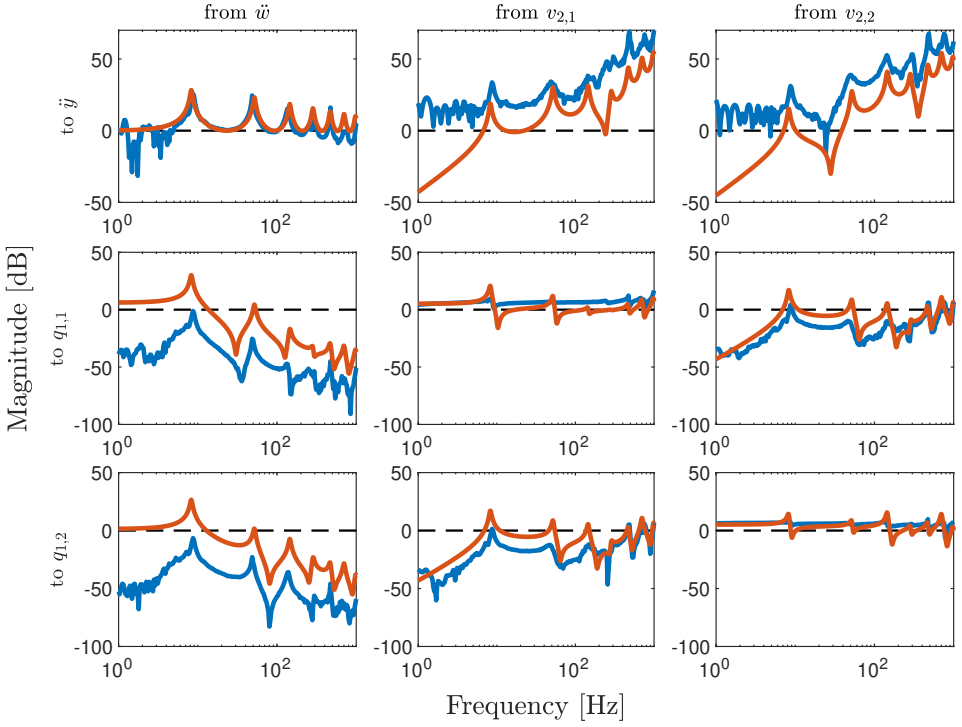
Figure 3.6: Open-loop magnitudes of the frequency response of the considered system, obtained from simulations (red) and experiments (blue). Only signals of two piezoelectric transducer pairs are presented for visibility.

3.4.1 Experimental setup

The studied structure is presented in Fig. 3.5, with the dimension of the setup in Fig. 3.5b. The main substrate of the structure is a slender aluminum alloy beam, with ρ_s = 2700 kg/m^3 and c_s = 69 GPa assumed for simulations. The base of the beam is clamped to vibration exciter Brüel & Kjær type 4809 powred with amplifier Brüel & Kjær type 2706. The vibrations of the tip and the base of the structure are measured by a pair of accelerometers Brüel & Kjær 4508 B. Their signals are used to calculate the transmissibility of the system and determine the performance. Collocated piezoelectric patch transducers PI P-876.A15 DuraAct are used as both sensors and actuators. Four pairs of piezoelectric patch transducers are used to create bandgap in the structure. In-house-made charge amplifiers, based on TL074 operational amplifiers and designed as described in [29] with C_f = 200nF and R_f = 2MΩ are used to condition the signals of the sensors. The transfer function between the charge of the sensor and the amplifier voltage output is

$$\frac{V_0}{Q} = \frac{-R_f s}{(R_f C_f s + 1)\left(R_i(C_p + C_c)s + 1\right)}. \tag{3.46}$$

The two poles of the transfer function are $\omega_1 = 1/R_f C_f$ and $\omega_2 = 1/R_i(C_c + C_p)$ and the gain of the flat frequency band is $1/C_f$. Four Dual-Channel 300V Amplifiers BD300 drive each of the actuators. The controllers are implemented digitally in the NI cRIO-9039 FPGA with the sampling frequency 10kHz and the same system is used to monitor and record the performance signals. Module NI9215 is used to measure the sensor signals from charge amplifiers, module NI9234 is used for acceleration measurements and module NI9264 is used to generate excitation signals for the shaker and piezoelectric actuators.

The numerical model of the systems is created in the modal-domain based on (3.15), (3.16), (3.17) and common dynamical system techniques. The influence of the charge amplifiers for sensors and the high-voltage amplifiers for the actuators are modelled as static gains.

3.4.2 Open-loop results

The open-loop responses of the system (in the absence of control) have been measured by sending a frequency sweep signal to each of the input channels of the system separately. The open-loop frequency responses between the base and tip accelerations and signals of two pairs of sensors and actuators are compared with the model results in Fig. 3.6. Only 3 out of 5 input-output pairs are presented for clarity. The general characteristics of the system are well captured in the model. The differences in gain in the cross-coupling terms between the transmissibility and piezoelectric channels do not have a large influence on the accuracy of performance predictions, as will be demonstrated later. The diminishing magnitude of the experimental transmissibility, more clearly visible in Fig. 3.8, is caused by the influence of the mass of the accelerometer placed at the tip of the beam. Frequency responses between the voltage and charge of the collocated sensors and actuators are presented in Fig. 3.7. Here, the differences between the experimental setup and the model are clearly visible. While the model predicts that the low-frequency gains of the frequency responses should be the same, they differ in the experimental results. This could be caused by the manufacturing tolerances of the transducers, variations in the glueing of the transducers, soldering connections and alignment of the transducers. The influence of the charge amplifiers, not captured in the model, can be clearly seen in the experimental phase plot, where at low frequencies the phase exceeds the $0°$ asymptote. The influence of the time delay can be seen in the phase lag appearing at high frequencies. Despite these parasitic effects, in the studied frequency range between 5Hz and 1000Hz, the dynamics of the systems can be considered NI.

3.4.3 Closed-loop results

In finite structures, the modal behaviour significantly influences the created bandgap. To showcase this, we consider bandgaps targeting different frequency ranges. Influencing the structure's behaviour is relatively easy close to resonance peaks since the high gain of the response of the structure leads to increased loop gain $|G_{Q_j/V_j}(s)C_j(s)|$. This case is well-researched in the active damping literature, where the objective of the controller is to reduce the magnitude of the resonance peaks of the structure. A bandgap targeting frequencies between resonance peaks may benefit structures excited by narrow-band disturbances. In such a case, the system's behaviour primarily depends on the controller's gain since the structure's response does not help with increasing the loop gain. While
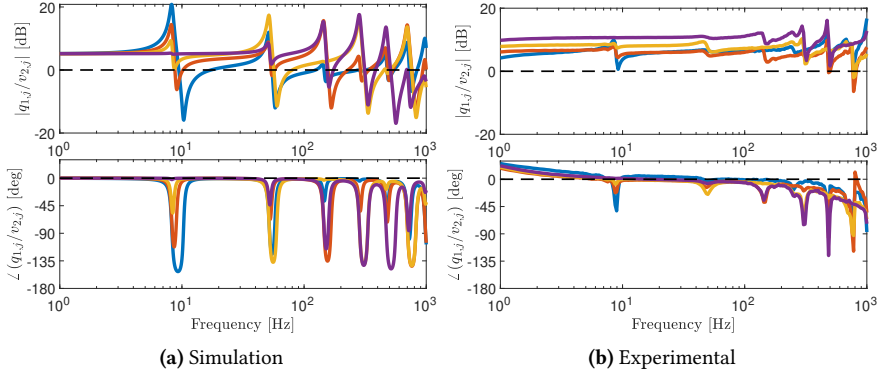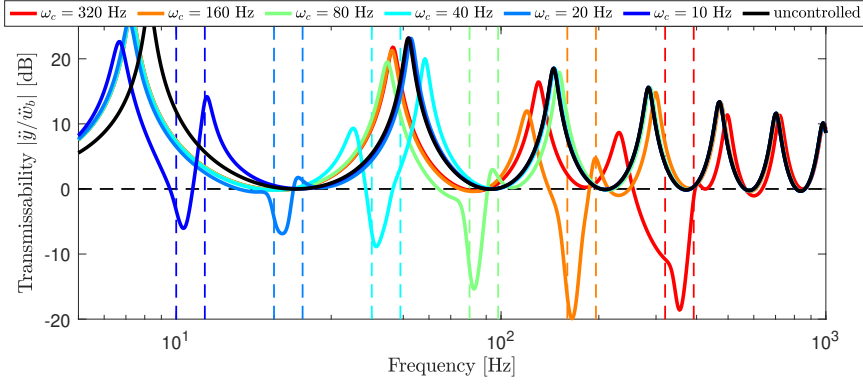
(a) Simulation

(b) Experimental

Figure 3.7: Frequency responses between the voltage and charge of the collocated sensors and actuators of the considered system. Each line corresponds to a different transducer pair.

some related results in the active vibration control literature are available [30], this topic is significantly less studied than the active damping case. Exploring this, is a contribution of this work.

Figure 3.8 demonstrates the modelled and experimentally measured closed-loop bandgaps created using feedback control. The gains of the controllers were determined individually for each of the feedback loops according to (3.26), based on the corresponding modelled or measured transfer functions. The modified PPF controllers (3.42) were used to assure that the antiresonances in the transmissibility align with the target frequency ω_c. Bandgaps in different frequency ranges were created by assigning corresponding ω_c to all the controllers. The remaining tuning parameters were fixed at values $k_c = 0.5$ and $\zeta_c = 0.05$. These values were selected since they lead to stable closed-loop dynamics for a wide range of target bandgap frequencies, and possibly better results could be achieved by tuning them individually for each transducer pair and targeted frequency range. This however, is beyond the scope of this paper and should be the subject of future work. The transmissibilities with bandgaps at different frequencies have been plotted in different colours. Vertical lines in the same colours present the expected bandgap region boundaries, based on the infinite number of transducers assumption (3.45).

In all the considered cases, it was possible to create a bandgap region in the vicinity of the target frequency. The width of the bandgap strongly depends on the targetted range of frequencies. While bandgaps are narrower than boundaries expected in the ideal conditions in the lower frequency region, significantly wider bandgaps are obtained at higher frequencies. This effect may be related to the non-periodic arrangement of transducers on the structure and the large spacing between the transducers. Especially at higher frequencies, the obtained bandgap is related to the locations and the number of transducers. This effect is worth exploring to optimise the structure's design for bandgap generation.

Although the system's overall behaviour is well captured in the model, significant depth differences can be seen between the bandgaps obtained in the model and measured in the experiment. This highlights the importance of developing design methods based

(a) Simulation
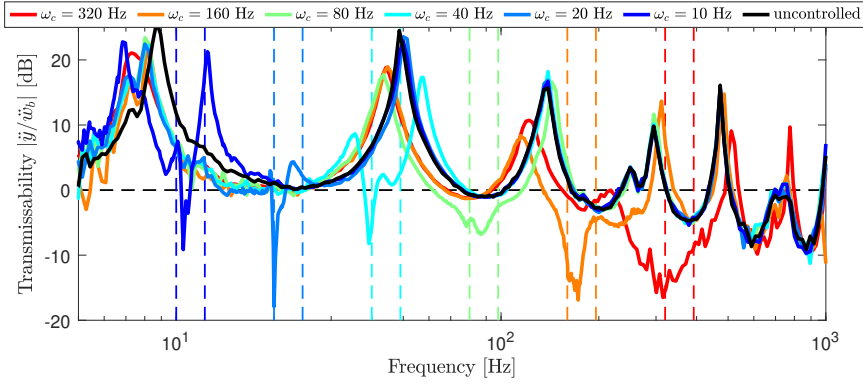
(b) Experiment

Figure 3.8: Transmissibility of the smart structures with sparsely placed transducers pairs, obtained from simulations and experiments. Different colour lines present the results with controllers tuned for different target frequencies and the same gain $k_c = 0.5$. Vertical dashed lines indicate the expected bandgap edge frequencies for a fully-covered metastructure with a sufficiently high number of transducer pairs.

on the experimentally obtained, non-parametric models of the system, like frequency responses.

The differences in the lower frequency region (see bandgaps near 10Hz and 20Hz) can be attributed to the influence of the charge amplifier dynamics. The phase lead, clearly visible in Fig. 3.7b cancels the influence of the damping of the controller ζ_c at specific frequencies, leading to stronger attenuation. Using this effect for the benefit of the designer is also worth further studies. At higher frequencies (bandgaps near 80Hz, 160Hz, 320Hz) the measured bandgaps are shallower than expected based on the model. We speculate that this is caused by the presence of noise in the system. If a deep bandgap is successfully implemented, the magnitude of the system response in the bandgap range is significantly reduced. This leads to a low signal-to-noise ratio. Moreover, in any closed-loop control system noise, originating for example from the electronics used in the system, is fed back to the actuators creating additional disturbance force.

The experimental results could be improved by reducing the noise levels in the system and using better-suited identification techniques. We expect that the noise can be eliminated to a large extent by improving the electronic implementation of the control system. Such improvements should include both low-noise power electronics for driving the actuators and more advanced circuits for sensor signal conditioning. To better identify the transmissibility of the system, attention should be paid to the selection of the excitation signal. The use of periodic signals gives access to a detailed nonparametric noise analysis and the identification could be further improved with local parametric methods (for example, see [31]).

3.5 Conclusions

Bandgaps - regions of reduced vibration transmissibility in elastic structures, are an opportunity for vibration control originating from the research on elastic metamaterials. In the case of slender structures, the use of piezoelectric patch transducers appears to be a well-suited solution. While the use of resonant shunts to create bandgaps is a well-researched topic, few results on obtaining bandgaps using feedback systems with piezoelectric sensors and actuators have been published so far.

We investigated this approach for creating bandgaps in finite beams. A simplified model of the system was developed and used for simulations. Using the assumption of an infinite number of transducers applied on the beam, we developed a method to estimate the influence of a feedback loop on a structure with piezoelectric sensors and actuators in closed form, which is valid for arbitrary feedback loop dynamics. The approximation's validity and the influence of a finite number of transducers on the bandgap generation were studied numerically. Additionally, we considered beams with a low number of sparsely placed transducer pairs and demonstrated that in such structures, bandgaps can be created using the proposed feedback approach, in some cases wider than in ideal metastructures.

The proposed approach for the design of feedback controllers for bandgap generation was validated experimentally, where clear bandgap regions at the target frequencies ranging between 10 and 320 Hz were measured. Possible improvements to these results can be achieved by modifying the electronic implementation of feedback systems to reduce noise levels and by applying more advanced identification techniques.

The presented approach can be extended to multiple PPF controllers in parallel to simultaneously create several bandgap regions. By correctly selecting the resonance frequencies and gains, merging the bandgap regions for attenuation in a wider frequency range should also be possible. The same stability condition, based on the negative imaginary systems theory, could be used.

3

References

[1] H. Soemers, *Design principles for precision mechanisms.* Enschede: University of Twente, 2010.

[2] J. A. Gripp and D. A. Rade, "Vibration and noise control using shunted piezoelectric transducers: A review," 11 2018.

[3] G. Wang and S. Chen, "Large low-frequency vibration attenuation induced by arrays of piezoelectric patches shunted with amplifier-resonator feedback circuits," *Smart Materials and Structures*, vol. 25, p. 015004, 11 2015.

[4] G. Matten, M. Collet, S. Cogan, and E. Sadoulet-Reboul, "Synthetic Impedance for Adaptive Piezoelectric Metacomposite," *Procedia Technology*, vol. 15, pp. 84–89, 1 2014.

[5] J. Nečásek, J. Václavík, and P. Marton, "Digital synthetic impedance for application in vibration damping," *Review of Scientific Instruments*, vol. 87, p. 024704, 2 2016.

[6] H. Bruneau, R. Le Letty, F. Claeyssen, F. Barillot, N. Lhermet, and P. Bouchilloux, "Semi-Passive and Semi-Active Vibration Control Using New Amplified Piezoelectric Actuators," *Smart Structures and Materials 1999: Smart Structures and Integrated Systems*, vol. 3668, no. March, pp. 814–821, 1999.

[7] J. Tang and K. W. Wang, "Active-passive hybrid piezoelectric networks for vibration control: Comparisons and improvement," *Smart Materials and Structures*, vol. 10, pp. 794–806, 8 2001.

[8] H. Yu, K. W. Wang, and J. Zhang, "Piezoelectric networking with enhanced electromechanical coupling for vibration delocalization of mistuned periodic structures-Theory and experiment," *Journal of Sound and Vibration*, vol. 295, pp. 246–265, 8 2006.

[9] K. Yi and M. Collet, "Broadening low-frequency bandgaps in locally resonant piezoelectric metamaterials by negative capacitance," *Journal of Sound and Vibration*, vol. 493, p. 115837, 2021.

[10] A. Preumont, *Vibration Control of Active Structures*, vol. 246 of *Solid Mechanics and Its Applications.* Cham: Springer International Publishing, 4 ed., 2018.

[11] K. Yi, Z. Liu, and R. Zhu, "Multi-resonant metamaterials based on self-sensing piezoelectric patches and digital circuits for broadband isolation of elastic wave transmission," *Smart Materials and Structures*, vol. 31, p. 015042, 12 2022.

[12] B. Jansen, H. Butler, and R. Di Filippo, "Active damping of dynamical structures using piezo self sensing," in *IFAC-PapersOnLine*, vol. 52, pp. 543–548, Elsevier, 1 2019.

[13] K. Yi, M. Ouisse, E. Sadoulet-Reboul, and G. Matten, "Active metamaterials with broadband controllable stiffness for tunable band gaps and non-reciprocal wave propagation," *Smart Materials and Structures*, vol. 28, p. 065025, 5 2019.

3

[14] F. Li, C. Zhang, and C. Liu, "Active tuning of vibration and wave propagation in elastic beams with periodically placed piezoelectric actuator/sensor pairs," *Journal of Sound and Vibration*, vol. 393, pp. 14–29, 4 2017.

[15] T. Ren, F. Li, Y. Chen, C. Liu, and C. Zhang, "Improvement of the band-gap characteristics of active composite laminate metamaterial plates," *Composite Structures*, 2020.

[16] Z. Y. Li, T. X. Ma, Y. Z. Wang, Y. Y. Chai, C. Zhang, and F. M. Li, "Active auto-adaptive metamaterial plates for flexural wave control," *International Journal of Solids and Structures*, vol. 254-255, p. 111865, 11 2022.

[17] A. Banerjee and K. K. Bera, "Emergence of non-reciprocity in metabeam exploiting piezoelectric sensing and actuation," *International Journal of Mechanical Sciences*, vol. 236, p. 107765, 2022.

[18] G. Wang, J. Wang, S. Chen, and J. Wen, "Vibration attenuations induced by periodic arrays of piezoelectric patches connected by enhanced resonant shunting circuits," *Smart Materials and Structures*, vol. 20, p. 125019, 11 2011.

[19] G. Wang, J. Cheng, J. Chen, and Y. He, "Multi-resonant piezoelectric shunting induced by digital controllers for subwavelength elastic wave attenuation in smart metamaterial," *Smart Materials and Structures*, vol. 26, p. 025031, 1 2017.

[20] P. Shivashankar and S. Gopalakrishnan, "Review on the use of piezoelectric materials for active vibration, noise, and flow control," 2020.

[21] J. L. Fanson and T. K. Caughey, "Positive position feedback control for large space structures," *AIAA Journal*, vol. 28, pp. 717–724, 5 1990.

[22] I. R. Petersen and A. Lanzon, "Feedback Control of Negative-Imaginary Systems," *IEEE Control Systems*, vol. 30, no. 5, pp. 54–72, 2010.

[23] C. Sugino, Y. Xia, S. Leadenham, M. Ruzzene, and A. Erturk, "A general theory for bandgap estimation in locally resonant metastructures," *Journal of Sound and Vibration*, vol. 406, pp. 104–123, 10 2017.

[24] C. Sugino, S. Leadenham, M. Ruzzene, and A. Erturk, "An investigation of electroelastic bandgap formation in locally resonant piezoelectric metastructures," *Smart Materials and Structures*, vol. 26, no. 5, 2017.

[25] C. Sugino, M. Ruzzene, and A. Erturk, "An analytical framework for locally resonant piezoelectric metamaterial plates," *International Journal of Solids and Structures*, vol. 182-183, pp. 281–294, 2020.

[26] M. B. Kaczmarek and H. HosseinNia, "Fractional-order negative position feedback for vibration attenuation," *Fractal and Fractional*, vol. 7, p. 222, 3 2023.

[27] C. Sugino, S. Leadenham, M. Ruzzene, and A. Erturk, "On the mechanism of bandgap formation in locally resonant finite elastic metamaterials," *Journal of Applied Physics*, vol. 120, p. 134501, 10 2016.

3

[28] D. Cardella, P. Celli, and S. Gonella, "Manipulating waves by distilling frequencies: A tunable shunt-enabled rainbow trap," *Smart Materials and Structures*, vol. 25, p. 085017, 7 2016.

[29] J. Karki, "Signal Conditioning Piezoelectric Sensors - Application Report - Texas Instruments," tech. rep., Texas Instruments, 2000.

[30] S. M. Kim, M. J. Brennan, and G. L. Abreu, "Narrowband feedback for narrowband control of resonant and non-resonant vibration," *Mechanical Systems and Signal Processing*, vol. 76-77, pp. 47–57, 8 2016.

[31] J. Schoukens, K. Godfrey, and M. Schoukens, "Nonparametric Data-Driven Modeling of Linear Systems: Estimating the Frequency Response and Impulse Response Function," 8 2018.

3

4

Relationship of Bandgap Formation with Unit Cell Number and Modal Behaviour

In the previous chapter, we developed a simplified model for active metastructures based on the assumption that the structure consists of infinitely many transducer pairs. This enabled relating the bandgap generation problem to loop-shaping techniques studied in Chapter 2. Here, the conditions necessary for the model to accurately describe the behaviour of the systems are studied in more detail. Specifically, we show that the necessary number of transducer pairs is related to the dominant mode in the targeted frequency range.

Active Piezoelectric Metastructures: Relationship of Bandgap Formation with Unit Cell Number and Modal Behaviour

4

Abstract *Elastic piezoelectric metastructures with actively implemented resonators offer an opportunity for novel vibration attenuation solutions, thanks to the possibility of creating bandgaps at low frequencies, their tuneability and compactness. We focus on metastructures with sensors and actuators, where the resonators are implemented using feedback control techniques, an alternative to commonly used shunt circuits. For bandgap creation in finite structures, unit-cell-based dispersion analysis is unsuitable since it lacks information on modal behaviour. As an alternative, a modal analysis approach can be used to calculate the frequency range of a locally resonant bandgap in closed form using the assumption of an infinite number of transducers of infinitesimal length distributed along the structure. The predictions obtained using this approach are accurate if a sufficiently high number of transducers is used, and the number required increases with the increasing target frequency. Despite the recent developments in the field, it remains to be seen what the sufficient number is in a specific situation. In this paper, we show that for low-frequency bandgaps in cantilevers, the minimal number of transducers is equal to the number of the dominant vibration mode at the targeted range of frequencies. Increasing the number of transducers above this value increases the vibration attenuation in the bandgap region but does not result in its widening. The result is demonstrated using numerical analysis.*

4.1 Introduction

In the context of elastic metamaterials, a bandgap denotes a specific frequency range wherein the structure effectively mitigates the propagation of vibrations. Creating the bandgaps within structures gives engineers a powerful tool for customizing dynamic responses, opening up new possibilities for vibration isolation solutions. However, this paper is not about metamaterials, as we focus on creating bandgaps in finite metastructures. In such a case, most existing modelling approaches for metamaterials focused on band structure dispersion analysis for waves propagating in an infinite media comprising a perfectly periodic lattice arrangement are unsuitable. By neglecting the effects of boundary conditions, these models are only valid for high-frequency applications and are not useful for analysing systems operating at low frequencies.

This problem has been addressed in [1, 2] for finite metastructures with mechanical resonators and in [3, 4] for electromechanical metastructures with piezoelectric transducers and resonators implemented by shunt circuits. The authors developed a theory for

finite metastructures under transverse vibrations and exact analytical results for bandgap estimation using modal analysis. Applying the assumption of an infinite number of resonators (or transducers) placed on the structure, the bandgap edge frequencies can be calculated in the closed form. In [5] (Chapter 3) this approach has been applied to piezoelectric metastructures with transducers divided into sensors and actuators, where the bandgaps are generated using feedback control and analogue results have been obtained.

The results presented in the aforementioned papers clearly show that the approximations obtained using the assumption of an infinite number of resonators are accurate if a structure is divided into a sufficient number of unit cells. However, it remains unclear what exactly the sufficient number is in a specific situation.

As the modal behaviour determines the dynamics of a finite structure, it is logical to expect the required number of transducers to be related to the vibration modes. In a flexible structure, the vibrations at a specific frequency will be predominantly determined by a single mode. This link can be used to determine optimal locations for tuned mass dampers targeting specific resonance peaks [6]. Similarly, the optimal placement for piezoelectric patch transducers for active damping applications is also determined using the knowledge of the modeshapes of the structure [7].

In this paper, we study this problem for piezoelectric metastructures in sensor/actuator configuration. Such configuration offers an attractive alternative to shunt circuits [8] commonly used for bandgap generation [3, 4, 9]. The control elements can be seen as generalized stiffness, which makes it easy to relate to passive mechanical solutions. Frequency domain tuning techniques based on experimental data can be used to design the controller. This removes the burden of meticulous modelling of minute details of the structure to capture the dynamics vital to designing the feedback loop. Moreover, adaptive systems, self-sensing and other advanced control architectures can be adopted from the active control results.

For a cantilever excited by base vibration, we show that the minimal number of transducers required for generating low-frequency bandgaps with width well approximated by the edge frequencies obtained for the ideal case is equal to the number of the mode dominant at the bandgap frequency. The analysis is based on the model derived in [10] (Chapter 3). In section 4.2, we present the analysis supporting our findings. The discussion in section 4.3 presents the findings in a wider context. The paper is concluded in section 4.4.

4.2 Minimal number of transducers

It is clear from the literature [1–5] that the bandgap edge frequency predictions obtained using the infinite number of transducer assumption like (3.40) are accurate if a sufficiently high number of transducers is used. However, it remains to be seen what the sufficient number is in a specific situation.

Vibration modes determine the dynamics of finite elastic structures. To see their influence on the bandgap formation, we consider bandgaps obtained with controller (3.25) with

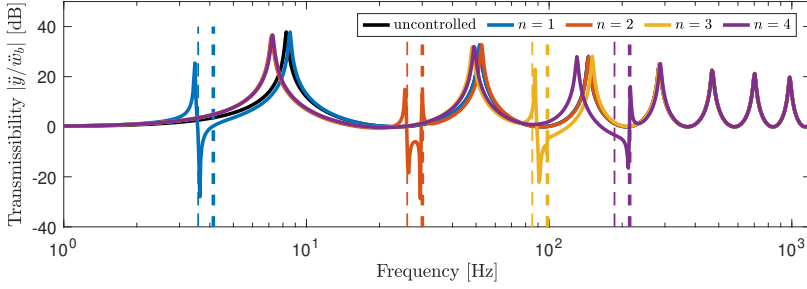$$\omega_c = \omega_{c,n} = (\omega_{n-1} + \omega_n)/2, \tag{4.1}$$

Figure 4.1: Transmissibility of a metastructure fully covered in piezoelectric material, divided into $S = 2$ sensor/actuator pairs. Different colour lines present the results with controllers tuned for different target frequencies $\omega_{c,n}$ and the same gain $k_c = 0.25$. Vertical dashed lines indicate the expected bandgap edge frequencies obtained using the assumption of an infinite number of transducers.

4

(a) Lower edge frequency ω_L

(b) Higher edge frequency ω_H
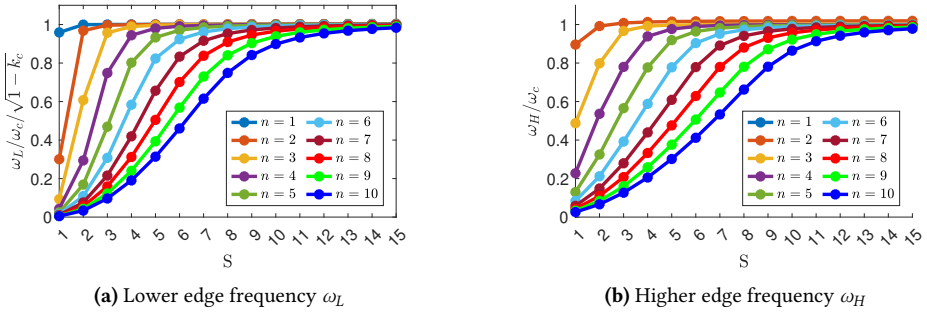
Figure 4.2: Bandgap edge frequencies as a function of the number of transducer pairs on the beam S for bandgaps targeting frequency regions dominated by subsequent vibration modes n.

where $\omega_n > \omega_{n-1}$ denote the system's resonance frequencies in ascending order. In such a configuration, the mode corresponding to ω_n dominates the structure dynamics at the bandgap range of frequencies.

Figure 4.1 shows the transmissibility of cantilever piezoelectric bimorph beam divided into $S = 2$ transducer pairs. Four cases with controllers tuned to different target frequencies $\omega_{c,n}$ are presented. The bandgap placed below the 1st resonance peak is bounded only by the resonance peaks below the targeted region. The bandgap placed between the 1st and 2nd modes is clearly visible, with the resonance peaks defining its borders close to the expected values from (3.40). The bandgaps placed at higher frequencies are significantly narrower than expected and the characteristic pattern of resonance and anti-resonances is not developed.

To better illustrate the relationship between the modal behaviour of the structure and bandgap generation, we track the bandgap edge frequencies in metastructures divided to different number transducer pairs. If the number of transducer pairs S is sufficiently high,
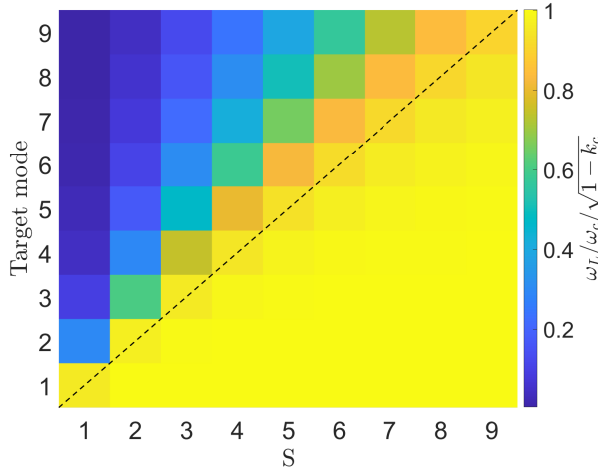
Figure 4.3: The ratio of the lower bandgap edge frequency ω_L for a metastructure with S transducer pairs and the predicted edge frequency at ideal conditions for bandgaps targeting frequency regions dominated by subsequent vibration modes n. The dashed line highlights the direct relationship between the convergence of ω_L to the ideal value and the number of transducers S equal to the number of the targeted mode.
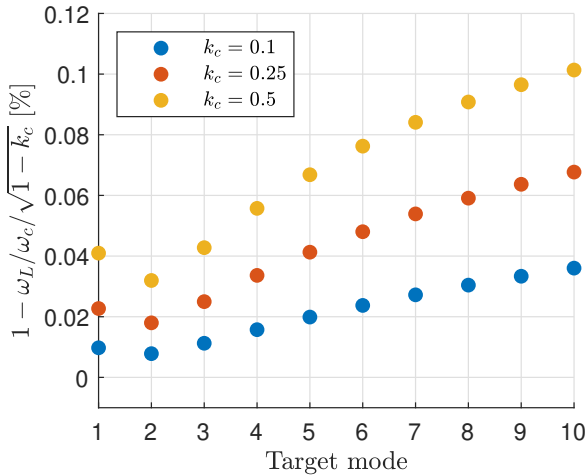
Figure 4.4: The discrepancy between the lower bandgap edge frequency ω_L and the edge frequency expected at ideal conditions for structures with the number of transducers S equal to the number of the dominant vibration modes in the targeted range of frequencies. The differences increase as higher frequency modes are targeted and higher controller gains, leading to wider bandgaps, are used.

the bandgap lower and higher edge frequencies are indicated by

$$\omega_L = \omega_S, \qquad\qquad \omega_H = \omega_{S+1},$$

respectively, where ω_S, ω_{S+1} denote consecutive resonance frequencies of the closed-loop system (with implemented resonator dynamics). Figure 4.2 tracks the edge frequencies for the bandgaps targeting the first 10 resonance modes in structures with an increasing number of transducer pairs. The edge frequencies asymptotically approach ideal values, with the rate of approach dependent on the targeted mode. Note that for the bandgap placed below the 1st resonance peak $n = 1$, only the lower edge frequency is visible, as the higher one overlaps with the resonance of the structure $\omega_H = \omega_1$ and is beyond the visible area of the plot. The edge frequencies ω_L, ω_H behave in the same way as S is increasing. For this reason, in the remainder of the paper we consider only the ω_L.

The direct relationship between the targeted mode, number of transducers and the width of the created bandgap is clearly visible in Fig. 4.3, where the ratio of the actual ω_L and the edge frequency obtained using the infinite number of transducers assumption is plotted against the number of transducers S and the targeted mode. It can be seen that bandgaps with edge frequencies close to the ideal values are obtained for all the targeted modes ω_n when the number of transducers is equal to the number of the targeted mode $S = n$.
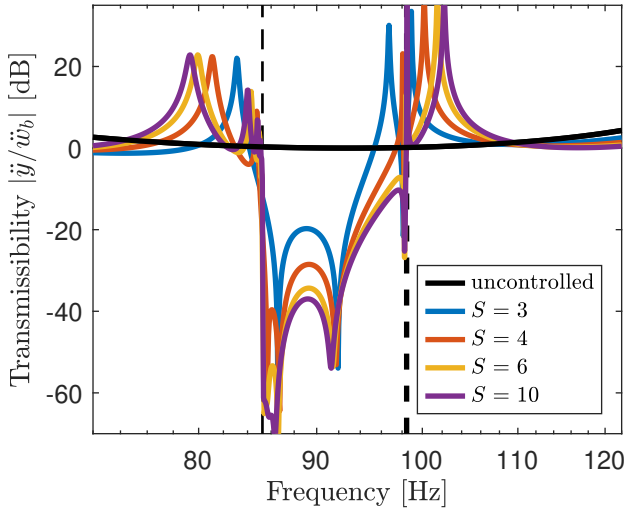
Figure 4.5: Transmissibility of a metastructure divided into different number S of sensor/actuator pairs, with all the controllers tuned to the same target frequency $\omega_{c,n}$ and gain $k_c = 0.25$. Vertical dashed lines indicate the expected bandgap edge frequencies obtained using the assumption of an infinite number of transducers.

The discrepancies between the ideal and actual edge frequencies for $S = n$ increase with the mode number and the controller gain are shown in Fig. 4.4. The error increases as higher-frequency modes are targeted and as higher controller gains are applied. Overall,

the errors in all the considered cases remain small, which indicates that for low-frequency bandgaps, the number of transducers equal to the number of the vibration mode dominant at the targeted frequency range is sufficient to create a bandgap with a width close to the ideal width obtained with the infinite number of transducers

The influence of increasing the number of sensor/actuator pairs S beyond the number of the targeted mode n is illustrated in Fig. 4.5, where the 3rd mode is targetted in structures in with different S. When $S = n$, the resonance peak corresponding to the higher edge frequency ω_H is slightly shifted with respect to the expected values, in agreement with the relationship show in Fig. 4.4. Increasing S brings the edge frequencies closer to the expected values, results in steeper drop of transmissibility magnitude in the bandgap region and deeper bandgap overall. It however does not lead to a wider bandgap.

4.3 Discussion

While the obtained results confirm the hypothesis of this paper, several questions related to generating bandgaps in finite metastructures, the required number of transducers and modal behaviour remain open. The presented results are based on an simplified analytical model of the structure. While the model has been validated experimentally in [5] (Ch. 3), the findings should be confirmed using more sophisticated numerical tools and dedicated experiments.

In this paper, we considered cantilever beams, fully covered with piezoelectric transducers in sensor/actuator configuration and with specific dynamics of the feedback controllers. While intuitively, the paper's findings should also apply to piezoelectric beams with shunts and beams with mechanical resonators, it remains to be confirmed. The study should also be repeated for beams with different boundary conditions, plates and more general thin structures. Structures fully covered with transducers or mechanical resonators are impractical in many situations. Moreover, in [5] (Ch. 3), we show that structures with sparsely placed transducers covering only a part of the structure can produce bandgaps significantly wider than expected at ideal conditions. A clear design strategy to obtain such a result would benefit the practical creation of bandgaps in structures.

4.4 Conclusion

The objective of this work was to find out what the sufficient number of unit cells in a finite metastructure is to obtain bandgaps with widths close to the predictions made with the infinite number of transducer assumption. To this end, we focused on bandgap generation in cantilever metastructures with collocated piezoelectric sensors and actuators, and positive position feedback (PPF) controllers. Using numerical studies, we showed that for low-frequency bandgaps in cantilevers, the minimal required number of transducers equals the number of the dominant vibration mode at the targeted range of frequencies. Increasing the number of transducers above this value increases the vibration attenuation in the bandgap region but does not result in its widening.

References

[1] C. Sugino, S. Leadenham, M. Ruzzene, and A. Erturk, "On the mechanism of bandgap formation in locally resonant finite elastic metamaterials," *Journal of Applied Physics*, vol. 120, p. 134501, 10 2016.

[2] C. Sugino, Y. Xia, S. Leadenham, M. Ruzzene, and A. Erturk, "A general theory for bandgap estimation in locally resonant metastructures," *Journal of Sound and Vibration*, vol. 406, pp. 104–123, 10 2017.

[3] C. Sugino, S. Leadenham, M. Ruzzene, and A. Erturk, "An investigation of electroelastic bandgap formation in locally resonant piezoelectric metastructures," *Smart Materials and Structures*, vol. 26, no. 5, 2017.

[4] C. Sugino, M. Ruzzene, and A. Erturk, "An analytical framework for locally resonant piezoelectric metamaterial plates," *International Journal of Solids and Structures*, vol. 182-183, pp. 281–294, 2020.

[5] M. B. Kaczmarek and S. H. HosseinNia, "Creating bandgaps in active piezoelectric slender beams through positive position feedback control," *Smart Materials and Structures*, vol. 33, p. 125039, 11 2024.

[6] K. Verbaan, S. van der Meulen, and M. Steinbuch, "Broadband damping of high-precision motion stages," *Mechatronics*, vol. 41, pp. 1–16, 2 2017.

[7] L. Bin, L. Yugang, Y. Xuegang, and H. Shanglian, "Maximal modal force rule for optimal placement of point piezoelectric actuators for plates," *Journal of Intelligent Material Systems and Structures*, vol. 11, pp. 512–515, 7 2000.

[8] J. A. Gripp and D. A. Rade, "Vibration and noise control using shunted piezoelectric transducers: A review," 11 2018.

[9] L. Airoldi and M. Ruzzene, "Design of tunable acoustic metamaterials through periodic arrays of resonant shunted piezos," *New Journal of Physics*, vol. 13, p. 113010, 11 2011.

[10] M. Kaczmarek and H. HosseinNia, "Tuneable Bandgap in Active Piezoelectric Metastructures Through Feedback Control," *Available at SSRN*, 2024.

5

Fractional-order control in AVC

Chapter 2 presented the loop-shaping approach for designing an AVC system. The loop gain analysis highlighted the importance of the phase margin at the cross-over frequencies. Moreover, the experimental evaluation of the vibration isolation system presented at the end of the chapter highlighted the importance of sufficient roll-off away from the targeted frequency, which is necessary to limit the transmission of disturbances to the system, which requires a steep slope of the loop shape. In LTI control, an element's magnitude slope and phase are determined by the Bode's relationship. This chapter seeks the optimal tradeoff between these conflicting requirements by introducing the fractional-order negative position feedback control. We show that using the proposed elements leads to improved performance compared to LTI counterparts.

Fractional-Order Negative Position Feedback for Vibration Attenuation

Abstract *In this paper, a fractional-order extension of a negative position feedback (NPF) controller for active damping is proposed. The design of the controller is motivated by the frequency-domain loop shaping analysis and the controller dynamics are defined to maintain the high-pass characteristics of an integer-order NPF. The proposed controller provides greater attenuation of a resonance peak of a flexible plant than the integer order equivalent with the same high-frequency gain. The stability and influence of tuning parameters on the behaviour of the proposed controller are analysed. The efficiency and feasibility of the fractional-order controller are demonstrated with an implementation on an experimental setup.*

5

5.1 Introduction

Vibration issues are becoming increasingly important when lightweight structures are used in machinery. The reduced mass of moving components reduces the power required to achieve high levels of acceleration, which benefits performance. Unfortunately, without reducing overall dimensions, this can only be accomplished by using thin structures and low-density materials. This may introduce lightly damped low-frequency resonances into the dynamics of a structure, making it more susceptible to disturbances and causing slowly decaying vibrations. The desire to solve this problem leads to increased interest in active vibration control techniques.

The fixed-structure controllers are important from the industry point of view since they are easier to implement than the optimization-based alternatives. The control structures are designed to be inherently robust and easy to tune, using general knowledge of the dynamics of a plant. This approach is often used for collocated resonant mechanical systems, that have the interlacing pattern of poles and zeros along the frequency axis. As a result, in absence of time delays or parasitic dynamics, the phase of a frequency response of a system with generalized force as input and generalized displacement as output always remains between 0° and −180° [1].

Velocity feedback (VF) is a popular strategy to increase damping in structures [2]. While the principle of VF is simple and intuitive, high gain of the controller at high frequencies may lead to amplification of noise and destabilize the system in presence of time delays and parasitic dynamics. Moreover, due to sensor dynamics, low-frequency components of velocity signals measured with commonly used sensors such as accelerometers or geophones are unreliable. In consequence, low and high-pass filters are often incorporated into the controller. Their presence influences the performance of VF and has to be included in the design process.

Dynamics of VF combined with a second-order band-pass filter tuned for a single frequency are equivalent to passive vibration absorbers [3]. Similar dynamics are used in resonant controllers. In these methods, a controller is a second-order element with resonance frequency tuned to the frequency of the mode to be damped [4–6]. The resonance peak of the controller is used to increase the gain in the vicinity of the target mode. An example is a negative position-feedback (NPF) controller, which has high-pass characteristics. The same goal is obtained in negative derivative feedback (NDF) by using a velocity signal and a controller with band-pass characteristics [7, 8]. For single mode systems, this design will prevent influence on both high and low-frequency dynamics.

Another type of a resonant controller is positive position feedback (PPF) [9], which takes a generalized displacement as an input and has low-pass characteristics. In consequence, the system is robustly stable, even in the presence of time delays, but at a price of lowering the dynamical stiffness of the system at low frequencies [5].

For all resonant controllers, damping is an important tuning parameter. In absence of damping, the use of resonant controllers leads to peak splitting, where the resonance peak of the mode is replaced by a zero accompanied by new resonance peaks at lower and higher frequencies. This phenomenon is typical for coupled resonators and has been described for tuned mass dampers already in [10]. In standard tuning procedures for resonant controllers, the peaks are removed by shifting the corner frequency of the controller with respect to the mode and increasing the damping of the controller.

In this paper, we study the behaviour of the resonant vibration control system using the frequency-domain loop shaping approach and show that the creation of new resonance peaks in the peak splitting may be prevented by using fractional-order filters. As the main contribution, we introduce a new fractional-order NPF controller. We analyse the dynamics of the control element in the active vibration control context and show that it provides stronger resonance peak attenuation than the integer-order counterparts with the same gain. The efficacy of the proposed attenuator is demonstrated experimentally.

The use of fractional order (FO) calculus has proven to be beneficial in engineering applications. Besides being used for modelling of various electrical, thermal and biomimetic systems, as well as chaos and fractals [11–14, 14, 15], they found application in modelling of viscoelastic materials [16, 17]. FO calculus also has the potential of improving the performance of controllers [18, 19]. In the majority of available literature on FO control the focus is on high-authority control [1], with FO PID as an example [20, 21].

Several examples of FO low-authority controllers can also be found in the literature. In [22] a FO Integral Resonant Controller (IRC) has been developed. A commensurate order FO PPF controller has been proposed in [23], where the additional degree of freedom has been used to increase the roll-off of the filter at high frequencies in order to reduce the spillover. In [24] an FO PPF with 3 additional tuning parameters has been proposed for vibration control of structures with parameter perturbations, however, depending on the parameters selection the controller may lose the low-pass characteristics typical for PPF. A fractional-order integral controller for collocated smart structures was proposed in [25] to improve the robustness of the closed-loop system to changes in the plant. In [26] a concept of fractional-order difference feedback for active damping have has introduced.

Most of the FO controllers mentioned above are FO generalizations of a second order filter, previously studied in [27]. While the same applies to the control element proposed

5

in this paper, the contribution lies in clearly motivating the use of FO elements in active vibration control. We focus on the filters with (pseudo)poles close to the stability margins and their use for active damping, studied in [28, 29] and extended to non-commensurate order systems in [30]. The topic is also related to the study of fractional-order mass-spring-damper systems [31–33] and electronic resonators [34, 35]. The use of alternative fractional-order generalizations, like power-law filters [36, 37],can also be justified by the analysis conducted in this work and is an interesting direction for future research.

The design of the FO controller proposed in this paper is motivated by a frequency-domain analysis. The loop-shaping objective for active vibration control in collocated systems can be described as a reduction of the amplitude of the sensitivity function [5, 38]. In [38, 39] the relationship between the open-loop frequency response function and closed-loop sensitivity functions is represented using the Sensitivity charts, similar to the Nichols charts. In [40] manual loop shaping is used for tuning a vibration controller in an industrial setting.

The remainder of this paper is organized as follows. Background information is provided in Section 2. In Section 3, we introduce the FO NPF controller and consider the influence of tuning parameters. In Section 4 we demonstrate the performance of the proposed controller with experiments. The conclusion of the paper is given in Section 5.

5.2 Background

In this section we present preliminary information for the paper. After introducing the type of plants considered in this work, we provide some basic information about fractional-order control systems. Finally, we present the objectives for active vibration control in the loop-shaping fashion.

5.2.1 System description

Figure 5.1 presents the collocated vibration control system as a single-input single-output feedback loop. The plant G can be a lightly damped lumped mass system or a flexible structure with a collocated sensor-actuator pair. The plant dynamics can be represented as a sum of the contributions of N eigenmodes of the system

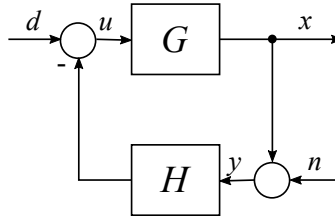$$G(s) = \sum_{i+1}^{N} \frac{\phi_{k,i}^2}{s^2/\omega_i^2 + 2\zeta_i s/\omega_i + 1},$$ (5.1)

Figure 5.1: Control structure [4].

where ω_i, ζ_i and $\phi_{k,i}$ are the eigenfrequency, damping ratio and the kth element of the eigenvector of the ith mode. In the case of flexible continuous systems, a quasi-static correction for the influence of high-frequency modes can be added to the model [1].

The controller is implemented in a negative feedback configuration and is represented by a transfer function $H(s)$, as Fig. 5.1 shows. The objective of the control system is to reduce the height of a resonance peak corresponding to a single target mode at frequency ω_n, without influencing other modes of the system.

The control system should also be robustly stable in presence of uncertainty of modal parameters. An important property of the collocated system is that the poles and zeros of $G(s)$ have an interlacing pattern [1]. In consequence, phase of $G(s)$ is always between 0° and −180°. This property may be used to guarantee the robust stability of active control systems [1, 5]. Unfortunately, it does not hold for systems with time delays, what may lead to instability if neither controller nor the plant have high-frequency roll-off characteristics or if the plant is not sufficiently damped.

5.2.2 Fractional-order control

Fractional order calculus has been developed to generalize conventional differentiation and integration to non-integer orders [41]. While there exists a vast number of definitions of FO operators, we use the Caputo derivative [42, 43] defined as

$$_C\mathscr{D}^\alpha f(t) \triangleq \frac{1}{\Gamma(m-\alpha)} \int_0^t \frac{f^{(m)}(\tau)}{(t-\tau)^{\alpha-m+1}} d\tau, \tag{5.2}$$

where $\alpha \in \mathbb{R}^+$ is the order of differentiation and m is a positive integer $m-1 < \alpha < m$.

The Laplace transform of (5.2) is given by

$$\mathscr{L}\left[_C\mathscr{D}^\alpha f(t)\right] = s^\alpha F(s) - \sum_{k=0}^{m-1} s^{\alpha-k-1} f^{(k)}(0). \tag{5.3}$$

Note, that for zero initial condition the Laplace transform of many FO operators is s^α, what greatly simplifies the design of FO controllers in the frequency domain.

A continuous-time FO system is given by a transfer function of the form

$$H(s) = \frac{b_m s^{\beta_m} + b_{m-1} s^{\beta_{m-1}} + \cdots + b_0 s^{\beta_0}}{a_n s^{\alpha_n} + b_{n-1} s^{\alpha_{n-1}} + \cdots + a_0 s^{\alpha_0}}, \tag{5.4}$$

with $a, b \in \mathbb{R}$. In a *commensurate-order* [44] system all the orders of derivation are integer multiples of the base order α, i.e. $\beta_k = k\alpha$ with $k \in \mathbb{Z}^+$, so the transfer function (5.4) is given by

$$H(s) = \frac{\sum_{k=0}^m b_k (s^\alpha)^k}{\sum_{k=0}^n a_k (s^\alpha)^k}, \tag{5.5}$$

and can be presented as a pseudo-rational function $H(\lambda)$ of the variable $\lambda = s^\alpha$

$$H(\lambda) = \frac{\sum_{k=0}^m b_k \lambda^k}{\sum_{k=0}^n a_k \lambda^k}. \tag{5.6}$$

The shape of a transfer function can be described by defining its slope in certain frequency regions. A transfer function has a slope of q in certain frequency range if its magnitude in this range is proportional to the q-th power of frequency ω^q. For example, a high-pass filter $F(s) = \frac{s}{s+\omega_f}$ has a slope of +1 at low frequencies $\omega << \omega_f$ and slope 0 at high frequency region $\omega >> \omega_f$.

Stability of a fractional-order system can be assessed by studying its transfer function [41]. In general, the denominator of (5.4) is not a polynomial and has an infinite number of roots. Among them, a finite number of roots belonging to the principle sheet of Riemann surface will determine the systems stability. The fractional order system is bounded-input bounded-output (BIBO) stable if all of the roots of the denominator that are in the principle Reimann sheet and are not the roots of the numerator have negative real parts [45]. For a commensurate-order system represented by (5.6), the stability condition is

$$|\arg(\lambda_i)| > \alpha \frac{\pi}{2}, \tag{5.7}$$

where λ_i are the roots of the characteristic polynomial in λ [41]. The stability of a closed-loop system containing a linear FO controller and a linear plant can be concluded using the frequency-domain Nyquist criteria [46].

A common way to implement FO controller is to approximate them in appropriate range of frequencies using finite-dimensional integer-order transfer functions. An overview of approximation techniques can be found in [47]. In continuous time, expansion-based and frequency-domain identification methods can be used to find the approximation. In the later category, the approximation can be found analytically, like in the method of Oustaloup [48], or identified directly from the desired frequency response using commercial software. While direct discrete-time approximation of FO-systems exist, it is also possible to discretise a continuous-time approximation, which yields satisfactory results if the sampling ratio is sufficiently high.

5.2.3 Loop-shaping for active vibration control

The objectives of the control system can be formulated in the frequency domain, by defining desired shapes of closed and open-loop transfer functions. For the system presented in Fig. 5.1, the closed-loop dynamics from the disturbance d and noise n inputs, to the performance output x and measurement y are given by

$$S = \frac{y}{n} = \frac{1}{1 + GH}, \tag{5.8a}$$

$$T_n = \frac{x}{n} = \frac{-GH}{1 + GH} = S - 1, \tag{5.8b}$$

$$T = \frac{x}{d} = \frac{G}{1 + GH} = GS. \tag{5.8c}$$

In this case, the sensitivity function S acts as the *vibration reduction ratio*. It can also be related to the degree of robustness of the system [5]. In order to minimize excitation of the system dynamics by the measurement noise n, the transfer function T_n should be possibly small at all frequencies. This means, that $S \approx 1$ is required. The objective of attenuating a
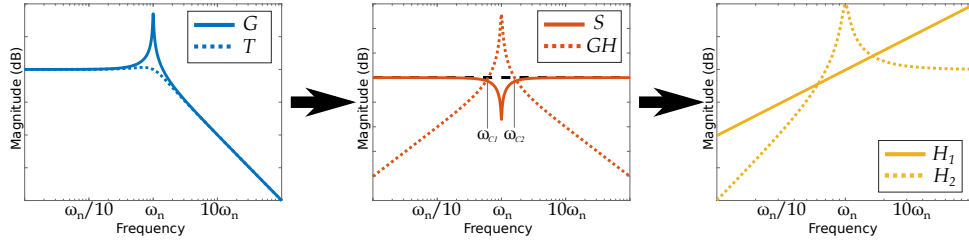
Figure 5.2: Illustration of the concept of loop-shaping. Using the knowledge of uncontrolled G and desired dynamics T, the necessary shapes of sensitivity S, loop gain GH and controllers can be deduced. H_1 denotes VF and H_2 NPF and lead to different slopes of GH.

single vibration mode without influencing other dynamics of the system can be expressed by comparing the desired closed and open-loop behaviour. At the frequency of the target mode $|T| << |G|$ is required, while $|T| \approx |G|$ should be maintained at all other frequencies. This leads to $|S| << 1$ and $|S| \approx 1$, respectively. To satisfy the conflicting requirements, the sensitivity function S should have a shape of a notch filter. In the vicinity of the resonance peak, the magnitude of S should be small to attenuate the resonance peak and at the other frequencies $|S|$ should be equal to 1. The idea of loop-shaping is illustrated in Fig. 5.2. The loop shaping for active damping can be presented as follow:

1. **Gain requirement:** The ideal loop shape of the open-loop gain GH is triangular, which can be deduced from the equation (5.8). This means that GH should have a positive slope for $\omega < \omega_n$, and a negative slope for $\omega > \omega_n$.

2. **Phase requirement:** The ideal triangular loop gain results in a region where the gain is above 1. This is required to provide high gain and reduce sensitivity at ω_n. However, it results in two crossover frequencies that can be defined as follows:

$$\omega_{c_i} =: \{\omega| \ \omega \in \mathbb{R} \ \text{and} \ |G(\omega)H(\omega)| = 1\}, i = 1, 2 \qquad (5.9)$$

To follow the ideal closed loop gain, the sensitivity at crossover frequency should be $|S| \leq 1$. To this respect, the open-loop phase at crossover frequency $\phi(\omega_{c_i}) = \angle G(\omega_{c_i})H(\omega_{c_i}) \geq -120°$.

With such a loop shape the control system will have a strong influence on the frequency regions where the magnitude of GH is high and will not change the dynamics of the system elsewhere. It should be noted that PPF cannot satisfy the above requirements. PPF was created with a focus on assuring stability for flexible systems with uncertain dynamics. In consequence, the use of PPF leads to undesired amplification of the response of the plant at low frequencies. NPF controllers presented in the last plot of Fig. 5.2 can only satisfy the gain requirement while VF control can satisfy both requirements. However, VF decreases the slope of the triangular open loop from ±2 to ±1 compared to NPF. To solve this problem this next section proposes a new element using fractional order calculus.

5.3 Fractional-order negative position feedback control

In this section we present the main contribution of the paper and introduce the FO-NPF controller. First, the definition of the dynamics of the element is motivated with the frequency-domain analysis. Subsequently, we consider stability and tuning of control systems containing the proposed controller.

5.3.1 Main Concept

To motivate the use of fractional-order resonant control, we will first more closely study the frequency-domain properties of the integer-order negative position feedback (NPF) controller [5]

$$H_2 = \frac{k_f(s/\omega_f)^2}{(s/\omega_f)^2 + 2\zeta_f(s/\omega_f) + 1},$$ (5.10)

where ω_f and ζ_f denote the corner frequency and damping ratio of the filter, with a single degree of freedom plant

$$G_T = \frac{1/k}{(s/\omega_n)^2 + 2\zeta s/\omega_n + 1}.$$ (5.11)

The integer controller satisfies the first requirement with a triangular loop gain $G_T H_2$ of ±2 slopes, which is beneficial since it limits both the low and high-frequency spillover. The shape of the controller can be seen in Fig. 5.2. Unfortunately, the steep slopes also have an adverse effect on the vibration attenuation performance of the system. Since the considered systems are linear, the Bode's magnitude-phase relationship holds [46], and the phase of the system with ±2 slopes is equal to ±180°, which is a violation of the second requirement. At regions where the loop gain $G_T H_2$ has the phase of ±180° the response of the system is amplified, which can be seen from the sensitivity transfer S in equation (5.8b). This limits the vibration attenuation performance of the system and leads to the creation of new peaks in the frequency response if the magnitude of the loop gain at these frequencies is close to 1. This behaviour can also be seen in other resonant controllers or tuned mass dampers [10].

The phase of the loop gain in the vicinity of the resonance peak is influenced by the damping ratio ζ_f of the controller. Increasing ζ_f increases the phase margin of the system, which leads to smaller secondary resonance peaks in closed loop. It also leads to a lower gain of the open loop $G_T H_2$ at the frequency of the target mode and its smaller attenuation. With an integer-order controller (5.10) the secondary resonance peaks are always attenuated by the cost of reducing the attenuation of the target mode.

In order to relax this trade-off, we propose a fractional-order resonant controller

$$H_\alpha = \frac{k_f(s/\omega_f)^{2\alpha}}{(s/\omega_f)^{2\alpha} + 2\zeta_f(s/\omega_f)^\alpha + 1},$$ (5.12)

where k_f denotes gain, ω_f the corner frequency and ζ_f the damping ratio. The element (5.12) is a fractional-order generalization of a second-order high-pass filter [27]. The slope of $G_T H_\alpha$ at lower frequencies is determined by the fractional order $\alpha \in (0, 1)$ of the controller and is equal to $+2\alpha$. Decreasing the steepness of the magnitude response at low

frequencies prevents the phase in this region from approaching +180˚. At the same time, the high resonance peak of the controller can be maintained to increase the magnitude at the target frequency. At high frequencies, the slope is determined by the plant dynamics and in the considered case is equal to −2. While the second requirement for loop-shaping is satisfied only for the lower zero-crossing frequency, it is sufficient to obtain a more desirable sensitivity S than in the integer-order case.

Tuning of the fractional-order attenuator (5.12) requires finding four parameters: fractional order α, the gain of the controller k_f, the corner frequency of the controller ω_f and its damping ratio ζ_f. Below, we present the stability conditions for the fractional-order attenuator and analyse the influence of the tuning parameters on the shape of open and closed-loop transfer functions.

5.3.2 Stability of the fractional-order attenuator

The stability of second-order fractional systems has been studied in [28, 29]. Here, we present only the specific results relevant to this paper. The fractional-order attenuator (5.12) is a commensurate-order system, so it can be represented by a pseudo-rational function $H_\alpha(\lambda)$, with $\lambda = s^\alpha$,

$$H_\alpha(\lambda) = \frac{k_f/\omega_f^{2\alpha}\,\lambda^2}{1/\omega_f^{2\alpha}\,\lambda^2 + 2\zeta_f/\omega_f^\alpha\,\lambda + 1}. \tag{5.13}$$

The roots of (5.13) are given by

$$\lambda_{1,2} = -\zeta_f\omega_f^\alpha \pm j\omega_f^\alpha\sqrt{1 - \zeta_f^2}. \tag{5.14}$$

The stability condition (5.7) states, that the roots of a stable fractional-order transfer function must lie outside of a closed angular sector. For $\alpha = 1$ this condition is equivalent to the roots remaining in the left half complex plain and can only be satisfied with positive damping coefficients. For $\alpha \in (0,1)$, the stability region is larger, and the condition can also be satisfied by a fractional-order attenuator with $\zeta_f < 0$. This leads to greater design freedom and allows for maintaining a high resonance peak for transfer functions with orders smaller than 2. In consequence, stronger attenuation of the resonance in the plant can be achieved with a FO controller, which will be further elaborated on in the following sections.

5.3.3 Influence of the tuning parameters on the attenuator

The definition of the FO attenuator in (5.12) has been chosen such that the influence of the tuning parameters is similar to the integer-order case. This is contrary to the example presented in [24], where the conversion of a filter to a FO version significantly alters its character.

The influence of the gain of the attenuator k_f and its corner frequency ω_f are the same as in the integer-order case. Their change leads to modification of the magnitude and shift of the controller along the frequency axis respectively. The fractional order α defines the slope of the controller in the low-frequency region. Additionally, it also influences the behaviour of the damping parameter ζ_f.

The response of the attenuator (5.12) at frequencies close to ω_f is characterized by a resonance peak, similar to the integer-order case. The resonance peak can be measured by a quality factor Q, determined by the maximum value of the peak, relative to the crossing point of the low and high-frequency asymptotes in the frequency response plot [49]. By evaluating (5.12) with the assumption that the fractional-order attenuator has the peak of response at $\omega = \omega_f$ we obtain

$$Q = \left((2\zeta_f \sin(\frac{\pi}{2}\alpha) + \sin(\pi\alpha))^2 + (2\zeta_f \cos(\frac{\pi}{2}\alpha) + \cos(\pi\alpha) + 1)^2 \right)^{-\frac{1}{2}}, \qquad (5.15)$$

which reduces to $Q = \frac{1}{2\zeta_f}$ for $\alpha = 1$.

The equivalent damping for an attenuator with fractional order α, that leads to the same Q-factor as for the integer order attenuator with $\zeta_{f,\alpha=1}$ is given by

$$\zeta_{f,\alpha} = \zeta_{f,\alpha=1} - \cos\left(\frac{\pi}{2}\alpha\right), \qquad (5.16)$$

which is obtained by comparing the quality factor in (5.15) with its integer-order equivalent and finding ζ_f such that both are equal.

Figure 5.3 illustrates the influence of changing the fractional order of the attenuator. In Fig. 5.3a, ζ_f is kept constant. In consequence, the height of the resonance peak decreases with decreasing order α. In Fig. 5.3b, the values of ζ_f are selected according to (5.16) such that roots of (5.13) lie on the border of the stability region, i.e. satisfy $|\arg(\lambda_i)| = \alpha\frac{\pi}{2}$. Similar to a marginally stable integer-order mass-spring system without damping, the marginally stable FO resonator has an infinite resonance peak. When ζ_f is adjusted such that a high resonance peak is maintained for all α, the phase in the vicinity of ω_f may exceed the low and high-frequency asymptotes. This may destabilize a closed-loop system, so the stability should be checked in the design process.

Note, that all the above considerations, even in the integer case, are valid only for lightly damped systems. For attenuators with significant damping, the point with the maximal magnitude of the frequency response is shifted from the corner frequency ω_f.

5.3.4 Influence of α on open and closed-loop response

Following the convention used for the integer-order attenuators [10], we consider first the behaviour of marginally-stable systems. The influence of increasing damping in the system is presented in the second step.

The phase of the loop gain $G_T H_\alpha$ with the fractional-order controllers does not approach $\pm 180°$ and as a consequence, smaller new peaks are created, which was already highlighted as a motivation to use FO controllers. This is especially visible in Fig. 5.4a, where the sensitivity function S is presented. When the resonance frequencies of the attenuator and the mode to be dampened are the same $\omega_f = \omega_n$, two uneven peaks are created in the closed-loop system (see Fig. 5.4b). Similar behaviour can be seen in tuned mass damper [10] and equal peaks can be obtained by adjusting the ω_f.

For low values of attenuator damping, the decrease of the factional order α leads to improved resonance peak attenuation, similar to the marginally stable case presented in
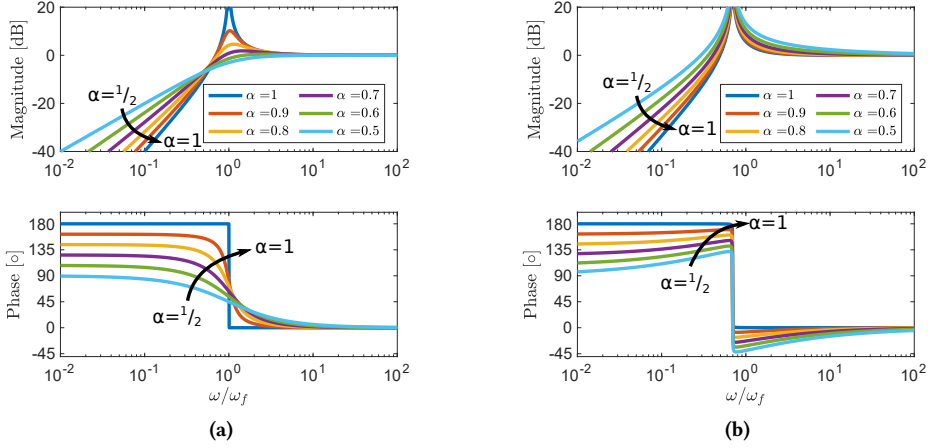
Figure 5.3: Frequency responses of a fractional-order attenuator with $\zeta_f = 0$ (a) and marginally stable fractional-order attenuators (b) for different values of α. All other parameters are constant.
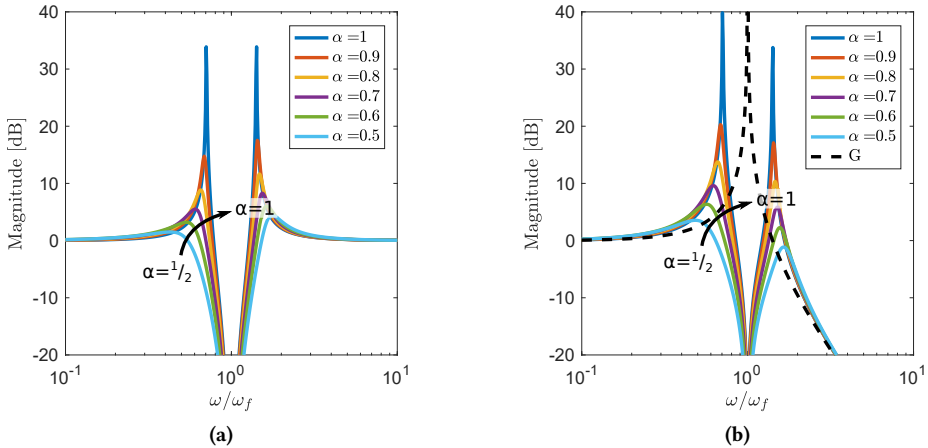

Figure 5.4: Sensitivity function S (a) and closed-loop frequency response T (b) for a lightly damped plant and marginally stable fractional-order attenuators with different α. All other parameters are constant, $\omega_f = \omega_n$.
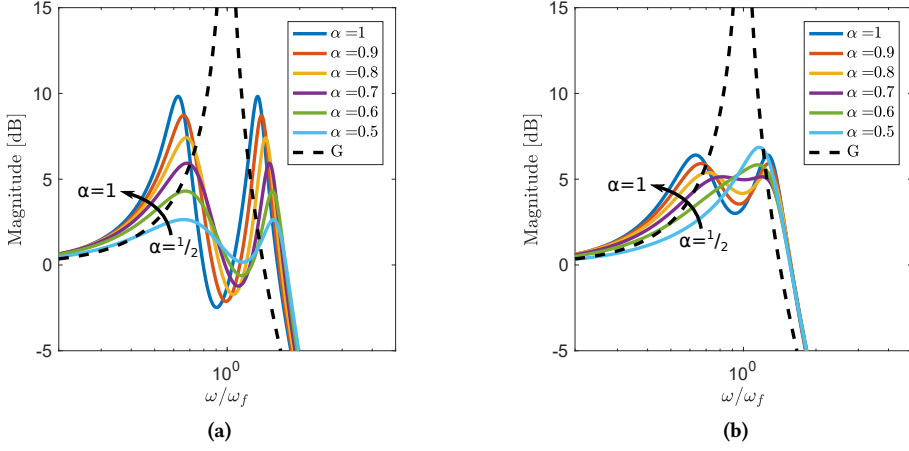
Figure 5.5: Closed-loop frequency response T for a lightly damped plant and fractional-order attenuators with (a) $\zeta_{f,\alpha=1} = 0.2$, (b) $\zeta_{f,\alpha=1} = 0.4$ and different α. Values of ω_f are adjusted for maximal attenuation.

Fig. 5.4. This is demonstrated in Fig. 5.5, where the closed-loop dynamics of the system with the fractional-order attenuators with different damping are compared. For all values of α, equivalent damping has been calculated using (5.16), so the responses can be compared. The gain of all controllers is kept constant and the values of ω_f are selected such that the value of the closed-loop H_∞ norm is minimized.

When damping is increased, the effectiveness of the attenuator no longer increases monotonically with the decrease of α, but an optimal value for which a nearly flat response in the vicinity of the resonance frequency of the plant is obtained can be found. In this case the best attenuation of a resonance peak is obtained for certain values of k_f, ω_f and $\zeta_{f,\alpha=1}$, which is illustrated in Fig. 5.5b for $\zeta_{f,\alpha=1} = 0.7$.

In general, the optimal attenuation is achieved when $\omega_f \neq \omega_n$. The shift of the corner frequencies depends on α and damping parameters ζ_n, ζ_f. If all other parameters are kept constant, the optimal ω_f increases with decreasing α, which is illustrated in Fig. 5.6.

5.3.5 Heuristic tuning guidelines

To summarize the considerations on the FO NPF controller introduced in this paper, we provide heuristic tuning guidelines, that may be helpful in obtaining an initial design of the controller. A common method of determining tuning parameters for resonant controllers is the fixed-point theory [10]. In this method, the gain of the controller (or the mass ratio in the case of a tuned-mass damper) is fixed as the main design parameter. In the integer-order case with an undamped single-mode plant, the presence of fixed points in the frequency response independent of the damping of the controller can be used to determine the remaining tuning parameters. However, even in the integer case, the parameters have to be adjusted to account for the presence of damping and other modes in the system.
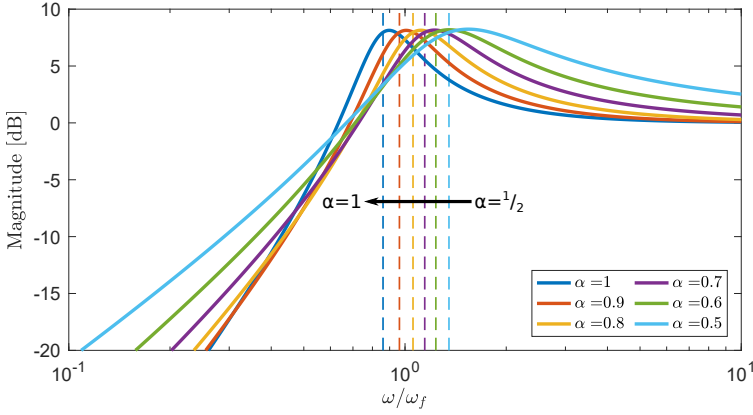
Figure 5.6: Frequency responses of optimal fractional-order attenuators with $\zeta_{f,\alpha=1} = 0.2$. Dashed lines indicate the corner frequencies ω_f of attenuators with corresponding α.

5

(a) Quality factor

(b) Corner frequency ω_f/ω_n

(c) Equivalent damping $\zeta_{f,\alpha=1}$
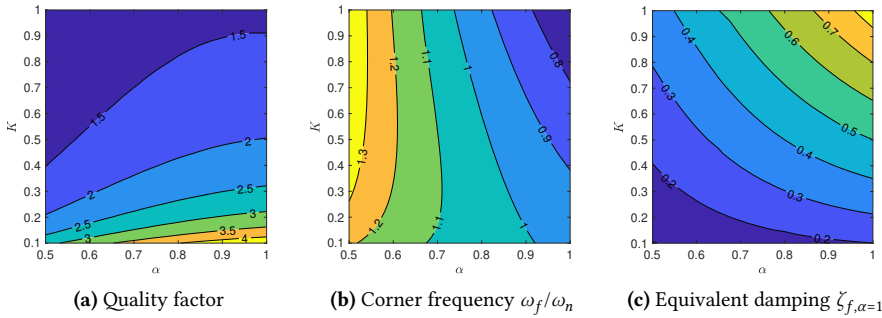
Figure 5.7: Optimal quality factor and tuning parameters for a single-mode plant with FO NPF controller.

For systems with non-integer-order controllers, such fixed-points cannot be found. Moreover, the presence of FO derivatives significantly complicates analytical derivations. The tuning guidelines presented here are based on an optimisation study, in which the H_∞ norm of a closed-loop response of a plant (5.11) with FO NPF (5.12) with different gains k_f and orders α was minimised, while the closed-loop stability was used as a constraint. The results of the study are presented in Fig. 5.7. For fixed k_f the height of the resonance peak is decreasing monotonically as the α is lowered. The changes in optimal values of the corner frequency and damping ratio are also monotonic, which greatly simplifies the tuning procedure.

In a design process, integer-order NPF with parameters selected as described in Appendix 5.A can be used as an initial design. The maximal gain of the controller k_f that satisfies the requirements in terms of high-frequency spillover should be selected. Subse-

quently, the order α can be lowered as long as the requirements in terms of low-frequency spillover are met, which leads to a stronger attenuation of the resonance peak. The corner frequency and damping ratio should be adjusted to obtain a flat magnitude of the frequency response in the vicinity of the targeted resonance frequency of the plant.

5.4 Experimental validation

In this section, we demonstrate that fractional-order attenuators can be implemented in practice and that they provide stronger attenuation than comparable integer-order filters. To focus on controller validation, a simple plant is selected. A precision flexure-based positioning stage presented in Fig. 5.8 is used as an experimental setup. This is a planar positioning system, in which two translations and one rotation of the platform (MC) can be controlled. It is achieved by controlling translations of three intermediate elements (M1-M3). Each of the intermediate elements is constrained to allow single translation by parallel flexures, actuated by a dedicated voice-coil actuator (A1-A3) and its position is measured with an optical encoder.

For the purpose of this experiment, only actuator 1A is used to control the position of intermediate element M1. The same actuator is used to provide both the disturbance signal and the control force. This results in a SISO system, whose dynamics can are approximated by a transfer function

$$G(s) = \frac{7597}{s^2 + 5.914s + 7138}. \tag{5.17}$$

This is equivalent to a mass-spring damper system with ω_n = 84.49 rad/s = 13.45 Hz, ζ_f = 3.5×10^{-2} and k = 0.9395. The attenuators are implemented as digital controllers with a sampling time of 0.1ms. This leads to a time delay of approximately 0.2 ms in the identified plant. The approximated and measured frequency responses of the plant are compared in Fig. 5.9b. In the measured dynamics, two closely placed resonance peaks can be seen, that have been approximated by a single mode in the model. Despite this discrepancy, the controllers designed using the approximated model yield good results when implemented in the actual setup.

To show the benefits of the proposed FO controller, the performance of two FO controllers with different values of α and an integer-order NPF controller were compared experimentally. To guarantee fair comparison for each selected value of α the gain of all controllers was set to k_f = 0.1 and the remaining controller parameters were chosen with the same optimization method. The objective of the optimization problem was set to minimize the H_∞ norm of the closed-loop frequency response of the system with ap-

Table 5.1: Tuning parameters of implemented fractional-order controllers

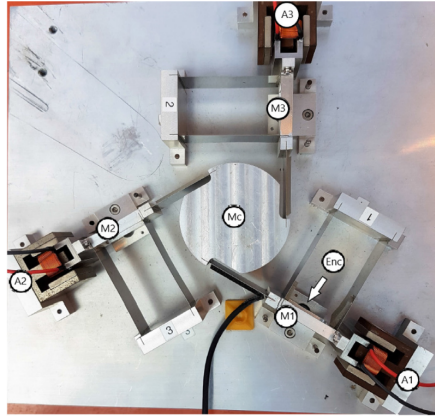|	H_1	H_2	H_3
k_f	0.1	0.1	0.1
α	1	0.7	0.5
ζ_f	0.2116	−0.2974	−0.6016
ω_n/ω_f	0.9565	1.0690	1.1954

Figure 5.8: Planar precision positioning stage with voice coil actuators denoted as A1, A2 and A3 controlling the three masses (indicated as M1, M2 and M3) and constrained by leaf flexures. The central mass (indicated by Mc) is connected to these 3 masses through leaf flexures and linear encoders (indicated by Enc) placed under masses M1, M2 and M3 provide position feedback.

5

proximated plant (5.17), with the constraint that the closed-loop system must be stable. The obtained parameters are presented in Table 5.1 and frequency responses of the controllers are shown in Fig. 5.9a. The controllers with orders $\alpha < 1$ are characterized by higher resonance peaks, which contributes to the stronger attenuation of the resonance in the closed loop. The width of the resonance peaks of the optimally tuned FO controllers increases with decreasing α, which may indicate higher robustness of the control system to parameter variation and should be studied in the future.

To enable the implementation, the FO controllers were approximated with integer-order systems. Continuous-time state-space systems of order 8 appeared to be sufficient to achieve a satisfactory approximation of the FO controller in frequencies between 1 and 5000 Hz. The approximations were obtained with the identification-based approach using the desired frequency responses of the FO controllers and Matlab function ssest. All the controllers were discretized using the bilinear (Tustin) method with a sampling time of 0.1ms and implemented on a real-time FPGA target.

The predicted and measured closed-loop dynamics of the system are shown in Fig. 5.9b. As expected, stronger attenuation of the resonance peak can be achieved with the fractional order controllers. The maximal magnitudes of the measured frequency response for systems with $\alpha = \{1, 0.7, 0.5\}$ are 13.81dB, 12.11dB and 10.36dB respectively. The differences between the predicted and measured responses are a result of using a simplified model for the plant dynamics.
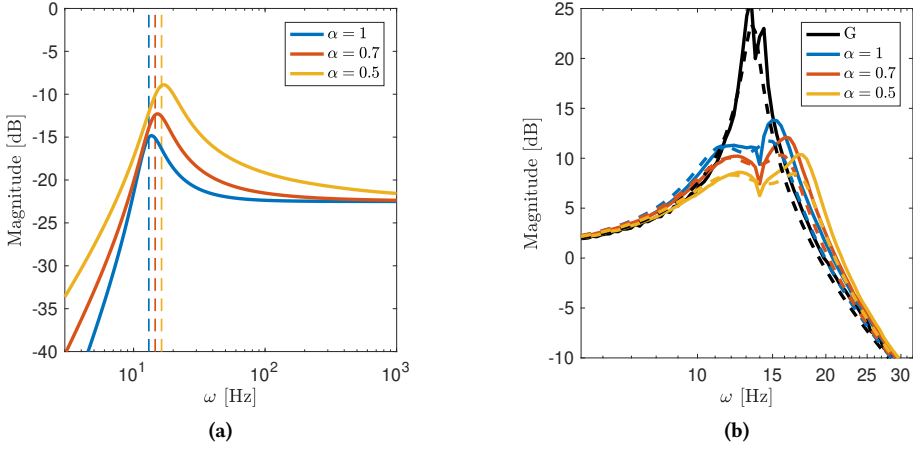
Figure 5.9: Implemented controllers (a) and compassion of frequency responses (b) obtained from experiments. Dashed (–) and solid (-) lines in (b) present the predicted and measured responses, respectively.

5.5 Conclusion

In this paper, we introduced a new FO NPF controller for collocated control systems. The design of the controller was motivated by the frequency-domain loop shaping analysis and the controller dynamics have been defined to maintain the high-pass characteristics of an integer-order NPF. The stability and tuning of the proposed controller were analysed, and we demonstrated that the extension of the NPF provides greater design freedom. Especially, lowering the steepness of the magnitude of the frequency response of the controller at low frequencies leads to stronger attenuation of the resonance peak of the plant in the closed loop. The ideal FO controllers were approximated by finite-dimensional integer-order systems, discretised and implemented for damping in an experimental setup. Despite the discrepancy between the assumed dynamics of the plant used for tuning and actual dynamics, the FO controllers provided stronger attenuation than the optimal integer-order one, while having the same high-frequency gain.

5.A Appendix: Optimal tuning of integer-order NPF

In this appendix, we briefly present derivations of tuning formulas for controllers with $\alpha = 1$. An alternative derivation, including also robustness considerations is presented in [5]. The procedure used for the derivation is based on the fixed-point method, introduced by Den Hartog for tuning of tuned mass dampers [10].

In the derivations, we consider a single mode plant (5.11) and the controller (5.10). We assume that the damping in the mechanical system has negligible influence on the tuning parameters and can be ignored in the derivations. To make the formulas more general, relative parameters are introduced. We have then:

$$G_T(\omega) = \frac{1/k}{(j\omega/\Omega)^2 + 1} = \frac{1/k}{-g^2 + 1} \tag{5.18}$$

$$
\begin{aligned}
H_2(\omega) &= \frac{k_f(j\omega/\omega_f)^{2\alpha}}{(j\omega/\omega_f)^{2\alpha} + 2\zeta_f(j\omega/\omega_f)^\alpha + 1} \\
&= \frac{k_f(jg/f)^{2\alpha}}{(jg/f)^{2\alpha} + 2\zeta_f(jg/f)^\alpha + 1}
\end{aligned} \tag{5.19}
$$

with the relative frequency $g = \omega/\omega_n$ and corner frequency shift $f = \omega_f/\omega_n$. The open-loop gain $K = k_f/k$ is also used in further derivations.

The closed-loop response of a single-mode system is presented in Fig. 5.10. Points independent of the damping ratio ζ_f, visible in 5.10c, are used to derive the tuning formulas. First, we find the frequencies $g^*_{\alpha=1}$ of the fixed points. Next, we select $f^*_{\alpha=1}$ such that the magnitudes of the fixed points are the same. Finally, $\zeta^*_{f,\alpha=1}$ is chosen to obtain a flat response.

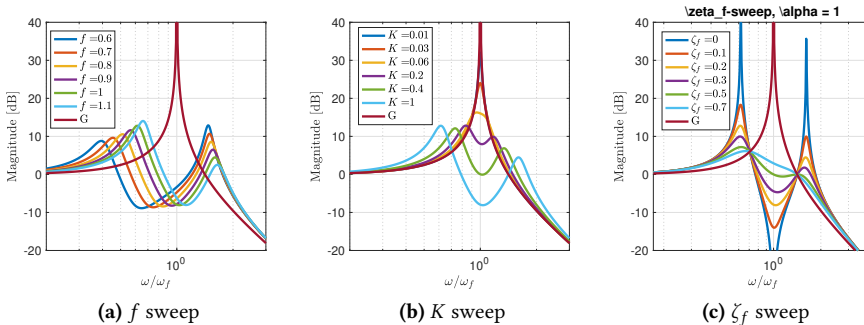(a) f sweep (b) K sweep (c) ζ_f sweep

Figure 5.10: Influence of the tuning parameters on the closed-loop frequency response of a single mode system with FracNPF with $\alpha = 1$.

The closed-loop frequency response of the system with $\alpha =$ is given by

$$
\begin{aligned}
T_{\alpha=1} &= \frac{G}{1+GH_2} \\
&= \frac{1/k(1+2\zeta_f g j/f - g^2/f^2)}{g^4/f^2 - (f^2+K+1)g^2/f^2 + 2\zeta_f(-g^3/f + g/f)j + 1},
\end{aligned}
\tag{5.20}
$$

and the magnitude of the response is

$$
|T_{\alpha=1}|^2 = \frac{1/k^2(f^4 + 4f^2 g^2 \zeta_f^2 - 2f^2 g^2 + g^4)}{(Kg^2 - f^2 + g^2 - g^4 + f^2 g^2)^2 + 4\zeta_f^2 f^2(-g^3 + g)^2}.
\tag{5.21}
$$

To find the frequency at which the magnitude of the response is independent of ζ_f, the numerator and denominator of $|T_{\alpha=1}|^2$ are expressed as polynomials in ζ i.e.

$$
|T_{\alpha=1}|^2 = (n_1 \zeta_f^2 + n_2)/(d_1 \zeta_f^2 + d_2),\, n_1, n_2, d_1, d_2 \in \mathbb{R}.
$$

The magnitude of the response is independent of ζ_f at frequencies g where the ratios of corresponding terms of the polynomials are equal i.e. $n_1/d_1 = n_2/d_2$. This is the case for

$$
g^*_{\alpha=1} = \frac{1}{2}\left(K + 2f^2 + 2 \pm ((2f^2 - 4f + K + 2)(2f^2 + 4f + K + 2))^{1/2}\right)^{1/2}.
\tag{5.22}
$$

The magnitude at the fixed points is independent of ζ_f. To find this magnitude, we can select the most convenient ζ_f. By taking $\zeta_f = \infty$ we obtain

$$
|T^*_{\alpha=1}|^2 = \left(\frac{1/k}{1-g^*_{\alpha=1}{}^2}\right)^2.
\tag{5.23}
$$

By substituting $g^*_{\alpha=1}$ and requiring the magnitudes of the closed-loop response at both fixed points to be equal, we obtain

$$
f^*_{\alpha=1} = \sqrt{2}/2\sqrt{2-K}.
\tag{5.24}
$$

The optimal value of damping should provide a flat magnitude of the closed-loop response near the frequency of the target mode. This goal can be achieved by requiring that the magnitude of the response at the fixed points $g^*_{\alpha=1}$ and at the target frequency $g = 1$ are identical. This is the case for damping ratio

$$
\zeta^*_{f,\alpha=1} = \frac{\sqrt{2}}{4}\sqrt{\frac{K(8-K)}{2-K}}.
\tag{5.25}
$$

The quality factor of the system with $\alpha = 1$ can be estimated using the magnitude of the response at the fixed points as

$$
Q^*_{\alpha=1} \approx k|T^*_{\alpha=1}| = \sqrt{2/K}.
\tag{5.26}
$$

References

[1] A. Preumont, *Vibration Control of Active Structures*, vol. 246 of *Solid Mechanics and Its Applications*. Cham: Springer International Publishing, 4 ed., 2018.

[2] M. J. Balas, "Direct Velocity Feedback Control of Large Space Structures," *Journal of Guidance and Control*, vol. 2, pp. 252–253, 5 1979.

[3] S. M. Kim, S. Wang, and M. J. Brennan, "Optimal and robust modal control of a flexible structure using an active dynamic vibration absorber," *Smart Materials and Structures*, vol. 20, p. 045003, 3 2011.

[4] S. M. Kim, S. Wang, and M. J. Brennan, "Dynamic analysis and optimal design of a passive and an active piezo-electrical dynamic vibration absorber," *Journal of Sound and Vibration*, vol. 330, pp. 603–614, 2 2011.

[5] S. M. Kim, S. Wang, and M. J. Brennan, "Comparison of negative and positive position feedback control of a flexible structure," *Smart Materials and Structures*, vol. 20, 1 2011.

[6] S. M. Kim, M. J. Brennan, and G. L. Abreu, "Narrowband feedback for narrowband control of resonant and non-resonant vibration," *Mechanical Systems and Signal Processing*, vol. 76-77, pp. 47–57, 8 2016.

[7] G. Cazzulani, F. Resta, F. Ripamonti, and R. Zanzi, "Negative derivative feedback for vibration control of flexible structures," *Smart Materials and Structures*, vol. 21, p. 075024, 7 2012.

[8] H. H. Syed, "Comparative study between positive position feedback and negative derivative feedback for vibration control of a flexible arm featuring piezoelectric actuator," *International Journal of Advanced Robotic Systems*, pp. 1–9, 7 2017.

[9] C. J. Goh and T. K. Caughey, "On the stability problem caused by finite actuator dynamics in the collocated control of large space structures," *International Journal of Control*, vol. 41, no. 3, pp. 787–802, 1985.

[10] J. P. Den Hartog, *Mechanical Vibrations*. New York: McGraw-Hill Book Company, Inc., 1940.

[11] R. Caponetto, G. Dongola, L. Fortuna, and I. Petráš, *Fractional Order Systems: Modeling and Control Applications*. World Scientific Publishing Co., 1 2010.

[12] M. E. Meral and D. Çelík, "A comprehensive survey on control strategies of distributed generation power systems under normal and abnormal conditions," 1 2019.

[13] P. P. Singh and B. K. Roy, "Comparative performances of synchronisation between different classes of chaotic systems using three control techniques," *Annual Reviews in Control*, vol. 45, pp. 152–165, 1 2018.

[14] K. Cao, Y. Chen, and D. Stuart, "A fractional micro-macro model for crowds of pedestrians based on fractional mean field games," *IEEE/CAA Journal of Automatica Sinica*, vol. 3, pp. 261–270, 7 2016.

5

[15] F. Ge, Y. Chen, and C. Kou, "Cyber-physical systems as general distributed parameter systems: Three types of fractional order models and emerging research opportunities," *IEEE/CAA Journal of Automatica Sinica*, vol. 2, pp. 353–357, 10 2015.

[16] K. Adolfsson, M. Enelund, and P. Olsson, "On the fractional order model of viscoelasticity," *Mechanics of Time-Dependent Materials*, vol. 9, pp. 15–34, 1 2005.

[17] A. Bonfanti, J. L. Kaplan, G. Charras, and A. Kabla, "Fractional viscoelastic models for power-law materials," *Soft Matter*, vol. 16, pp. 6002–6020, 7 2020.

[18] Y. Q. Chen, "Ubiquitous fractional order controls?," in *IFAC Proceedings Volumes (IFAC-PapersOnline)*, vol. 2, pp. 481–492, Elsevier, 1 2006.

[19] Y. Q. Chen, I. Petráš, and D. Xue, "Fractional order control - A tutorial," in *Proceedings of the American Control Conference*, pp. 1397–1411, 2009.

[20] A. A. Dastjerdi, N. Saikumar, and S. H. HosseinNia, "Tuning guidelines for fractional order PID controllers: Rules of thumb," *Mechatronics*, vol. 56, pp. 26–36, 12 2018.

[21] A. A. Dastjerdi, B. M. Vinagre, Y. Q. Chen, and S. H. HosseinNia, "Linear fractional order controllers; A survey in the frequency domain," 1 2019.

[22] A. San-Millan, V. Feliu-Batlle, and S. S. Aphale, "Application of a fractional order integral resonant control to increase the achievable bandwidth of a nanopositioner.," *IFAC-PapersOnLine*, vol. 50, no. 1, pp. 14539–14544, 2017.

[23] L. Marinangeli, F. Alijani, and S. H. Hosseinnia, "Fractional-order positive position feedback compensator for active vibration control of a smart composite plate," *Journal of Sound and Vibration*, vol. 412, pp. 1–16, 2018.

[24] W. Niu, B. Li, T. Xin, and W. Wang, "Vibration active control of structure with parameter perturbation using fractional order positive position feedback controller," *Journal of Sound and Vibration*, vol. 430, pp. 101–114, 9 2018.

[25] D. Feliu-Talegon, A. San-Millan, and V. Feliu-Batlle, "Fractional-order integral resonant control of collocated smart structures," *Control Engineering Practice*, vol. 56, pp. 210–223, 11 2016.

[26] Z. H. Wang and Y. G. Zheng, "The optimal form of the fractional-order difference feedbacks in enhancing the stability of a sdof vibration system," *Journal of Sound and Vibration*, vol. 326, pp. 476–488, 10 2009.

[27] A. G. Radwan, A. S. Elwakil, and A. M. Soliman, "On the generalization of second-order filters to the fractional-order domain," *Journal of Circuits, Systems and Computers*, vol. 18, pp. 361–386, 4 2009.

[28] R. Malti, X. Moreau, F. Khemane, and A. Oustaloup, "Stability and resonance conditions of elementary fractional transfer functions," *Automatica*, vol. 47, pp. 2462–2467, 11 2011.

5

[29] E. Ivanova, X. Moreau, and R. Malti, "Stability and resonance conditions of second-order fractional systems," 6 2018.

[30] S. Zhang, L. Liu, D. Xue, and Y. Q. Chen, "Stability and resonance analysis of a general non-commensurate elementary fractional-order system," *Fractional Calculus and Applied Analysis*, vol. 23, pp. 183–210, 2 2020.

[31] S. Sahoo, S. Saha Ray, and S. Das, "An efficient and novel technique for solving continuously variable fractional order mass-spring-damping system," *Engineering Computations (Swansea, Wales)*, vol. 34, no. 8, pp. 2815–2835, 2017.

[32] N. Sene and J. F. G. Aguilar, "Fractional mass-spring-damper system described by generalized fractional order derivatives," *Fractal and Fractional*, vol. 3, pp. 1–15, 7 2019.

[33] D. Pang, W. Jiang, S. Liu, and D. Jun, "Stability analysis for a single degree of freedom fractional oscillator," *Physica A: Statistical Mechanics and its Applications*, vol. 523, pp. 498–506, 6 2019.

[34] A. Adhikary, S. Sen, and K. Biswas, "Practical realization of tunable fractional order parallel resonator and fractional order filters," *IEEE Transactions on Circuits and Systems I: Regular Papers*, vol. 63, pp. 1142–1151, 8 2016.

[35] G. Tsirimokou, C. Psychalinos, A. S. Elwakil, and K. N. Salama, "Electronically tunable fully integrated fractional-order resonator," *IEEE Transactions on Circuits and Systems II: Express Briefs*, vol. 65, pp. 166–170, 2 2018.

[36] S. Kapoulea, C. Psychalinos, and A. S. Elwakil, "Power law filters: A new class of fractional-order filters without a fractional-order Laplacian operator," *AEU - International Journal of Electronics and Communications*, vol. 129, p. 153537, 2 2021.

[37] S. Mahata, N. Herencsar, and D. Kubanek, "On the design of power law filters and their inverse counterparts," *Fractal and Fractional*, vol. 5, p. 197, 11 2021.

[38] V. Sethi, M. A. Franchek, and G. Song, "Multimodal active vibration suppression of a flexible structure by loop shaping," in *Smart Structures and Materials 2005: Smart Structures and Integrated Systems*, vol. 5764, p. 348, SPIE, 5 2005.

[39] V. Sethi, G. Song, and M. A. Franchek, "Loop shaping control of a model-story building using smart materials," *Journal of Intelligent Material Systems and Structures*, vol. 19, pp. 765–777, 7 2008.

[40] J. Munoa, X. Beudaert, K. Erkorkmaz, A. Iglesias, A. Barrios, and M. Zatarain, "Active suppression of structural chatter vibrations using machine drives and accelerometers," *CIRP Annals - Manufacturing Technology*, vol. 64, pp. 385–388, 1 2015.

[41] C. a. Monje, Y. Q. Chen, B. M. Vinagre, D. Xue, and V. Feliu, *Fractional-order Systems and Controls. Fundamentals and Applications.* Springer-Verlag London Limited, 2010.

5

[42] M. Caputo, "Linear Models of Dissipation whose Q is almost Frequency Independent-II," *Geophysical Journal of the Royal Astronomical Society*, vol. 13, pp. 529–539, 11 1967.

[43] I. Podlubny, *Fractional Differential Equations, to Methods of Their Solution and Some of Their Applications*, vol. 198. San Diego : Academic Press, c1999., 1998.

[44] B. M. Vinagre and V. Feliu, "Optimal fractional controllers for commensurate order systems: A special case of the Wiener-Hopf method," in *Proceedings of the IEEE Conference on Decision and Control*, vol. 1, pp. 97–102, Institute of Electrical and Electronics Engineers Inc., 2000.

[45] D. Matignon, "Stability properties for generalized fractional differential systems," *ESAIM: Proceedings*, vol. 5, pp. 145–158, 1998.

[46] K. J. Åström, "Limitations on control system performance," in *ECC 1997 - European Control Conference*, pp. 3421–3426, Institute of Electrical and Electronics Engineers Inc., 4 1997.

[47] B. Vinagre, I. Podlubny, A. Hernandez, and V. Feliu, "Some approximations of fractional order operators used in control theory and applications," *Fractional calculus and applied analysis*, vol. 3, no. 3, pp. 231–248, 2000.

[48] A. Oustaloup, *Systemes asservis lineaires d'ordre fractionnaire : theorie et pratique*. Masson, 1983.

[49] R. M. Schmidt, G. Schitter, A. Rankers, and J. van Eijk, *The Design of High Performance Mechatronics*. Amsterdam: IOS Press, 2 ed., 2014.

5

6

Metamaterials with fractional-order resonators

The previous chapter considered using a fractional generalization of a second-order high-pass filter for active vibration control. An advantage of such an element is the possibility to create a high resonance peak with phase in the low-frequency region significantly smaller from +180˚. In the loop-shaping context, this can be used to achieve high loop gain at the targeted frequency with high phase margins at the cross-over frequencies, which directly leads to sensitivity in the shape of a deep notch with minimised secondary resonance peaks. Here, we use this element to create a bandgap in a metamaterial. The analysis shows that it is possible to create a deep bandgap without a secondary resonance peak, which, as we have seen in Chapter 3, is not possible in conventional metamaterials. In contrast to Chapter 5, which focuses on frequency domain analysis, we study the system's behaviour using the pseudo-pole analysis. This possibility to easily analyse the dynamics of systems with complicated dynamics is the main advantage of fractional-order system theory.

Elastic metamaterials with fractional-order resonators

Abstract *Elastic metamaterials incorporating locally resonating unit cells can create bandgap regions with lower vibration transmissibility at longer wavelengths than the lattice size and offer a promising solution for vibration isolation and attenuation. However, when resonators are applied to a finite host structure, not only the bandgap but also additional resonance peaks in its close vicinity are created. Increasing the damping of the resonator, which is a conventional approach for removing the undesired resonance peaks, results in shallowing of the bandgap region. To alleviate this problem, we introduce an elastic metamaterial with resonators of fractional order. We study a one-dimensional structure with lumped elements, which allows us to isolate the underlying phenomena from irrelevant system complexities. Through analysis of a single unit cell, we present the working principle of the metamaterial and the benefits it provides. We then derive the dispersion characteristics of an infinite structure. For a finite metastructure, we demonstrate that the use of fractional-order elements reduces undesired resonances accompanying the bandgap, without sacrificing its depth.*

6.1 Introduction

Metamaterials are structures with properties beyond those of their constituents, often composed of repeating patterns called unit cells. The term initially emerged from the study of structures capable of manipulating waves, that could be used to create perfect lenses, cloaking devices or superabsorbers. In this paper, we focus on mechanical metamaterials for the manipulation of elastic waves. An overview of historical developments as well as methods and trends in the field can be found in [1, 2]. A feature of metamaterials that offers a promising solution for vibration attenuation and isolation is the creation of bandgaps, i.e., ranges of frequencies in which vibrations cannot propagate through a structure. In elastic metamaterials, thanks to the use of locally resonating unit cells in their structure [3], the bandgaps can be created at much longer wavelengths than the lattice size, which is a clear benefit when compared with phononic crystals whose operating principle is described by Bragg scattering [4]. Within the unit cells, not only mechanical resonators but also passive and active electronic elements can be used, which increases the design freedom and scope of possible implementations.

When a finite resonant metastructure is considered, rather than an infinite metamaterial, it is important to examine the modal behavior, especially in the case of low-frequency vibrations [5]. Application of resonators to a finite host structure results not only in the creation of a bandgap but also introduces additional resonance peaks in the response. Dis-

persion characteristics of a lattice with resonators are related to the modal behaviour of a host structure [6, 7]. The introduction of the resonators leads to the splitting of resonance peaks corresponding to each mode of the host structure, similar to the effect that can be observed in single-mode systems with tuned mass dampers [8]. These additional peaks are located near the bandgap region, thereby compromising the achieved vibration isolation performance. The modes with resonances above the frequency of the bandgap contribute to the additional peaks below the bandgap region and vice versa.

In the majority of elastic metamaterials presented in the literature, second-order resonators are used. This approach simplifies the analysis and design but also results in a tradeoff between the depth of the bandgap region and the creation of unwanted resonance peaks. While pole placement or optimization-based designs have been proposed to address this issue [9, 10], these methods may not provide the necessary insight for the rational design of metamaterials.

In this paper, we investigate the application of fractional-order (FO) resonators in metamaterials and demonstrate that with this approach the tradeoff between the depth of the bandgap and creating unwanted resonance peaks can be relaxed. To facilitate the use of the tools from control theory, unit-cell level dynamics of the metamaterial are presented as feedback interconnection of an element representing the base structure and the resonator. The working principle of the studied metamaterial is demonstrated in an analysis of a single unit cell in isolation. Subsequently, we derive the dispersion characteristics for an infinite metamaterial structure. To confirm the benefits of the use of FO elements, we investigate vibration transmission through a finite metastructure.

The potential of FO calculus has been demonstrated in various engineering fields. In addition to its use in modelling of electrical, thermal, biomimetic systems, chaos and fractals [11–15], FO calculus has also been employed in the modelling of viscoelastic materials [16, 17]. Moreover, FO calculus has been found to enhance the performance of controllers, such as FO PID [18–21], and in the field of active vibration control, FO versions of Integral Resonant Controller (IRC) [22, 23], Positive Position Feedback (PPF) [24, 25], Negative Position Feedback (NPF) [26] and difference feedback for active damping [27] have demonstrated better performance than their integer-order counterparts. In the field of metamaterials, FO operators have been used for the modelling of viscoelastic damping phenomena [28–31]. In this work, FO resonators of commensurate order [32–34] as well as power-law generalizations of second-order elements [35–38] are studied in the context of elastic metamaterials. The theoretical framework provided by FO calculus allows for an extension of the design freedom of a system while preserving the advantages of linearity, making it possible to analytically determine the properties of the system.

The paper is structured as follows. In Section 6.2, we present background information on FO systems and FO resonators specifically. We also discuss the possible physical implementation of the studied elements. The main contribution of this work is presented in Section 6.3. First, we revisit a feedback model of an integer order metamaterial. Subsequently, we demonstrate the working principle of the metamaterial with an analysis of a single unit cell in isolation, as well as the derivation of the dispersion relationships of an infinite structure. The analysis of the dynamics of a metastructure with a finite number of unit cells is also conducted. In the concluding Section of the paper, we discuss the obtained results and possible directions for further research.

6.2 Background

6.2.1 Fractional-order systems

Fractional-order calculus has been developed to generalize conventional differentiation and integration to non-integer orders [35]. While there exists a vast number of definitions of FO operators, we use the Caputo derivative [39, 40] defined as

$$
{}_C\mathcal{D}^\alpha f(t) \triangleq \frac{1}{\Gamma(m-\alpha)} \int_0^t \frac{f^{(m)}(\tau)}{(t-\tau)^{\alpha-m+1}} d\tau,
\tag{6.1}
$$

where $\alpha \in \mathbb{R}^+$ is the order of differentiation and m is a positive integer such that $m-1 < \alpha < m$.

The Laplace transform of (6.1) is given by

$$
\mathcal{L}\left[{}_C\mathcal{D}^\alpha f(t)\right] = s^\alpha F(s) - \sum_{k=0}^{m-1} s^{\alpha-k-1} f^{(k)}(0).
\tag{6.2}
$$

Note, that for zero initial condition the Laplace transform of many FO operators is s^α, what greatly simplifies the design of FO controllers in the frequency domain.

A continuous-time FO system is given by a transfer function of the form

$$
H(s) = \frac{b_m s^{\beta_m} + b_{m-1} s^{\beta_{m-1}} + \cdots + b_0 s^{\beta_0}}{a_n s^{\alpha_n} + b_{n-1} s^{\alpha_{n-1}} + \cdots + a_0 s^{\alpha_0}},
\tag{6.3}
$$

with $a_i, b_i \in \mathbb{R}$. Changing the orders $\alpha_i, \beta_i \in \mathbb{R}^+$ in (6.3) may lead to dramatic changes in the dynamics of a system, for example from low-pass to high-pass filter [25]. For meaningful analysis, the character of an element should be preserved. To assure this, two variants of FO transfer functions presented bellow will be used.

In a commensurate-order [41] system all the orders of derivation are integer multiples of the base order α, i.e. $\beta_k = k\alpha$ with $k \in \mathbb{Z}^+$, so the transfer function (6.3) is given by

$$
H(s) = \frac{\sum_{k=0}^{m} b_k (s^\alpha)^k}{\sum_{k=0}^{n} a_k (s^\alpha)^k},
\tag{6.4}
$$

and can be presented as a pseudo-rational function $H(\lambda)$ of the variable $\lambda = s^\alpha$

$$
H(\lambda) = \frac{\sum_{k=0}^{m} b_k \lambda^k}{\sum_{k=0}^{n} a_k \lambda^k}.
\tag{6.5}
$$

A power-law [35–38] fractional-order system is described by a transfer function of the form

$$
H(s) = \left(\frac{\sum_{k=0}^{m} b_k s^k}{\sum_{k=0}^{n} a_k s^k} \right)^\alpha.
\tag{6.6}
$$

The stability of a FO system can be assessed by studying its transfer function [35]. In general, the denominator of (6.3) is not a polynomial and has an infinite number of roots.

Among them, a finite number of roots belonging to the principle sheet of Riemann surface will determine the systems stability. The fractional order system is bounded-input bounded-output stable if all of the roots of the denominator that are in the principle Reimann sheet and are not the roots of the numerator have negative real parts [42].

For a commensurate-order system represented by (6.5), the stability condition is

$$|\arg(\lambda_i)| > \alpha \frac{\pi}{2}, \tag{6.7}$$

where λ_i are the roots of the characteristic polynomial in λ [35]. In the case of power-law filters (6.6), the stability is concluded when the poles of the denominator $\sum_{k=0}^{n} a_k s^k$ lie in the left half complex plain [37].

6.2.2 Fractional-order resonators

In this Section, we review the available results relevant to fractional-order generalizations of second-order high-pass filters close to the limits of the stability, which will be used in the remainder of this paper. FO generalization of elementary transfer functions has been a topic of extensive study. Stability conditions, resonance conditions and characteristic frequencies of such filters were analysed in [32–34]. These results were generalized to systems of non-commensurate order in [43, 44]. The trajectories of marginally stable FO systems were studied in [45]. Closely related results were obtained for mechanical oscillators with components characterized by FO operators [46–49].

A commensurate order generalization of a second-order high pass filter is given by

$$R_\alpha(s) = \frac{K_R \left(\frac{s}{\omega_r}\right)^{2\alpha}}{\left(\frac{s}{\omega_r}\right)^{2\alpha} + 2\zeta_\alpha \left(\frac{s}{\omega_r}\right)^{\alpha} + 1}, \tag{6.8}$$

where $\alpha \in (0,1)$ denotes the order of the pseudo-poles of the system. The FO resonator (6.8) can be represented by a pseudo-rational transfer function

$$R_\alpha(\lambda) = \frac{K_R/\omega_r^{2\alpha} \, \lambda^2}{1/\omega_r^{2\alpha} \, \lambda^2 + 2\zeta_\alpha/\omega_r^\alpha \, \lambda + 1}, \tag{6.9}$$

with $\lambda = s^\alpha$, which is characterised by conjugate pair of pseudo-poles at

$$p_\alpha = -\zeta_\alpha \omega_r^\alpha \pm j\omega_r^\alpha \sqrt{1 - \zeta_\alpha^2}. \tag{6.10}$$

The stability condition (6.7) states, that the roots of a stable fractional-order transfer function must lie outside of a closed angular sector. For $\alpha = 1$ this condition is equivalent to the roots remaining in the left half complex plain and can only be satisfied with positive damping coefficients. For $\alpha \in (0,1)$, the stability region is larger and the transfer function (6.8) is stable for $\zeta_\alpha > -\cos(\frac{\pi}{2}\alpha)$ [33]. This leads to greater design freedom and allows for maintaining a high resonance peak for transfer functions with $\alpha < 1$.

Finding the frequency at which the magnitude response of (6.8) has a maximum in general, involves solving a nonlinear equation [32, 33]. However, for a marginally stable

(6.8) the resonance frequency always matches ω_n [33]. This allows us to derive simple approximations useful in the "lightly-damped" case. The resonance peak can be measured by a quality factor Q, determined by the maximum value of the peak, relative to the crossing point of the low and high-frequency asymptotes in the frequency response plot [50]. By evaluating the magnitude of (6.8) with the assumption that the fractional-order attenuator has the peak of response at $\omega = \omega_r$ we obtain

$$Q_\alpha = \frac{|R_\alpha(\omega_r)|}{|R_\alpha(\infty)|} = \left(\left(2\zeta_\alpha \sin\left(\frac{\pi}{2}\alpha\right) + \sin\left(\pi\alpha\right) \right)^2 + \left(2\zeta_\alpha \cos\left(\frac{\pi}{2}\alpha\right) + \cos\left(\pi\alpha\right) + 1 \right)^2 \right)^{-\frac{1}{2}}, \quad (6.11)$$

which reduces to $Q = \frac{1}{2\zeta_\alpha}$ for $\alpha = 1$.

The equivalent damping for an attenuator with fractional order α, that leads to the same Q-factor as for the integer order attenuator with ζ_r is given by

$$\zeta_\alpha = \zeta_r - \cos\left(\frac{\pi}{2}\alpha\right), \quad (6.12)$$

which is obtained by comparing the quality factor in (6.11) with its integer-order equivalent and finding ζ_α such that both are equal.

The power-law fractional-order generalization of a second-order high-pass filter is

$$\tilde{R}_\alpha(s) = \frac{K_R\left(\frac{s}{\omega_r}\right)^{2\alpha}}{\left(\left(\frac{s}{\omega_r}\right)^2 + 2\tilde{\zeta}_\alpha\left(\frac{s}{\omega_r}\right) + 1 \right)^\alpha}, \quad (6.13)$$

which is stable for $\tilde{\zeta}_\alpha > 0$ [37]. Using the same approach as for (6.8), the quality factor and the equivalent damping ratio are defined as

$$\tilde{Q}_\alpha = \frac{1}{(2\tilde{\zeta}_\alpha)^\alpha}, \qquad\qquad \tilde{\zeta}_\alpha = \frac{(2\zeta_r)^{1/\alpha}}{2}. \quad (6.14)$$

The frequency responses of integer and fractional-order resonators are compared in Figure 6.1. The influence of the gain K_R and natural frequency ω_r of the resonator are the same as in the integer-order case. Their change leads to modification of the magnitude and shift of the frequency response along the frequency axis respectively. At low frequencies, the magnitude of the frequency response is proportional to $\omega^{2\alpha}$, which is linked to the phase of $\alpha\pi/2$. This effect, as explained in [26], leads to a lower amplitude of introduced resonance peaks when the element is used for vibration control. In the high-frequency region, all the elements have a constant magnitude of the frequency response and the phase of 0. For the commensurate-order FO element (6.8), decreasing α leads to the widening of the resonance peak. At the same time, the phase close to the resonance frequency exceeds the low and high-frequency asymptotes. The phase of the power-law element (6.13) does not intersect the asymptotes, but the resonance peak narrows down as α is decreased.
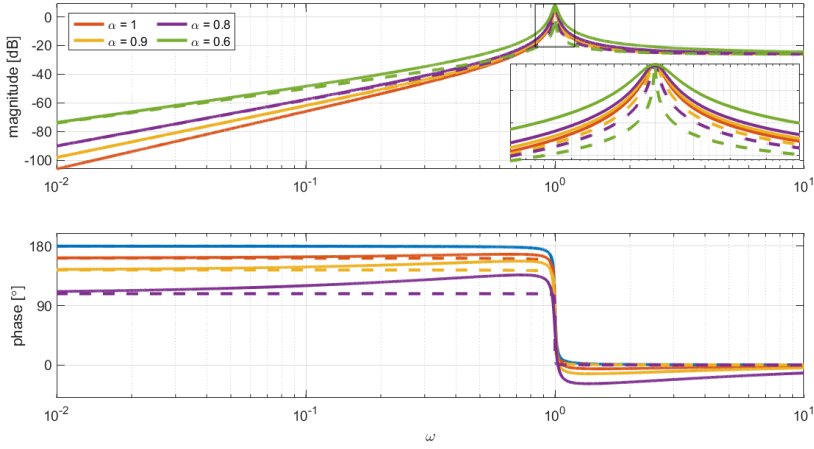
Figure 6.1: Frequency responses of commensurate-order (solid lines) and power-law (dashed lines) fractional-order resonators with different values of α. The values of the damping ratio are adjusted to maintain the same quality factor for all compared elements.

6.2.3 Physical implementation of fractional-order resonators

In active structures with sensors and actuators, the fractional-order resonators can be implemented as controllers with appropriate transfer functions. A common way to implement FO systems is to approximate them in an appropriate range of frequencies using finite-dimensional integer-order transfer functions. An overview of approximation techniques can be found in [51]. In continuous time, expansion-based and frequency-domain identification methods can be used to find the approximation. In the latter category, the approximation can be found analytically, like in the method of Oustaloup [52], or identified directly from the desired frequency response using commercial software. While direct discrete-time approximations of FO systems exist, it is also possible to discretise a continuous-time approximation, which yields satisfactory results if the sampling ratio is sufficiently high.

Alternatively, the fractional-order resonators can be implemented by shunting the transducers present in the structure with electronic components with FO dynamics. In [53, 54] the direct implementation of electronic resonators was studied. To the best of the author's knowledge, passive mechanical resonators with FO dynamics have not been developed yet. Similarly, emulation of an FO resonator dynamics be a higher number of integer-order resonators remains an open question.

6.3 Fractional-order metamaterials

In this section, we present the main contribution of the paper and study the application of fractional-order resonators in an elastic metamaterial. First, the dynamics of the system in the integer case are revisited. Second, the working principle is presented in an analysis of the dynamics of a single cell in isolation. Subsequently, we conduct the dispersion

analysis for an infinite structure. The section concludes with an investigation of vibration transmission through a finite structure.
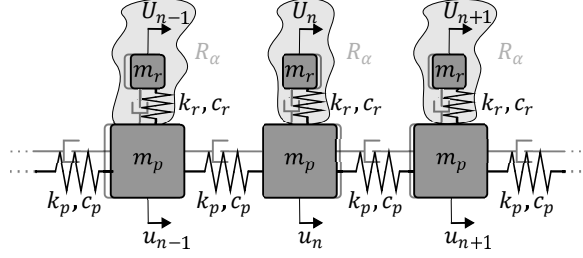
6.3.1 System model

Figure 6.2: A chain of masses with resonators. Grey loops indicate the resonators, whose dynamics are extended using fractional-order calculus.

Consider the granular metamaterial [55] presented in Figure 6.2. This choice of simple lumped parameter models allows us to focus on the underlying phenomena free from the distraction of irrelevant system complexities. Each unit cell of the metamaterial consists of a host-structure element with mass m_p connected to neighbour unit cells by stiffness k_p and viscous damper c_p. To the host element of each unit cell a resonator characterised by mass m_r, stiffness k_r and damping c_r is attached. The dynamics of nth unit cell are described by

$$m_p \ddot{u}_n = \quad k_p(u_{n-1} + u_{n+1} - 2u_n) + k_r(U_n - u_n)$$
$$+ c_p(\dot{u}_{n-1} + \dot{u}_{n+1} - 2\dot{u}_n) + c_r(\dot{U}_n - \dot{u}_n), \quad (6.15\text{a})$$
$$m_r \ddot{U}_n = \quad k_r(u_n - U_n) + c_r(\dot{u}_n - \dot{U}_n), \quad (6.15\text{b})$$

where u_n and U_n denote the displacement of the host element and the resonator of nth unit cell. To clearly present the band-gap region, $\omega_r << \omega_p$ is selected. The damping ratio ζ_p is small since it is determined by the host structure and $\zeta_r \approx 0$ is desired to create deep band gaps. By taking the Laplace transform of (6.15) and defining $\omega_p^2 = 2k/m$, $\omega_r^2 = k_r/m_r$, $K_R = k_r/k_p$, $\zeta_p = 2c_p/2\sqrt{2k_p m_p}$, $\zeta_r = c_r/2\sqrt{k_r m_r}$ we obtain

$$\left(\left(\frac{s}{\omega_p} \right)^2 + 2\zeta_p \left(\frac{s}{\omega_p} \right) + 1 + \frac{1}{2} \frac{K_r \left(\frac{s}{\omega_r} \right)^2 \left(2\zeta_r \left(\frac{s}{\omega_r} \right) + 1 \right)}{\left(\frac{s}{\omega_r} \right)^2 + 2\zeta_r \left(\frac{s}{\omega_r} \right) + 1} \right) u_n(s) = \frac{1}{2} (u_{n-1}(s) + u_{n-1}(s)), \quad (6.16)$$

with $u_i(s)$ denoting Laplace transform of the signal u_i.

The dynamics between neighbour unit cells can be represented as

$$u_n = T u_{n-1} + T u_{n+1}, \tag{6.17a}$$

$$T(s) = \frac{u_n(s)}{u_{n-1}(s)} = \frac{u_n(s)}{u_{n+1}(s)} = \frac{P(s)}{1 + P(s)R(s)} = P(s)S(s), \tag{6.17b}$$

$$P(s) = \frac{\frac{1}{2}}{\left(\frac{s}{\omega_p}\right)^2 + 2\zeta_p\left(\frac{s}{\omega_p}\right) + 1}, \tag{6.17c}$$

$$R(s) = \frac{K_R(\frac{s}{\omega_r})^2 \left(2\zeta_r\left(\frac{s}{\omega_r}\right) + 1\right)}{\left(\frac{s}{\omega_r}\right)^2 + 2\zeta_r\left(\frac{s}{\omega_r}\right) + 1}, \tag{6.17d}$$

which can be related to the "vibration reduction ratio" concept [56].

In the remainder of the paper, we study the effects that replacing the resonator (6.17d) with FO counterparts (6.8) and (6.13). The transfer function (6.17d) describes the relation between the displacement of the main body of the unit cell u_n and the force applied on it due to the presence of the resonator. For lightly damped resonators, the zero at $s = -\omega_r/(2\zeta_r)$ can be neglected, so the proposed FO generalization is justified.

6.3.2 Single unit-cell analysis

To demonstrate the root cause of the tradeoff between attenuation of vibrations in the bandgap and amplification at unwanted resonance peaks, as well as the proposed solution, consider the nth unit cell in isolation, driven by displacement n_{n-1} and with $u_{n+1} = 0$. If a fractional-order resonator (6.8) is used, the transmissibility (6.17b) is given by

$$T = \frac{\frac{1}{2}\left(\left(\frac{s}{\omega_r}\right)^{2\alpha} + 2\zeta_\alpha\left(\frac{s}{\omega_r}\right)^\alpha + 1\right)}{\left(\left(\frac{s}{\omega_r}\right)^{2\alpha} + 2\zeta_\alpha\left(\frac{s}{\omega_r}\right)^\alpha + 1\right)\left(\left(\frac{s}{\omega_p}\right)^2 + 2\zeta_p\left(\frac{s}{\omega_p}\right) + 1\right) + \frac{1}{2}K_R\left(\frac{s}{\omega_r}\right)^{2\alpha}}, \tag{6.18}$$

with $\alpha = 1$ representing the integer-order case. The response of the unit cell is characterized by a pair of pseudo-zeros at the location of the resonator poles p_α (6.10), which are related to the creation of a band gap in the metamaterial. The denominator of (6.18) contains terms with different fractional order, which complicates the analysis. In order to enable pseudo-pole analysis, $P(s)$ and $R(s)$ will be approximated at different frequency ranges.

Recall that $\omega_r < \omega_p$ are selected. At frequencies $\omega \gg \omega_r$ the response of the resonator with any value of α can be approximated by the gain K_R. The transmissibility (6.18) is then approximated as

$$T_{\omega > \omega_r} \approx \frac{\frac{1}{2}}{\left(\frac{s}{\omega_p}\right)^2 + 2\zeta_p\left(\frac{s}{\omega_p}\right) + 1 + \frac{1}{2}K_R}, \tag{6.19}$$

(a) integer-order, $\alpha = 1$, $\zeta_p = 0$, $\zeta_r \neq 0$ **(b)** commensurate-order, $\zeta_p = 0$, $\zeta_{r,\alpha=1} = 0$
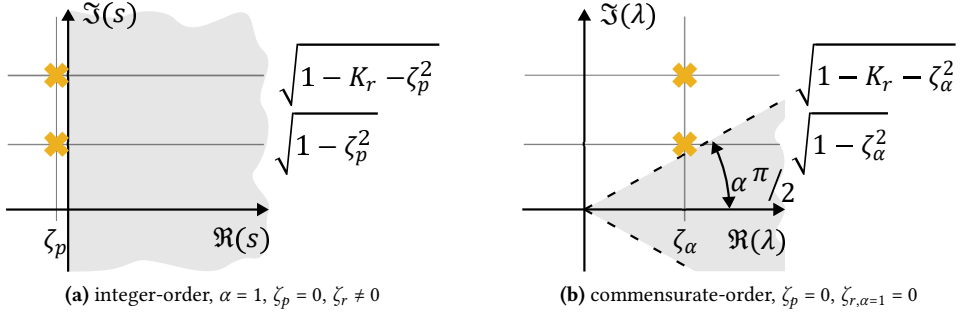
Figure 6.3: Locations of approximated (pseudo)poles of a single unit cell for a) $\omega >> \omega_r$ and b) $\omega \approx \omega_r$ or $\omega < \omega_r$. The absolut values of poles are scaled to enable comparison.

with poles at

$$p_{\omega > \omega_r} = -\zeta_p \omega_p \pm j\omega_p \sqrt{1 + K_R/2 - \zeta_p^2}.$$

The location of the poles is illustrated in Figure 6.3a. Since $\zeta_p \approx 0$ we have $\angle p_{\omega > \omega_r} \approx \pi/2$ and a resonance peak with high-quality factor is created. To reduce the height of this resonance peak, the value of ζ_p has to be increased.

In the vicinity of ω_r and at lower frequencies, the response of $P(s)$ can be approximated by the gain $\frac{1}{2}$. The transmissibility (6.18) is then approximated as

$$T_{\omega < \approx \omega_r} \approx \frac{\frac{1}{2}\left(\left(\frac{s}{\omega_r}\right)^{2\alpha} + 2\zeta_\alpha \left(\frac{s}{\omega_r}\right)^{\alpha} + 1\right)}{\left(\left(\frac{s}{\omega_r}\right)^{2\alpha} + 2\zeta_\alpha \left(\frac{s}{\omega_r}\right)^{\alpha} + 1\right) + \frac{1}{2}K_R\left(\frac{s}{\omega_r}\right)^{2\alpha}}, \tag{6.20}$$

which is characterized by a pair of pseudo-zeros at p_α (6.10) and a pair of poles at

$$p_{\omega < \approx \omega_r} = \frac{1}{1 + K_R/2}\left(-\zeta_\alpha \omega_r^\alpha \pm j\omega_r^\alpha \sqrt{1 + K_R/2 - \zeta_\alpha^2}\right).$$

From (6.12), for $\alpha = 1$ we have $\zeta_\alpha \approx 0$, so $\angle p_{\alpha|\alpha=1} \approx \angle p_{\omega < \approx \omega_r|\alpha=1} \approx \pi/2$, which means that the low-frequency resonance with high-quality factor is created. The presence of the resonance peak in the response is undesired since the function of a resonant metamaterial is to reduce vibration transmission. The height of the resonance peak can be reduced by increasing ζ_r, by the cost of also reducing the depth of the zero, since the damping of both poles and zeros of the structure increases simultaneously. This illustrates a fundamental tradeoff in elastic metamaterials.

With a fractional-order resonator with $\alpha < 1$, a damped low-frequency resonance peak can be created without affecting the damping ratio of the zero pair, therefore relaxing the aforementioned tradeoff. The pole locations, in this case, are presented in Figure 6.3b. For $\alpha < 1$, the high-quality factor of the resonator is obtained with $|\zeta_\alpha| > 0$ and the pair
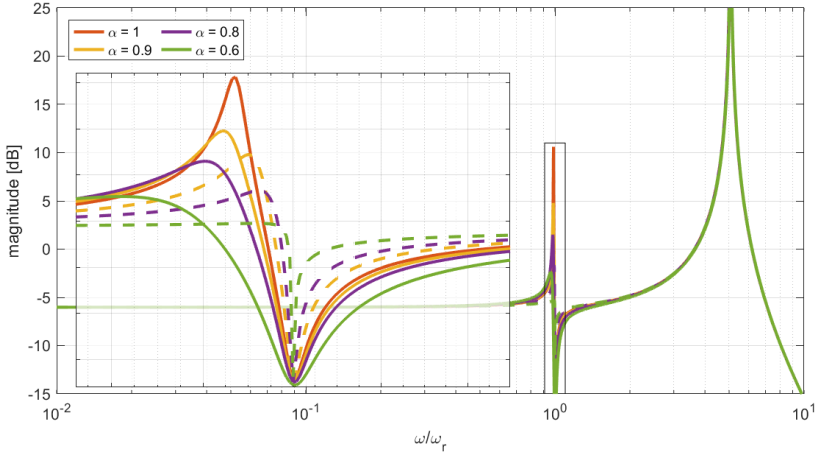
Figure 6.4: Infuence of α on the transmissibility of a single unit cell for resonators with commensurate-order (solid lines) and power-law (dashed lines) definitions. The damping of all the resonators is adjusted to maintain the same quality factor.

of the pseudo-zeros is placed close to the stability margins $\angle p_\alpha \approx \alpha\pi/2$. Simultaneously, $\angle p_{\omega<\approx\omega_r|\alpha<1} > \angle p_\alpha$ as the poles of the transmissibility are moved deeper into the stable region. A similar effect is expected for power-law resonators (6.13), however, the pseudo pole analysis in not possible due to the definition of resonator's dynamics.

The influence of commensurate-order and power-law FO resonators with different orders α on the transmissibility of a single unit cell is presented in Figure 6.4. For all the elements, a zero in transmissibility is created at ω_r and the same attenuation of vibration transmission at this frequency is obtained, as it is related to the location of (pseudo)zeros in the complex plain. The bandwidth at which the influence of the zeros is visible increases with decreasing α for commensurate-order resonators. For the power-law FO resonators decreasing α has the opposite effect, which can be related to the width of resonance peaks of (6.8) and (6.13). The benefit of the use of FO resonators is visible in the height of the resonance peak below ω_r. As α is decreased, the height of the resonance peak is decreased for both types of FO resonators, but the attenuation is significantly stronger in the power-law case. In the high-frequency region, if ω_r is sufficiently smaller than ω_p the second resonance peak remains unaffected with all the resonators.

6.3.3 Dispersion analysis of a fractional-order resonant metamaterial

In this subsection, we analyse the vibration transmission in an infinite elastic metamaterial with fractional order resonators using the dispersion method. Following the Bloch-Floquet theory, the spatial component of the harmonic wave solution for the nth unit cell can be expressed as $u_n(\omega) = \tilde{u}\left(\mu(\omega)\right)e^{j\mu n}$, where $\tilde{u}$ defines the amplitude of the wave motion and the exponential term describes the magnitude and phase changes as the wave
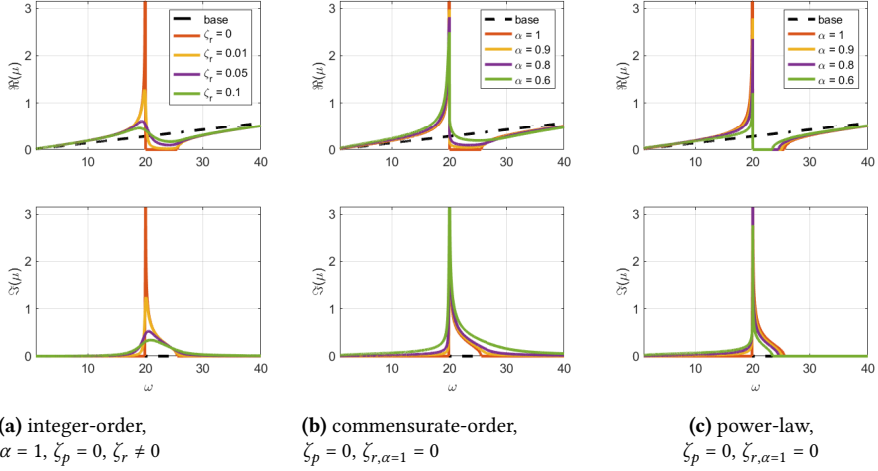
Figure 6.5: Dispersion diagrams for metamaterials with (a) integer-order and (b) commensurate-order or (c) power-law fractional-order resonators.

propagates thru the unit cells [1], with μ denoting the propagation constant. Wave propagation without magnitude change corresponds to real μ, while the imaginary part of μ indicates attenuation of the wave as it progresses thru the lattice. By implementing this in (6.17), considering nontrivial solutions ($\tilde{u} \neq 0$) and taking $s = j\omega$ we obtain

$$\cos(\mu) = \frac{1}{2T(\omega)}. \tag{6.21}$$

The attenuation factors can be found by solving (6.21) in terms of the propagation constant at given frequencies. The band gaps can be identified as ranges of frequencies in which the propagation constant takes pure imaginary values. A physical interpretation of this problem is related to wave propagation in a medium due to sustained sinusoidal excitation with dissipation limited to spatial attenuation [57].

To create the baseline for the analysis, Figure 6.5a presents the dispersion diagram of an integer-order metamaterial (i.e. with (6.8), $\alpha = 1$) with $\zeta_p = 0$ and different values of ζ_r. As the value of ζ_r increases, the maximal value of achieved attenuation factor $\Im(\mu)$ decreases, due to the lowering of the quality factor of the resonator. Simultaneously, the range of frequencies with non-zero attenuation increases, which can be used for widening the band-gap region [58, 59]. Moreover, the range of frequencies in which μ takes pure imaginary values disappears. This is caused by the phase of the frequency response of the resonator diverging significantly from the low and high-frequency asymptotes in the vicinity of the resonance peak.

Figure 6.5b presents a dispersion diagram for metamaterial with commensurate - order resonators and $\zeta_p = 0, \zeta_\alpha = -\cos(\alpha\pi/2)$. Since the quality factor of the resonator does not change with changing α, high values of attenuation ratio $\Im(\mu)$ are preserved. However,

values for $\alpha < 1$ are slightly lower than in the integer case due to the phase at the resonance lower than 90˚ [3]. Simultaneously, the width of the frequency range with $\Im(\mu) \neq 0$ increases. Similar to the integer-order case with $\zeta_r \neq 0$, the region of frequencies with pure imaginary μ disappears.

In Figure 6.5c a dispersion diagram of metamaterial with power-law fractional-order resonators and $\zeta_p = \tilde{\zeta}_\alpha = 0$ is presented. Similar to the commensurate-order case, the high attenuation ratio $\Im(\mu)$ is preserved, with only a slight decrease in maximal magnitude, when α decreases. The range of frequencies with $\Im(\mu) \neq 0$ extends towards lower values thanks to the lower phase of the frequency response of the resonator for $\alpha < 1$, and shrinks in the high-frequency side due to the narrowing of the resonance peak. The phase of the resonator does not extend beyond the high-frequency asymptote, which prevents the expansion of the band gap towards high frequencies. Simultaneously, the same leads to the reappearance of the range of frequencies with $\Re(\mu) = 0$.

6.3.4 Fractional-order resonant metastructure

The effectiveness of the proposed fractional-order resonators for attenuation of undesired resonance peaks in the vicinity of the bandgap region can be fully seen when a finite metastructure is considered. In a finite chain of N cells, the transmission of the vibrations from the base with displacement u_0 to the end of the chain can be calculated using (6.17) and assuming $u_{N+1} = u_N$ to represent the free boundary condition at the end of the chain. The dynamics of the complete resonant metastructure are then represented by

$$
\begin{bmatrix}
1 & -T & 0 & \cdots & & \cdots & 0 \\
-T & 1 & -T & 0 & & & \vdots \\
0 & \ddots & \ddots & \ddots & & & \\
\vdots & & -T & 1 & -T & & \vdots \\
& & & \ddots & \ddots & \ddots & 0 \\
\vdots & & & 0 & -T & 1 & -T \\
0 & \cdots & & & \cdots & 0 & -T & 1-T
\end{bmatrix}
\begin{bmatrix}
u_1 \\
\vdots \\
u_{n-1} \\
u_n \\
u_{n+1} \\
\vdots \\
u_N
\end{bmatrix}
=
\begin{bmatrix}
T u_0 \\
\vdots \\
\\
\\
\\
\vdots \\
0
\end{bmatrix}, \tag{6.22}
$$

and transmissability of the complete metastructure is defined as $T_{TOT}(\omega) = u_N(\omega)/u_0(\omega)$.

Figures 6.6 and 6.7 compare responses of finite metastructures with $N = 10$ cells with integer and fractional-order resonators, for different values of damping in the base chain. The lightly-damped case, presented in Figure 6.6, is showcased to clearly present the behaviour of the system, however, if implemented, may lead to instability of a structure since the commensurate-order resonator is not negative imaginary and e.g. time delays if a digital implementation of the resonator is used. When such a system is implemented, the stability of not only unit cells in isolation, but complete metastructure should be validated. The structure in Figure 6.7 has a significant dampening and would yield a stable system even in presence of the aforementioned effects.

In Figures 6.6a and 6.7a the effect of increasing the damping in the integer-order resonators is presented. As ζ_r increases, the resonance peaks created by the introduction of the resonators are damped, but with the price of increasing the vibration transmission within the band-gap region.

The use of commensurate-order resonators, presented in Figures 6.6b and 6.7b, reduces the undesired resonance peaks below and above the bandgap frequencies, without signifi-

cant shallowing of the depth of the bandgap. Moreover, the bandgap expands as the order α is decreased. These effects are related to the dispersion diagram present in Figure 6.5b and the widening of the regions with $|\Im(\mu)| > 0$.

In the power-law FO case, presented in Figures 6.6c and 6.7c, the additional resonance peaks are attenuated only at lower frequencies, the bandgap region narrows down as α is decreased and the bandgap is not diminished significantly. All effects again correspond to the dispersion diagram in Figure 6.5c. In many applications, however, the disadvantages of the power-law element, when compared with the commensurate-order FO resonator, will be however outweighed by its stability properties, thanks to the phase of the element remaining between the low and high-frequency asymptotes. Moreover, when a bandgap is placed below the lowest resonance frequency of a finite host structure no additional resonance peaks above the bandgap frequencies are created [6, 7].
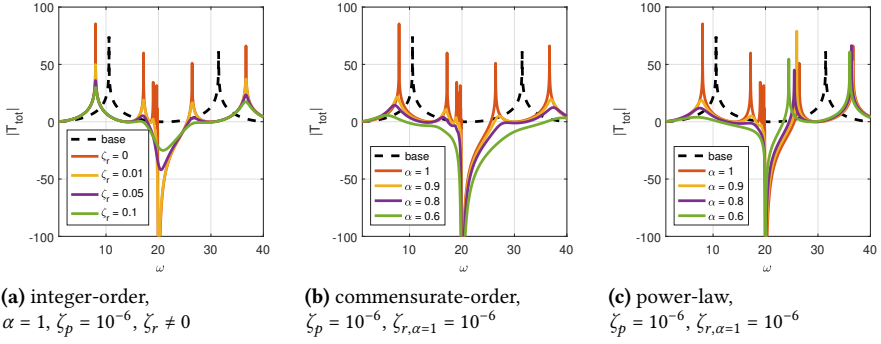

(a) integer-order,
$\alpha = 1$, $\zeta_p = 10^{-6}$, $\zeta_r \neq 0$

(b) commensurate-order,
$\zeta_p = 10^{-6}$, $\zeta_{r,\alpha=1} = 10^{-6}$

(c) power-law,
$\zeta_p = 10^{-6}$, $\zeta_{r,\alpha=1} = 10^{-6}$

Figure 6.6: Transmissablity of a finite metastructure of 10 cells with (a) integer-order and (b) commensurate-order or (c) power-law fractional-order resonators. The base chain of the metastructure is nearly undamped.
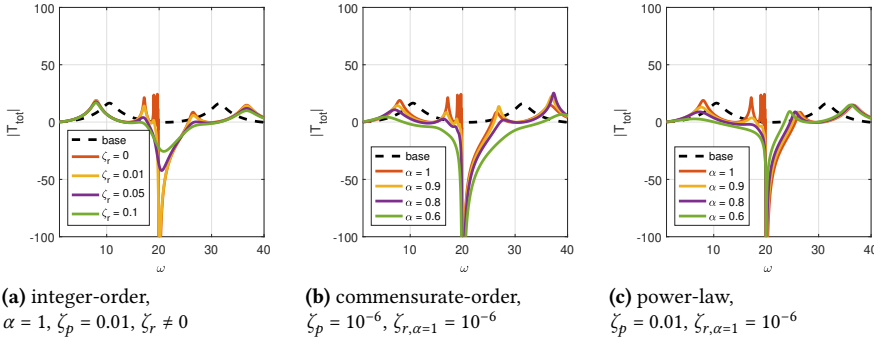
(a) integer-order,
$\alpha = 1$, $\zeta_p = 0.01$, $\zeta_r \neq 0$

(b) commensurate-order,
$\zeta_p = 10^{-6}$, $\zeta_{r,\alpha=1} = 10^{-6}$

(c) power-law,
$\zeta_p = 0.01$, $\zeta_{r,\alpha=1} = 10^{-6}$

Figure 6.7: Transmissablity of a finite metastructure of 10 cells with (a) integer-order and (b) commensurate-order or (c) power-law fractional-order resonators. The base chain of the metastructure has significant damping.

6.4 Conclusion

Elastic metamaterials with embedded resonators provide a promising approach to vibration isolation and attenuation. However, when resonators are applied to a finite host structure, not only the bandgap but also additional resonance peaks in its close vicinity are created. Increasing the damping of the resonator, which is a conventional approach for removing the undesired resonance peaks, results in shallowing of the bandgap region. We introduced an elastic metamaterial with fractional-order resonators and demonstrated that they can reduce the undesired resonances without significant changes to the maximal attenuation in the bandgap region. Both commensurate-order and power-law definitions of the fractional-order dynamics of the resonators were considered. The working principle of the proposed system was demonstrated on a single-unit cell and explained with the analysis of (pseudo)pole locations of the element. The properties of infinite metamaterial with FO resonators were studied using the dispersion method. Finally, we demonstrated that the fractional-order elements provide the desired effect by showcasing the transmissibility of a finite chain of unit cells. Analysis in this paper was limited to a granular metamaterial. While it can be expected that similar effects should be observed in other cases e.g. beams with translational resonators or piezoelectric patch actuators, detailed study is still required. The physical implementation of the studied elements also remains an open problem. While the FO resonators can be implemented as electronic or control elements, passive mechanical components with such dynamics still have to be developed.

References

[1] M. I. Hussein, M. J. Leamy, and M. Ruzzene, "Dynamics of phononic materials and structures: Historical origins, recent progress, and future outlook," *Applied Mechanics Reviews*, vol. 66, 7 2014.

[2] G. Ma and P. Sheng, "Acoustic metamaterials: From local resonances to broad horizons," 2 2016.

[3] I. L. Chang, Z. X. Liang, H. W. Kao, S. H. Chang, and C. Y. Yang, "The wave attenuation mechanism of the periodic local resonant metamaterial," *Journal of Sound and Vibration*, vol. 412, pp. 349–359, 1 2018.

[4] V. Laude, *Phononic Crystals: Artificial Crystals for Sonic, Acoustic, and Elastic Waves, 2nd Ed.* De Gruyter, 2020.

[5] H. Sun, X. Du, and P. F. Pai, "Theory of metamaterial beams for broadband vibration absorption," *Journal of Intelligent Material Systems and Structures*, vol. 21, pp. 1085–1101, 6 2010.

[6] C. Sugino, S. Leadenham, M. Ruzzene, and A. Erturk, "On the mechanism of bandgap formation in locally resonant finite elastic metamaterials," *Journal of Applied Physics*, vol. 120, p. 134501, 10 2016.

[7] C. Sugino, Y. Xia, S. Leadenham, M. Ruzzene, and A. Erturk, "A general theory for bandgap estimation in locally resonant metastructures," *Journal of Sound and Vibration*, vol. 406, pp. 104–123, 10 2017.

[8] J. P. Den Hartog, *Mechanical Vibrations*. New York: McGraw-Hill Book Company, Inc., 1940.

[9] C. Sugino, M. Ruzzene, and A. Erturk, "Design and analysis of piezoelectric metamaterial beams with synthetic impedance shunt circuits," *IEEE/ASME Transactions on Mechatronics*, vol. 23, pp. 2144–2155, 10 2018.

[10] G. Wang, J. Cheng, J. Chen, and Y. He, "Multi-resonant piezoelectric shunting induced by digital controllers for subwavelength elastic wave attenuation in smart metamaterial," *Smart Materials and Structures*, vol. 26, p. 025031, 1 2017.

[11] R. Caponetto, G. Dongola, L. Fortuna, and I. Petráš, *Fractional Order Systems: Modeling and Control Applications*. World Scientific Publishing Co., 1 2010.

[12] M. E. Meral and D. Çelík, "A comprehensive survey on control strategies of distributed generation power systems under normal and abnormal conditions," 1 2019.

[13] P. P. Singh and B. K. Roy, "Comparative performances of synchronisation between different classes of chaotic systems using three control techniques," *Annual Reviews in Control*, vol. 45, pp. 152–165, 1 2018.

6

[14] K. Cao, Y. Chen, and D. Stuart, "A fractional micro-macro model for crowds of pedestrians based on fractional mean field games," *IEEE/CAA Journal of Automatica Sinica*, vol. 3, pp. 261–270, 7 2016.

[15] F. Ge, Y. Chen, and C. Kou, "Cyber-physical systems as general distributed parameter systems: Three types of fractional order models and emerging research opportunities," *IEEE/CAA Journal of Automatica Sinica*, vol. 2, pp. 353–357, 10 2015.

[16] K. Adolfsson, M. Enelund, and P. Olsson, "On the fractional order model of viscoelasticity," *Mechanics of Time-Dependent Materials*, vol. 9, pp. 15–34, 1 2005.

[17] A. Bonfanti, J. L. Kaplan, G. Charras, and A. Kabla, "Fractional viscoelastic models for power-law materials," *Soft Matter*, vol. 16, pp. 6002–6020, 7 2020.

[18] Y. Q. Chen, "Ubiquitous fractional order controls?," in *IFAC Proceedings Volumes (IFAC-PapersOnline)*, vol. 2, pp. 481–492, Elsevier, 1 2006.

[19] Y. Q. Chen, I. Petráš, and D. Xue, "Fractional order control - A tutorial," in *Proceedings of the American Control Conference*, pp. 1397–1411, 2009.

[20] A. A. Dastjerdi, N. Saikumar, and S. H. HosseinNia, "Tuning guidelines for fractional order PID controllers: Rules of thumb," *Mechatronics*, vol. 56, pp. 26–36, 12 2018.

[21] A. A. Dastjerdi, B. M. Vinagre, Y. Q. Chen, and S. H. HosseinNia, "Linear fractional order controllers; A survey in the frequency domain," 1 2019.

[22] D. Feliu-Talegon, A. San-Millan, and V. Feliu-Batlle, "Fractional-order integral resonant control of collocated smart structures," *Control Engineering Practice*, vol. 56, pp. 210–223, 11 2016.

[23] A. San-Millan, V. Feliu-Batlle, and S. S. Aphale, "Application of a fractional order integral resonant control to increase the achievable bandwidth of a nanopositioner.," *IFAC-PapersOnLine*, vol. 50, no. 1, pp. 14539–14544, 2017.

[24] L. Marinangeli, F. Alijani, and S. H. Hosseinnia, "Fractional-order positive position feedback compensator for active vibration control of a smart composite plate," *Journal of Sound and Vibration*, vol. 412, pp. 1–16, 2018.

[25] W. Niu, B. Li, T. Xin, and W. Wang, "Vibration active control of structure with parameter perturbation using fractional order positive position feedback controller," *Journal of Sound and Vibration*, vol. 430, pp. 101–114, 9 2018.

[26] M. B. Kaczmarek and H. HosseinNia, "Fractional-order negative position feedback for vibration attenuation," *Fractal and Fractional*, vol. 7, p. 222, 3 2023.

[27] Z. H. Wang and Y. G. Zheng, "The optimal form of the fractional-order difference feedbacks in enhancing the stability of a sdof vibration system," *Journal of Sound and Vibration*, vol. 326, pp. 476–488, 10 2009.

6

[28] Y. Liu, D. Yu, H. Zhao, J. Wen, and X. Wen, "Theoretical study of two-dimensional phononic crystals with viscoelasticity based on fractional derivative models," *Journal of Physics D: Applied Physics*, vol. 41, p. 065503, 2 2008.

[29] M. Cajić, D. Karličić, S. Paunović, and S. Adhikari, "A fractional calculus approach to metadamping in phononic crystals and acoustic metamaterials," *Theoretical and Applied Mechanics*, vol. 47, no. 1, pp. 81–97, 2020.

[30] S. Sepehri, M. M. Mashhadi, and M. M. S. Fakhrabadi, "Wave propagation in fractionally damped nonlinear phononic crystals," *Nonlinear Dynamics*, vol. 110, pp. 1683–1708, 10 2022.

[31] W. Ding, J. P. Hollkamp, S. Patnaik, and F. Semperlotti, "On the fractional homogenization of one-dimensional elastic metamaterials with viscoelastic foundation," *Archive of Applied Mechanics*, vol. 93, pp. 261–286, 1 2023.

[32] A. G. Radwan, A. S. Elwakil, and A. M. Soliman, "On the generalization of second-order filters to the fractional-order domain," *Journal of Circuits, Systems and Computers*, vol. 18, pp. 361–386, 4 2009.

[33] R. Malti, X. Moreau, F. Khemane, and A. Oustaloup, "Stability and resonance conditions of elementary fractional transfer functions," *Automatica*, vol. 47, pp. 2462–2467, 11 2011.

[34] E. Ivanova, X. Moreau, and R. Malti, "Stability and resonance conditions of second-order fractional systems," 6 2018.

[35] C. a. Monje, Y. Q. Chen, B. M. Vinagre, D. Xue, and V. Feliu, *Fractional-order Systems and Controls. Fundamentals and Applications.* Springer-Verlag London Limited, 2010.

[36] B. Voß, C. Weise, M. Ruderman, and J. Reger, "Fractional-order partial cancellation of integer-order poles and zeros," *IFAC-PapersOnLine*, vol. 55, pp. 259–264, 1 2022.

[37] S. Kapoulea, C. Psychalinos, and A. S. Elwakil, "Power law filters: A new class of fractional-order filters without a fractional-order Laplacian operator," *AEU - International Journal of Electronics and Communications*, vol. 129, p. 153537, 2 2021.

[38] S. Mahata, N. Herencsar, and D. Kubanek, "On the design of power law filters and their inverse counterparts," *Fractal and Fractional*, vol. 5, p. 197, 11 2021.

[39] M. Caputo, "Linear Models of Dissipation whose Q is almost Frequency Independent-II," *Geophysical Journal of the Royal Astronomical Society*, vol. 13, pp. 529–539, 11 1967.

[40] I. Podlubny, *Fractional Differential Equations, to Methods of Their Solution and Some of Their Applications*, vol. 198. San Diego : Academic Press, c1999., 1998.

[41] B. M. Vinagre and V. Feliu, "Optimal fractional controllers for commensurate order systems: A special case of the Wiener-Hopf method," in *Proceedings of the IEEE Conference on Decision and Control*, vol. 1, pp. 97–102, Institute of Electrical and Electronics Engineers Inc., 2000.

[42] D. Matignon, "Stability properties for generalized fractional differential systems," *ESAIM: Proceedings*, vol. 5, pp. 145–158, 1998.

[43] Z. Jiao and Y. Q. Chen, "Stability of fractional-order linear time-invariant systems with multiple noncommensurate orders," *Computers and Mathematics with Applications*, vol. 64, pp. 3053–3058, 11 2012.

[44] S. Zhang, L. Liu, D. Xue, and Y. Q. Chen, "Stability and resonance analysis of a general non-commensurate elementary fractional-order system," *Fractional Calculus and Applied Analysis*, vol. 23, pp. 183–210, 2 2020.

[45] M. S. Tavazoei, M. Haeri, and N. Nazari, "Analysis of undamped oscillations generated by marginally stable fractional order systems," *Signal Processing*, vol. 88, pp. 2971–2978, 12 2008.

[46] J. F. Gómez-Aguilar, J. J. Rosales-García, J. J. Bernal-Alvarado, T. Córdova-Fraga, and R. Guzmán-Cabrera, "Fractional mechanical oscillators," *Revista Mexicana de Fisica*, vol. 58, no. 4, pp. 348–352, 2012.

[47] S. Sahoo, S. Saha Ray, and S. Das, "An efficient and novel technique for solving continuously variable fractional order mass-spring-damping system," *Engineering Computations (Swansea, Wales)*, vol. 34, no. 8, pp. 2815–2835, 2017.

[48] N. Sene and J. F. G. Aguilar, "Fractional mass-spring-damper system described by generalized fractional order derivatives," *Fractal and Fractional*, vol. 3, pp. 1–15, 7 2019.

[49] D. Pang, W. Jiang, S. Liu, and D. Jun, "Stability analysis for a single degree of freedom fractional oscillator," *Physica A: Statistical Mechanics and its Applications*, vol. 523, pp. 498–506, 6 2019.

[50] R. M. Schmidt, G. Schitter, A. Rankers, and J. van Eijk, *The Design of High Performance Mechatronics*. Amsterdam: IOS Press, 2 ed., 2014.

[51] B. Vinagre, I. Podlubny, A. Hernandez, and V. Feliu, "Some approximations of fractional order operators used in control theory and applications," *Fractional calculus and applied analysis*, vol. 3, no. 3, pp. 231–248, 2000.

[52] A. Oustaloup, *Systemes asservis lineaires d'ordre fractionnaire : theorie et pratique*. Masson, 1983.

[53] A. Adhikary, S. Sen, and K. Biswas, "Practical realization of tunable fractional order parallel resonator and fractional order filters," *IEEE Transactions on Circuits and Systems I: Regular Papers*, vol. 63, pp. 1142–1151, 8 2016.

[54] G. Tsirimokou, C. Psychalinos, A. S. Elwakil, and K. N. Salama, "Electronically tunable fully integrated fractional-order resonator," *IEEE Transactions on Circuits and Systems II: Express Briefs*, vol. 65, pp. 166–170, 2 2018.

6

[55] G. Gantzounis, M. Serra-Garcia, K. Homma, J. M. Mendoza, and C. Daraio, "Granular metamaterials for vibration mitigation," *Journal of Applied Physics*, vol. 114, p. 093514, 9 2013.

[56] S. M. Kim, S. Wang, and M. J. Brennan, "Comparison of negative and positive position feedback control of a flexible structure," *Smart Materials and Structures*, vol. 20, 1 2011.

[57] M. J. Frazier and M. I. Hussein, "Generalized Bloch's theorem for viscous metamaterials: Dispersion and effective properties based on frequencies and wavenumbers that are simultaneously complex," *Comptes Rendus Physique*, vol. 17, no. 5, pp. 565–577, 2016.

[58] J. M. Manimala and C. T. Sun, "Microstructural design studies for locally dissipative acoustic metamaterials," *Journal of Applied Physics*, vol. 115, p. 023518, 1 2014.

[59] Y. Y. Chen, M. V. Barnhart, J. K. Chen, G. K. Hu, C. T. Sun, and G. L. Huang, "Dissipative elastic metamaterials for broadband wave mitigation at subwavelength scale," *Composite Structures*, vol. 136, pp. 358–371, 2 2016.

6

7

Reset control for active vibration isolation in the presence of wide-band disturbances

In loop-shaping for the AVC system, presented in Chapter 2, there is a trade-off between the steep roll-off away from the target frequency and the sufficient phase margin at the cross-over frequencies. Such a trade-off can be relaxed by augmenting an LTI feedback loop with a nonlinear reset element, as demonstrated by multiple motion control examples. In the work presented in this chapter, we attempted to achieve the same in an active vibration isolation system. However, multiple resonance peaks in the closed-loop and wide-band excitations posed additional challenges for creating a well-performing reset control system. To ensure that the resetting is beneficial, we proposed to filter the reset triggering signals such that the reset is triggered only by a signal component in a desired frequency band. The idea enabling this work was to use the Best Linear Approximation approach to identify the dynamics of a nonlinear controller and closed-loop system instead of the plant. In this way, we gained insights into the behavior of reset systems in realistic conditions, which is not achievable with the commonly used describing function-based techniques.

Reset Control in the Presence of Wide-band Disturbances

Abstract *This paper explores the use of reset control in systems subjected to wide-band disturbances. Such excitation may result in too rare or excessive resetting, leading to deteriorated performance. Moreover, the commonly used Describing Function (DF) approximation for the frequency-domain design of reset systems does not represent the reset element's behavior under such conditions sufficiently, as it is defined for sinusoidal excitation. To address this, we present a design approach based on the analysis of power spectral densities (PSD) of the signals in the system and the use of Best Linear Approximations (BLA) of reset elements. In the first step, the dominant components in the PSD of the reset triggering signal are related to the frequency-domain properties of the reset element. To benefit from the resetting, it should lead to an increase in phase margins near the cross-over frequency. This is the case when the components at the cross-over frequency dominate the reset triggering signal. To ensure this, the use of a band-pass shaping filter is proposed. In the second step, the BLA of the rest element is used to represent its response to signal with a specific PSD in the frequency domain. This information is used to tune both the reset element and the shaping filter to achieve the desired performance and minimize the loss of gain at low frequencies. Closed-loop simulations show the feasibility of the method in achieving the desired behavior of the reset element, leading to improved resonance peak damping in the studied example.*

7.1 Introduction

Reset control systems are emerging as an augmentation for linear control, making it possible to overcome the inherent limitations related to the waterbed effect and the Bode's gain-phase relationship [1], which has been shown in multiple studies, especially in the field of precision motion control [2–6]. Depending on the design of the controller, improved transient response [7], steady-state tracking of reference signals or disturbance rejection [8, 9] can be achieved.

The research on reset control was initiated by Clegg, who proposed an integrator with output resetting whenever its input crosses zero. The benefits of the reset action can be clearly presented using the Describing Function (DF) approximation, as the reduction of the phase lag of the integrator by 52°. The use of reset systems was later extended, leading to more sophisticated elements like the "First-Order Reset Element" [10, 11], "Second-Order Reset Element" [12], or resetting the state to the fraction of the current value, known as partial resetting [13]. An element especially suited for practical adoption is "Constant-in-Gain, Lead-in-Phase" (CgLp) [14], which, based on DF analysis, can provide phase lead

while maintaining constant gain at a selected range of frequencies. This property can be used to increase the phase margins of control systems, leading to performance improvements.

Reset control systems can be designed using loop-shaping in the procedure analogous to the design of commonly employed PID controllers [15], making them suitable for wide adoption in the industry. The most popular frequency domain design methods for reset systems are based on the sinusoidal input describing functions [15–20]. However, since the reset systems are non-linear and the superposition principle does not apply, these methods are not able to capture the behaviour of the system in the presence of wide frequency band disturbances. Such disturbances may originate from systems surrounding (e.g. floor vibrations), be a result of noisy signals used for control, or parasitic dynamics in the system. Wide-band excitation may lead to too rare or excessive resetting. In both cases, the behavior of the reset control system is different than expected based on DF, and its benefits are not observed. This poses a challenge in the design of reset systems for many real-life applications, making the existing reset systems unsuitable in many cases.

This chapter presents an approach to the design of reset control systems for applications with wide-band excitations. First, the PSD or a reset triggering signal is analyzed, and the dominant frequencies are related to the reset action. The behavior of the reset element in the presence of a signal with specific PSD is represented in the frequency domain using the Best Linear Approximation (BLA). To ensure that the response of the reset element, as well as the response of a closed-loop reset system, follow the predictions from the DF, a method to tune the shaping filters is proposed. The validity of the approach is illustrated with simulations.

The structure of the chapter is as follows. In Section 7.2 the preliminaries of reset control and the BLA are given. Section 7.3 presents the design of a linear and reset controller for active vibration isolation in an example introducing the problem. Analysis of the reset triggering signal's PSD is provided in Section 7.4. The open-loop behaviour of a FORE subjected to wideband noise is studied in Section 7.5. The result of closed-loop simulations are presented in Section 7.6. Lastly, the conclusions of this chapter are given in Section 7.7.

7.2 Preliminaries

In this section, we present the studied class of reset systems as well as their commonly used frequency-domain approximations. Moreover, we introduce the Best Linear Approximations of non-linear systems, which will be used as a new design tool for rest control systems.

7.2.1 Reset systems

The state-space representation of the reset element is

$$R : \begin{cases} \dot{x}_r(t) = A_r x_r(t) + B_r u_r(t), & \rho(t) \neq 0, \\ x_r(t^+) = A_\rho x_r(t), & \rho(t) = 0 \\ y_r(t) = C_r x_r(t) + D_r u_r(t) \end{cases} , \tag{7.1}$$

where $x_r \in \mathbb{R}^{n_r}$ is the state of R, $x_r(t^+) = x_r^+ = \lim_{\epsilon \to 0^+} x(t+\epsilon)$ is the after reset state value, $u_r \in \mathbb{R}^m$ is the input of R, $y_r \in \mathbb{R}^m$ is the output of R and A_r, B_r, A_ρ, C_r, D_r are constant matrices of appropriate dimensions.

The base linear system (BLS) R_{bls} is an LTI system with a state-space realization

$$(A_r, B_r, C_r, D_r) \tag{7.2}$$

and describes the dynamics of R in the absence of reset. The reset is triggered by a signal $\rho(t)$. The linear reset law $x_r^+ = A_\rho x_r(t)$ describes the change of state that occurs at reset instants $t_k, k = 1, 2, \ldots$, that is when the reset condition $\rho = 0$ is satisfied.

Among many methods for the stability analysis of reset systems [21–23], three are especially well suited for practical frequency-domain design, namely, the H_β condition [13], passivity-based approach [24], and the Negative Imaginary Systems theory [25].

A specific type of reset element which is of concern in the paper is First Order Reset Element (FORE), represented by (7.1) with

$$A_r = -\omega_r, \qquad B_r = \omega_r, \qquad C_r = 1, \qquad D_r = 0, \qquad A_\rho = \gamma,$$

where ω_r denotes the corner frequency of the element and $\gamma \in [-1, 1]$. In the transfer function manipulations, the elements can be represented by $\dfrac{1}{s/\omega_r + 1}\!\!\nearrow^{\gamma}$, where the arrow indicates the resetting action.

7.2.2 Describing function representation

The Higher-Order Sinusoidal Input Describing Function (HOSIDF) [16] is a quasi-linearisation of a non-linear element that considers its steady-state response to a sinusoidal excitation. The non-linear element is considered as a virtual harmonic generator, and HOSIDF of nth order is defined

$$H_n(j\omega) = \frac{a_n(\omega)e^{j\phi_n(a_0,\omega)}}{a_0}, \tag{7.3}$$

where a_n and ϕ_n denote the nth component of the Fourier series expansion of the steady-state output of the element for a sinusoidal input.

The first-order HOSIDF (DF) of an open-loop reset element has been derived in [26], and the higher-order components were presented in [27]. In [20], the HOSIDF for a closed-loop system with a reset controller was introduced, and the calculation necessary for the HOSIDF analysis of reset systems were implemented in the form of a user-friendly Matlab toolbox.

7.2.3 CgLp

Constant-in-Gain, Lead-in-Phase (CgLp) [14] consists of a reset lag element in series with a linear lead filter. In the FORE-based version

$$R = \frac{1}{s/\omega_r + 1}\!\!\nearrow^{\gamma}, \qquad\qquad D(s) = \frac{s/\omega_{r,\alpha} + 1}{s/\omega_f + 1}, \tag{7.4}$$
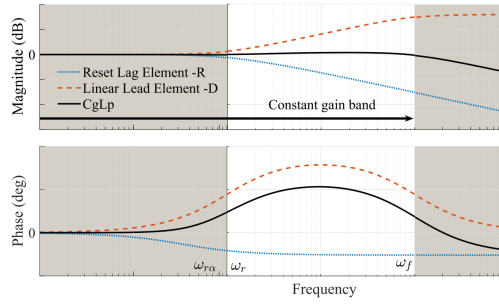
Figure 7.1: The concept of using a combination of a reset lag and a linear lead element to form a CgLp element [14].

where the corner frequency of the lead filters $\omega_{r,\alpha} = \alpha\omega_r, \alpha \in \mathbb{R}$ is adjusted to account for a shift in corner frequency of the lag filter due to resetting action.

The phase lead in frequency range (ω_r, ω_f) is obtained using the reduced phase lag of the reset lag element (when the first harmonic of HOSIDF is considered) combined with a corresponding lead element. Ideally, the gain of the reset lag element should be cancelled out by the gain of the corresponding linear lead element, which creates a constant gain behaviour. This concept is illustrated in Fig.7.1.

7.2.4 Best linear approximation of a non-linear system

The Best Linear Approximation (BLA) is based on the idea that a non-linear system can be represented by a combination of an LTI model and non-linear disturbance, both of which depend on the power spectrum of the input signal [28]. The methodology to obtain the (BLA) is well established and used mainly for system identification. The key results have been derived for the special Wiener systems, represented by the Volterra series. The reset systems that are the focus of this paper have not been studied in this framework. However, in [20], it has been proven that the considered reset systems are convergent for inputs in the form of Bohl functions, which include the multisine signals often used for BLA estimation. While the class of convergent systems can not be straightforwardly related to the classes of Volterra and special Wiener systems [29], systems in these classes have similar properties. Most importantly, for a given input signal, the convergent systems have a unique globally asymptotically stable solution, and if the input is periodic, then the corresponding steady-state solution is also periodic with the same period [30]. This justifies the attempt to use the BLA of reset systems in a reset controller design procedure.

The BLA can be obtained nonparametrically by performing classical frequency response function (FRF) measurements [28]

$$G_{BLA}(j\omega_k) = \frac{S_{yu}(j\omega_k)}{S_{uu}(j\omega_k)}, \tag{7.5}$$

where $S_{yu}(j\omega_k)$ is the cross-power spectrum between the output y and the input u of the system, and $S_{uu}(j\omega_k)$ is the auto-power spectrum of the input. The BLA can also be measured in closed-loop systems [31], including noise and disturbance signals. The appro-

priate selection of excitation signals and signal processing techniques for BLA estimation are key to obtaining reliable results. While the framework also allows for the quantification and characterization of non-linear distortions, this is beyond the scope of this work.

7.3 Problem description

In this section, the problem under the study is presented. First, we introduce the plant and objectives of the control systems. Subsequently, we present the conventional LTI control solution and its limitations as well as a reset-based alternative. Finally, we show the challenges related to implementing reset control in systems with wideband disturbances.

7.3.1 Plant

Consider a vibration isolation system presented in Fig. 7.2, consisting of a mass to be isolated with position x_2 on a shaking base with x_1. In this work, we focus on reducing the influence of the base vibration $\ddot{x}_1$ (with a PSD specified in [32]) on the acceleration $\ddot{x}_2$ of the isolated mass using a feedback controller.

The dynamics of the plant are captured by the transmissibility

$$P_t(s) = \frac{\ddot{x}_2(s)}{\ddot{x}_1(s)} = \frac{1}{\frac{s^2}{\omega_p^2} + 2\zeta \frac{s}{\omega_p} + 1},$$
(7.6)

and compliance

$$P_c(s) = \frac{\ddot{x}_2(s)}{F_d(s)} = \frac{s^2/k}{\frac{s^2}{\omega_p^2} + 2\zeta \frac{s}{\omega_p} + 1},$$
(7.7)

with ω_p = 104 Hz denoting the resonance frequency, stiffness k = 2.39 · 10^7 N·m/s, damping ratio of the plant ζ_p = 0.0022. In the design of the feedback system a delay τ = 0.7 ms should be also included.

Since the system consists of a non-linear element, the sequence of elements in the loop matters, and linear elements placed before and after the reset element must be distinguished. To reflect this, we consider a feedback controller consisting of linear elements $C_1(s)$ and $C_2(s)$, and the reset element R. Different fixed-structure components that constitute the controller (for example, integrator, low-pass filter, or lead filter) may be placed
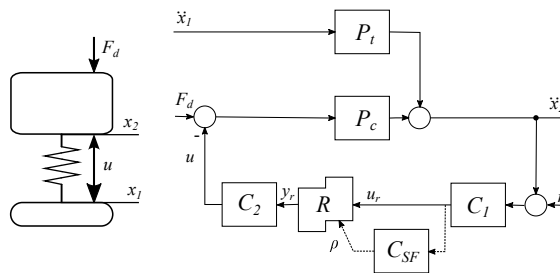

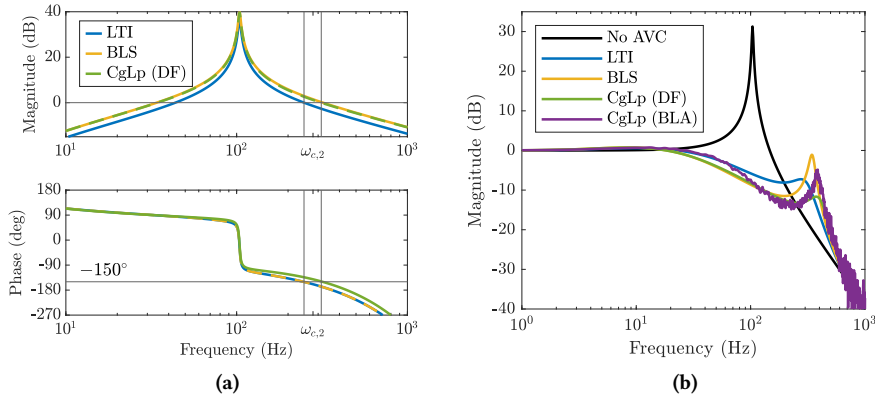**Figure 7.2:** Closed-loop diagram of a reset control system for AVC

Figure 7.3: (a) Open-loop with the different controllers. An optimal shape is a triangular shape centered at the resonance frequency. Second crossover frequency $\omega_{c,2}$ is indicated with the vertical line, for both the LTI and BLS controller. **(b)** Transmissibility from x_1 to x_2 of the system with no AVC and with different strategies implemented, showing the improvement in disturbance rejection performance. The Best Linear Approximation (BLA) highlights the deteriorated performance under wideband noise conditions.

either in $C_1(s)$ or $C_2(s)$, leading to different behavior of the reset system. The behavior of the system can also be influenced by placing a linear shaping filter $C_{SF}(s)$ on the reset triggering signal ρ [17]. The influence of the measurement noise n and direct disturbance forces F_d are considered negligible in the analysis of the system.

7.3.2 LTI Controller design

To dampen the resonance peak of the plant, the Linear Time-Invariant (LTI) controller employs Direct Velocity Feedback (DVF), as it is common in practice [33]. Since acceleration is measured as an output of the plant, the DVF has a transfer function

$$C_v(s) = \frac{K_v}{s + \omega_v}, \tag{7.8}$$

and its parameters are presented in Tab. 7.1. Such a controller results in a triangular loop gain $C_v(s)P_c(s)$ presented in Fig. 7.3a with crossover frequencies $\omega_{c,1}$ and $\omega_{c,2}$, at which $|C_v(\omega_{c,2})P_c(\omega_{c,2})| = 1$. These crossover frequencies and corresponding phase margins are key to the stability and performance of the system. The maximal gain of the controller K_v resulting in 30° phase margin at the second crossover frequency is selected. The achievable gain is limited by the phase loss due to the time-delay in the system.

Table 7.1: Parameters of the controllers, where the BLS also functions as the linear part of the reset controller.

	K_v	ω_v [Hz]	$\omega_{c,2}$ [Hz]	PM [°]
LTI	$7.2 \cdot 10^4$	5	248	30
BLS	$1 \cdot 10^5$	5	313	12

7.3.3 Reset Controller design

Increasing the gain of the controller while maintaining the desired phase margins would lead to a stronger reduction of the system's transmissibility, without sacrificing stability. To make this possible, a CgLp element is introduced to the control structure. In this example, the liner controller with increased gain has a phase margin at the $\omega_{c,2}$ of only 12°, indicated with Base Linear System (BLS) in Fig. 7.3a. The CgLp element provides an additional 18° of phase lead (analyzed with DF), resulting in the same combined value as in the LTI system.

   The desired amount of phase provided by the CgLp element can be achieved with different combinations of parameter values. In this first example, the element was constructed with ω_r = 150 Hz, ω_f = 10 kHz, α = 1.62 and γ = 0. Referring to the control structure in Fig. 7.2, non-linear element R is equal to the FORE part of CgLp and

$$C_1(s) = 1, \qquad C_{SF}(s) = 1, \qquad C_2(s) = C_v(s)D(s),$$

where C_2 consists of the lead part of the CgLp (7.4) and the DVF (7.8). The parameters of the controller are presented in Tab. 7.1 under BLS.

   The sequence of elements in the control loop does not influence the DF of the system but results in different behaviour, which is indicated by higher-order HOSIDF [18, 20]. The selection of the specific architecture and parameter values will be the subject of analysis in the remainder of the paper.

7.3.4 Problem identification

The closed-loop transmissibility between $\ddot{x}_1$ and $\ddot{x}_2$ of the system is presented in Fig. 7.3b. The DF approximation of the reset system suggests a stronger disturbance rejection than in the LTI case without creating an excessive resonance peak close to $\omega_{c,2}$. However, when a time simulation of the rest system is performed, the resulting BLA shows a significant resonance peak. This suggests that the reset system is not effective. The DF-based analysis of a reset element assumes single sinusoidal excitation and cannot capture the behavior of a reset system excited by a signal with an arbitrary power spectrum. This is due to the fact that the superposition principle does not apply. In the remainder of the paper, we show a design strategy to achieve the desired performance.

7.4 PSD of the reset triggering signal in closed-loop

The sequence of reset instances for a system excited by a multi-harmonic signal is not merely the sum of the reset instances caused by each harmonic independently. Figure 7.4 presents the Power Spectral Density (PSD) of the reset triggering signal ρ in the closed-loop simulation, along with the PSD of flor excitation signal used. In the case studied in the
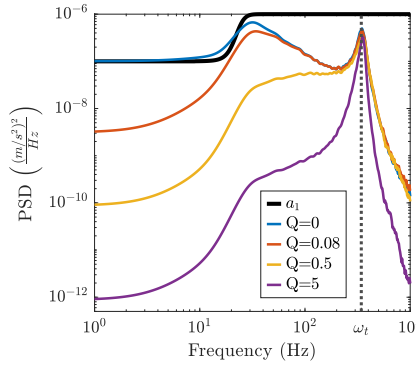
Figure 7.4: PSD of floor disturbance profile a_1 [32] and PSD of the reset triggering signal ρ in closed-loop simulation for different widths Q of the BPF. The dotted line denotes the closed-loop resonance frequency, $\omega_t = 343$Hz.

previous section ($Q = 0$), the reset triggering signal contains a wide range of frequencies. It is dominated by low-frequency components with a smaller peak around the second crossover frequency. Such a spectrum indicates a complicated reset sequence, as multiple components with similar amplitudes and different frequencies constitute the signal.

To benefit from the properties of the CgLp element, it must provide a phase lead at a desired frequency, in this case around $\omega_{c,2}$. To ensure this, we propose to shape the reset triggering signal such that a single frequency is dominant. The PSD of the reset triggering signal $S_\rho(\omega)$ is influenced by four factors in the control system design. If the reset element is represented by its DF $R_{DF}(j\omega)$, the $S_\rho(\omega)$ can be written in a quasi-linearised form:

$$S_\rho(\omega) = |H_{\rho d}(j\omega)P_t(j\omega)|^2 S_{x_1}(\omega), \tag{7.9}$$

$$H_{\rho d}(j\omega) = \frac{C_{SF}(j\omega)C_1(j\omega)}{1 + C_1(j\omega)P_c(j\omega)C_2(j\omega)R_{DF}(j\omega)}. \tag{7.10}$$

First, the excitation spectrum $S_{x_1}(\omega)$ is often known but generally cannot be easily influenced. For this reason, we do not study it further. The second factor is the sequence of the linear elements in the controller, as $C_1(j\omega)$ appears both in the numerator and denominator, while $C_2(j\omega)$ can be only seen in the denominator. Exploring this relationship may be interesting in the context of the continuous reset architecture [18]. However, for simplicity, $C_1 = 1$ will be used in the reminder of this work. Third, the $S_\rho(\omega)$ also depends on the dynamics of the reset element, denoted with $R_{DF}(j\omega)$. However, since the reset element is nonlinear, this relationship is hard to capture and using it requires extensive simulations or experiments. Fourth, the shaping filter dynamics $C_{SF}(s)$ determine $S_\rho(f)$. As this factor seems the easiest to control, it will be our focus in the reminder of this paper.

To make a single frequency dominant in $S_\rho(f)$ we apply the band-pass shaping filter

$$C_{SF}(s) = \frac{\frac{\omega_c}{Q}s}{s^2 + \frac{\omega_c}{Q}s + \omega_c^2}, \tag{7.11}$$

with $|C_{SF}(j\omega_c)| = 1$ at the center frequency ω_c. The width of the filter is determined by the value of Q, with a larger value resulting in a more narrow filter.

In Fig. 7.4, the effect of shaping ρ with different BPF widths on S_ρ in closed-loop is shown. As the band-pass filter becomes more narrow, the target frequency ω_t becomes more dominant in the reset triggering signal since the magnitude of the low-frequency content becomes smaller. This should enable benefiting from reset at the desired frequency range.

7.5 Open-loop behaviour of a FORE in the presence of wideband disturbances

Before showing the actual BLA of a reset system with wideband input signals, we present a time-domain illustration of a reset element's behaviour in Fig. 7.5. In the figure, we study different cases of the response of a reset element with a single sinusoidal input signal u_r with frequency ω_{u_r}. In each case, the resets are forced by a signal ρ with a different frequency ω_ρ.

The standard case, e.g. considered in DF analysis, is presented in Fig. 7.5b. The reset is triggered by ρ, which has the same frequency as the input signal u_r.

Excessive resetting is illustrated in Fig. 7.5a, where the resetting frequency is much higher than the frequency of the input signal. In such a case, the magnitudes of the FORE's response decrease, as there is not enough time for the response to rise to the values obtained by the BLS of the element. The extent of the magnitude decreases is related to the corner frequency of the element, ω_r, in a similar way as it defines the speed of the step response for linear systems.

When the resetting frequency is much lower than the input frequency, the reset action has a minor influence on system behaviour, as illustrated in Fig. 7.5c. In such a case, the response of the reset element should closely match the one of its BLS, and no advantage of the reset element will be exhibited in frequency domain.

The behavior of a reset element with an input signal with a specific PSD is captured in the frequency domain by the BLA. In Fig. 7.6, the BLA of FORE in open-loop with and without band-pass filters is presented. The parameters of FORE are $\omega_r = 380$ Hz, $\alpha = 1.11$ and $\gamma = 0.4$. The input signal u_r of FORE is obtained from a closed-loop simulation without a shaping filter. In an open-loop simulation, the reset triggering signals pass through filters with various widths Q. In each case, the BLA is calculated between the input and the output of the FORE. The BLA are compared to the DF of FORE with the same parameters and without the shaping filer.

At low frequencies, the BLA for all filter widths exhibit a smaller magnitude when compared to the DF. This behavior is related to excessive resetting, similar to the presented case in Fig. 7.5a. The resets are triggered with a high frequency, related to the dominant components of ρ presented in Fig. 7.4. When narrower band-pass filters are used, the components of ρ near the closed-loop resonance frequency ω_t become more dominant, and stronger gain loss at low frequencies can be seen in the BLA.

The BLA of the reset system matches the DF only within the frequency range close to the frequency of the reset triggering signal. Fig. 7.6b highlights the BLA of FORE near the closed-loop resonance frequency ω_t. Selecting a band-pass filter with $Q = 0.5$ results
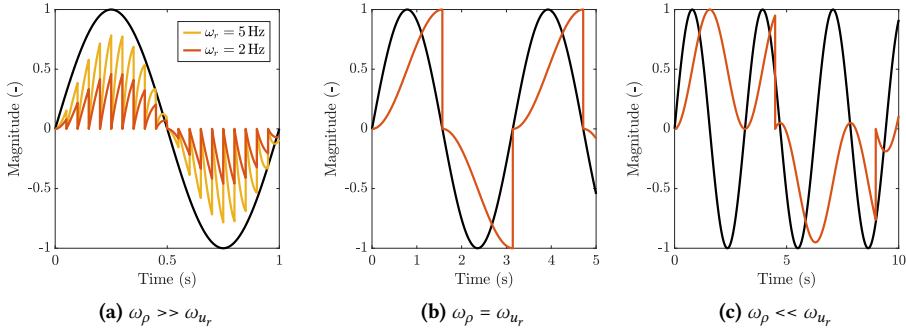
Figure 7.5: Simplified time-domain illustration of the behaviour of a reset system, when input frequency ω_{u_r} and the reset frequency ω_ρ are not necessarily the same. The input (black) is a single sine wave. a) Resetting too fast. Depending on ω_r of FORE being closer to ω_ρ, the gain of the output is closer to its input. b) Standard situation for a Clegg Integrator. Resets take place with the input frequency. c) Clegg Integrator with slow resetting.
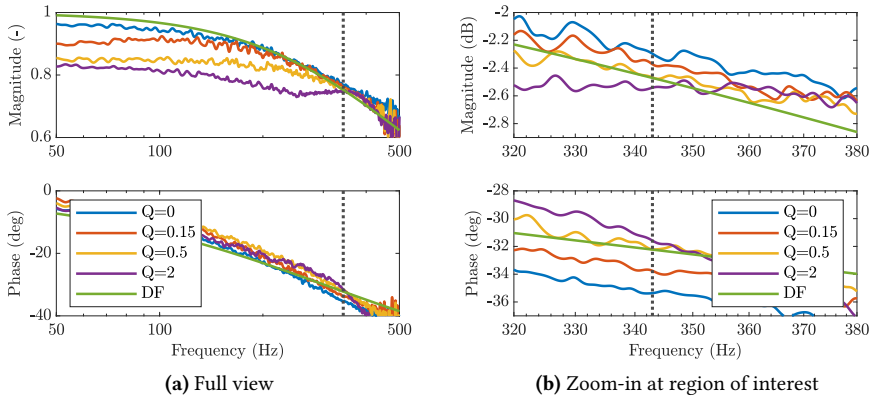
7

Figure 7.6: BLA between y_r in open-loop for different BPF widths and u_r in closed-loop without BPF, compared to DF of FORE. The closed-loop resonance frequency is indicated with the dotted line, which is the desired frequency for matching.
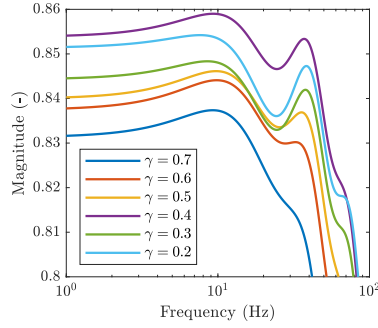
Figure 7.7: BLA of FORE in open-loop for different values of γ. The corresponding value of ω_r is maximised, to reduce gain loss.

in the closest match between the BLA and the DF of the element, at the target frequency. The rigorous explanation why this is the case should be a subject of future study.

At high frequencies, above the resonance frequency ω_t, the response of the reset element is dominated by the higher harmonics of the reset frequency, which are represented by spikes in the BLA, which are not shown in the figure for clarity. This is related to the higher-order harmonics of the reset systems, and several strategies are available to reduce this effect [8, 17, 18].

To minimize the low-frequency gain loss, the maximal possible value of ω_r should be selected, as suggested by Fig. 7.5a. Fig. 7.7 compares the BLA of FORE with different combinations of ω_r and γ, leading to the same phase lead in DF at ω_t. Selecting γ closer to 0 leads to stronger resets, and the same phase lead can be achieved with a narrower CgLp. Although the differences are small, it can be seen that with $\gamma = 0.4$, the gain loss in the low-frequency region is minimized. Explaining why this combination of values leads to the best results should be a subject of further study.

The results presented above indicate the tradeoff between the phase provided by CgLp and the gain loss at lower frequencies. For given γ, CgLp designed for larger phase lead at target frequency should be wider, requiring smaller ω_r. Lower ω_r leads to larger gain loss, leading to deterioration of systems performance.

The CgLp for closed-loop simulations is designed with only 5° phase lead, limiting gain loss and still providing damping of the BLS resonance peak. The corresponding corner frequency is $\omega_r = 380$ Hz. The maximal possible ω_f, limited by the Nyquist frequency, is selected, such that it has minimal influence on the phase lead at ω_t. For the shaping filter, a band-pass filter with $Q = 0.5$ is selected as it results in a close match between the BLA and DF at the frequency of interest, as indicated in Fig. 7.6b.

7.6 Closed-loop transmissibility analysis

In Fig. 7.8, the transmissibility relationships from closed-loop simulations with different controllers are compared with DF-based prediction. In the absence of a shaping filter ($Q = 0$), the BLA of the transmissibility matches closely the DF at low frequency. However,
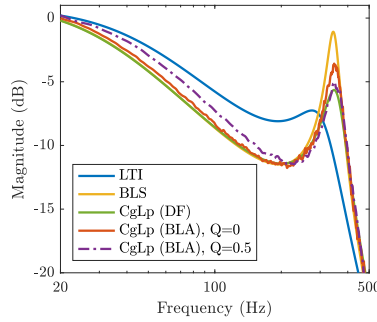
Figure 7.8: Closed-loop transmissibility for different controller designs. DF-based vs. BLA for no BPF and BPF with Q = 0.5

the resonance peak close to ω_t is greater than expected, which corresponds to lesser phase provided by the element (Fig. 7.6b).

Shaping the reset triggering signal with the tuned band-pass filter (Q = 0.5) results in stronger resonance peak reduction and a close match with the DF prediction around the resonance peak. This is at the cost of an increase in transmissibility at low frequency compared to the DF, due to the magnitude loss of FORE in that range of frequencies.

Both the magnitude loss and damping can be well explained using the BLA of the FORE from the open-loop simulation. At the same time, accurate prediction of the closed-loop results, based on the open-loop BLA of a reset element, remains challenging. Modifying the reset element influences the PSD of the reset triggering signal, as indicated in eq. (7.10). Improved damping due to better design of the reset element will reduce the magnitude of the response at the targetted frequency range, possibly increasing the influence of the components at other frequencies on the reset sequence. Moreover, due to the nonlinearity, the dynamics of a reset element are not fully captured by a BLA. Nevertheless, in the presented case, using the estimations based on open-loop BLA provided valuable insight for designing an improved system.

7.7 Discussion and Conclusions

The aim of this paper was to enable the rational design of reset control systems in the presence of wide-band excitation. To this end, we proposed a design approach based on the analysis of power spectral densities of the signals in the system and the use of Best Linear Approximations of reset elements. In the presented case, the analysis of the PSD of the reset triggering signal revealed that low-frequency components dominated it, causing different behaviour than expected based on the DF analysis. To benefit from the reset element, the components at the cross-over frequency should dominate the reset triggering signal. To ensure this, a band-pass shaping filter was implemented.

Forcing the resetting at a specific frequency has an influence on other frequency ranges, which can be represented by a BLA of a reset element. At lower frequencies, the gain of the element decreases, which can be, to some extent, mitigated by adjusting the parameters of

the shaping filter and the reset element. At higher frequencies, the harmonics of the reset-ting frequency dominate the elements response. Closed-loop simulations showed that the damping performance at the resonance frequency was consistent with the expectations based on DF analysis. This demonstrates that by shaping the reset triggering signal, the benefits of the reset control can be realized, even in the presence of wide-band excitation.

Significant work is still required to make the design approach proposed here well-founded and reliable. While we show the potential of using the BLA to represent reset systems in the frequency domain, much more insight can still be gained. Moreover, the use of different control structure architectures, for example, including reset and LTI elements in parallel, should also be explored.

7

References

[1] S. Skogestad and I. Postlethwaite, *Multivariable Feedback Control - Analisys and design*, vol. 1. Hoboken, NJ: John Wiley, 2 ed., 2005.

[2] Y. Zheng, Y. Chait, C. V. Hollot, M. Steinbuch, and M. Norg, "Experimental demonstration of reset control design," *Control Engineering Practice*, vol. 8, pp. 113–120, 2 2000.

[3] Q. Chen, Y. Chait, and C. V. Hollot, "Analysis of reset control systems consisting of a fore and second-order loop," *Journal of Dynamic Systems, Measurement and Control, Transactions of the ASME*, vol. 123, no. 2, pp. 279–283, 2001.

[4] O. Beker, C. V. Hollot, and Y. Chait, "Plant with integrator: An example of reset control overcoming limitations of linear feedback," *IEEE Transactions on Automatic Control*, vol. 46, pp. 1797–1799, 11 2001.

[5] D. Wu, G. Guo, and Y. Wang, "Reset integral-derivative control for HDD servo systems," *IEEE Transactions on Control Systems Technology*, vol. 15, pp. 161–167, 1 2007.

[6] G. Zhao, D. Nešić, Y. Tan, and C. Hua, "Overcoming overshoot performance limitations of linear systems with reset control," *Automatica*, vol. 101, pp. 27–35, 2019.

[7] N. Karbasizadeh, N. Saikumar, and S. H. HosseinNia, "Fractional-order single state reset element," *Nonlinear Dynamics*, vol. 104, pp. 413–427, 3 2021.

[8] N. Karbasizadeh, A. A. Dastjerdi, N. Saikumar, D. Valerio, and S. H. Hossein Nia, "Benefiting from linear behaviour of a nonlinear reset-based element at certain frequencies," in *2020 Australian and New Zealand Control Conference, ANZCC 2020*, pp. 226–231, Institute of Electrical and Electronics Engineers Inc., 11 2020.

[9] D. Caporale, L. F. van Eijk, N. Karbasizadeh, S. Beer, D. Kostic, and S. H. HosseinNia, "Practical Implementation of a Reset Controller to Improve Performance of an Industrial Motion Stage," *IEEE Transactions on Control Systems Technology*, vol. PP, pp. 1–12, 2024.

[10] K. R. Krishnan and I. M. Horowitz, "Synthesis of a non-linear feedback system with significant plantignorance. For prescribed system tolerances," *International Journal of Control*, vol. 19, no. 4, pp. 689–706, 1974.

[11] I. Horowitz and P. Rosenbaum, "Non-linear design for cost of feedback reduction in systems with large parameter uncertainty," *International Journal of Control*, vol. 21, no. 6, pp. 977–1001, 1975.

[12] L. Hazeleger, M. Heertjes, and H. Nijmeijer, "Second-order reset elements for stage control design," in *Proceedings of the American Control Conference*, vol. 2016-July, pp. 2643–2648, Institute of Electrical and Electronics Engineers Inc., 7 2016.

[13] O. Beker, C. V. Hollot, Y. Chait, and H. Han, "Fundamental properties of reset control systems," *Automatica*, vol. 40, pp. 905–915, 6 2004.

7

[14] N. Saikumar, R. K. Sinha, and S. Hassan Hosseinnia, "'Constant in Gain Lead in Phase' Element-Application in Precision Motion Control," *IEEE/ASME Transactions on Mechatronics*, vol. 24, pp. 1176–1185, 6 2019.

[15] N. Saikumar, K. Heinen, and S. H. HosseinNia, "Loop-shaping for reset control systems: A higher-order sinusoidal-input describing functions approach," *Control Engineering Practice*, vol. 111, p. 104808, 6 2021.

[16] P. W. J. M. Nuij, O. H. Bosgra, and M. Steinbuch, "Higher-order sinusoidal input describing functions for the analysis of non-linear systems with harmonic responses," *Mechanical Systems and Signal Processing*, vol. 20, pp. 1883–1904, 2006.

[17] N. Karbasizadeh, A. A. Dastjerdi, N. Saikumar, and S. H. HosseinNia, "Band-Passing Nonlinearity in Reset Elements," 9 2020.

[18] N. Karbasizadeh and S. H. HosseinNia, "Continuous reset element: Transient and steady-state analysis for precision motion systems," *Control Engineering Practice*, vol. 126, p. 105232, 9 2022.

[19] X. Zhang, M. B. Kaczmarek, and S. H. HosseinNia, "Frequency-domain analysis for reset systems using pulse-based model," *ArXive preprint*, 2022.

[20] A. A. Dastjerdi, A. Astolfi, N. Saikumar, N. Karbasizadeh, D. Valerio, and S. H. Hosseinnia, "Closed-Loop Frequency Analysis of Reset Control Systems," *IEEE Transactions on Automatic Control*, vol. 68, pp. 1146–1153, 2 2023.

[21] A. Barreiro and A. Bãnos, *Reset Control Systems.* London: Springer-Verlag, 2012.

[22] Y. Guo, L. Xie, and Y. Wang, *Analysis and design of reset control systems.* Institution of Engineering and Technology, 1 2016.

[23] C. Prieur, I. Queinnec, S. Tarbouriech, and L. Zaccarian, "Analysis and synthesis of reset control systems," *Foundations and Trends in Systems and Control*, vol. 6, no. 2-3, pp. 119–338, 2018.

[24] J. Carrasco, A. Baños, and A. van der Schaft, "A passivity-based approach to reset control systems stability," *Systems and Control Letters*, vol. 59, pp. 18–24, 1 2010.

[25] M. B. Kaczmarek and S. H. HosseinNia, "Negative Imaginary Reset Control Systems," *IEEE Transactions on Automatic Control*, pp. 1–6, 2024.

[26] Y. Guo, Y. Wang, and L. Xie, "Frequency-domain properties of reset systems with application in hard-disk-drive systems," *IEEE Transactions on Control Systems Technology*, vol. 17, no. 6, pp. 1446–1453, 2009.

[27] K. Heinen, "Frequency analysis of reset systems containing a clegg integrator: An introduction to higher order sinusoidal input describing functions," 2018.

[28] Lieve Lauwers, *Some practical applications of the best linear approximation in nonlinear block-oriented modelling.* PhD thesis, 2011.

7

[29] D. Rijlaarsdam, P. Nuij, J. Schoukens, and M. Steinbuch, "A comparative overview of frequency domain methods for nonlinear systems," *Mechatronics*, vol. 42, pp. 11–24, 2017.

[30] A. Pavlov, A. Pogromsky, N. Van De Wouw, and H. Nijmeijer, "Convergent dynamics, a tribute to Boris Pavlovich Demidovich," *Systems & Control Letters*, vol. 52, pp. 257–261, 2004.

[31] R. Pintelon, M. Schoukens, and J. Lataire, "Best Linear Approximation of Nonlinear Continuous-Time Systems Subject to Process Noise and Operating in Feedback," *IEEE Transactions on Instrumentation and Measurement*, vol. 69, pp. 8600–8612, 10 2020.

[32] S. T. Spanjer and W. B. Hakvoort, "Optimal Active Vibration Isolation System Design using Constrained H2control.," in *IFAC-PapersOnLine*, vol. 55, pp. 160–165, Elsevier, 1 2022.

[33] M. J. Balas, "Direct Velocity Feedback Control of Large Space Structures," *Journal of Guidance and Control*, vol. 2, pp. 252–253, 5 1979.

7

8

Negative Imaginary Reset Control Systems

Chapter 7 investigated the use of reset controllers in AVC to relax the limitations of LTI systems. One of the challenges in the reset control is proving the stability of a control system based on the measured frequency response of the plant. In this chapter, to address this challenge, the Negative Imaginary (NI) systems theory is extended to a class of reset systems. The NI properties of LTI systems, analogous to positive real systems, can be concluded based on the frequency response. This knowledge is sufficient to conclude the stability of a reset control system using the theorems presented in this chapter.

Negative Imaginary Reset Control Systems

Abstract *In this note, we present an extension of the nonlinear negative imaginary (NI) systems theory to reset systems. We define the reset negative imaginary (RNI) and reset strictly negative imaginary (RSNI) systems and provide a state-space characterization of these systems in terms of linear matrix inequalities. Subsequently, we establish the conditions for the internal stability of a positive feedback interconnection of a (strictly) negative imaginary linear time-invariant plant and a reset (strictly) negative imaginary controller. The applicability of the proposed method is demonstrated in a numerical example of a reset version of a positive position feedback (PPF) controller for a plant with resonance.*

8.1 Introduction

Negative-Imaginary (NI) systems theory, introduced in [1, 2], offers a framework for stability analysis of energy-dissipating systems that do not fit within the classical dissipativity framework. A prominent application of this theory is found in flexible mechanical structures with collocated force actuators and position sensors. In these systems, energy is associated with the output and its derivative, and they exhibit passivity from the input to the derivative of the output.

For linear time-invariant (LTI) systems, the NI systems theory is well developed. The necessary and sufficient conditions for a system to exhibit the NI and strictly NI (SNI) properties are formulated in terms of both frequency responses and linear matrix inequalities (LMI) for state-space matrices [1–4]. The class of Output Negative Imaginary (ONI) systems, that unifies the existing subclasses of the NI systems class was introduced in [5]. The relationship between the NI properties of LTI systems and the dissipativity theory has been studied in [6–8]. The stability conditions for a positive feedback interconnection of a NI and strictly NI system involve only the open-loop steady-state gain of the system [1], hence robust stability can be guaranteed for systems with uncertain dynamics and lightly-damped resonances. Thanks to this property, the LTI NI framework found wide adoption in the field of active vibration control of flexible structures [9].

The NI systems theory was extended to Lipschitz continuous nonlinear systems in [10–13], using the dissipativity theory. Two stronger notions of the NI property for nonlinear systems were introduced, namely the weakly strictly nonlinear negative imaginary (WS-NNI) property [11] and the nonlinear output strictly negative-imaginary (OSNI) property [12, 13]. The conditions for the closed-loop stability of a positive feedback interconnection of two nonlinear NI systems were derived. The notion of linear time-varying NI systems was introduced in [14].

The existing nonlinear NI systems theory does not accommodate hybrid systems with state jumps. Among such systems, reset systems [15–17] are being rapidly developed

and show potential for wide adoption in the industry for control of LTI plants, which can be explained using two arguments. Firstly, reset control systems have been shown to overcome the inherent limitations of LTI systems, as evidenced by numerous studies, particularly in the field of precision motion control [18–22]. Secondly, the design of reset control systems can be conducted in the frequency domain using the describing function approximation [23–26], following a procedure analogous to the design of commonly employed LTI controllers. This represents a significant advantage compared to other types of nonlinear controllers.

However, the stability analysis of reset control systems often requires parametric models of both the controller and the plant [15, 27], which in practice may be hard to obtain. Although specific frequency-domain methods exist, their applicability is limited to low-order systems [28–30] or systems with less common reset conditions [31]. Establishing the stability of reset control systems can be achieved through the passivity theory [32], yet the NI systems theory would be better suited to many applications, for example, in the field of active vibration control.

In this note, we extend the nonlinear NI systems theory to reset systems. In this way, we address the challenges related to assessing the stability of reset control systems for LTI plants. We achieve this with the following three contributions.

- We introduce definitions of reset NI (RNI) and reset strictly NI (RSNI) systems. This is necessary, as the reset systems do not fit existing definitions of NI properties.

- We provide the necessary and sufficient conditions for a reset system to be RNI (RSNI), analogue to the NI Lemma for LTI systems [3]. In consequence, it can be easily checked if a system possesses the RNI (RSNI) properties.

- We show that a positive feedback interconnection of an SNI (NI) LTI plant with an RNI (RSNI) reset controller is internally stable under some conditions.

The applicability of the stability result is illustrated with an example of a reset positive position feedback (PPF) [33] controller for a plant with resonance, commonly used to model mechanical systems.

8

The structure of the note is as follows: Section 8.2 provides preliminary information on LTI and nonlinear NI systems and reset control. The main contribution of the note is presented in Section 8.3. Section 8.4 illustrates the stability results with an example. The note is concluded in Section 8.5.

8.2 Preliminaries

In this section, we present the studied control system, including the considered class of reset systems. Moreover, we recall the concepts of linear and nonlinear negative imaginary systems.

Notation

A^*	Complex conjugate transpose of the complex matrix A.
A^T	Transpose of the matrix A.
$A > 0$	The matrix A is positive definite.
$A \geq 0$	The matrix A is positive semidefinite.
$\Re\{s\}$	Real part of the complex number s.
$\lambda_{max}(A)$	Maximum eigenvalue of the matrix A.

8.2.1 System description

We focus on the control architecture presented in Fig. 8.1. A positive feedback interconnection is used to follow the conventions of the NI systems theory. The closed-loop system consists of a liner time-invariant (LTI) plant and a reset controller. The plant is described by

$$G : \begin{cases} \dot{x}(t) = Ax(t) + Bu(t), \\ y(t) = Cx(t) + Du(t), \end{cases} \tag{8.1}$$

where $x \in \mathbb{R}^n$, $u \in \mathbb{R}^m$, $y \in \mathbb{R}^m$, and A, B, C, D are constant matrices of appropriate dimensions. The plant (8.1) has the $m \times m$ real-rational proper transfer function $G(s) := C(sI - A)^{-1}B + D$, which is said to be strictly proper if $G(\infty) = D = 0$.

The state-space representation of the reset element is

$$R : \begin{cases} \dot{x}_r(t) = A_r x_r(t) + B_r u_r(t), & \rho(t) \neq 0, \\ x_r(t^+) = A_\rho x_r(t), & \rho(t) = 0 \ , \\ y_r(t) = C_r x_r(t) + D_r u_r(t) \end{cases} \tag{8.2}$$
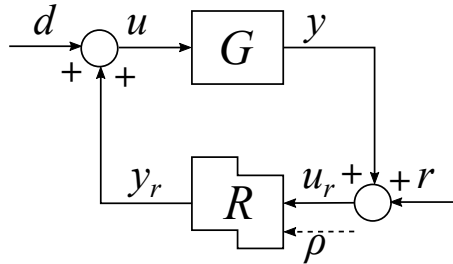

Figure 8.1: A positive feedback interconnection.

where $x_r \in \mathbb{R}^{n_r}$ is the state of R, $x_r(t^+) = x_r^+ = \lim_{\epsilon \to 0^+} x(t + \epsilon)$ is the after reset state value, $u_r \in \mathbb{R}^m$ is the input of R, $y_r \in \mathbb{R}^m$ is the output of R and A_r, B_r, A_ρ, C_r, D_r are constant matrices of appropriate dimensions.

The base linear system (BLS) R_{bls} is an LTI system with a state-space realization (A_r, B_r, C_r, D_r) and describes dynamics of R in the absence of reset.

The reset is triggered by a signal $\rho(t)$. The linear reset law $x_r^+ = A_\rho x_r(t)$ describes the change of state that occurs at reset instants t_k, $k = 1, 2, \ldots$, that is when the reset condition $\rho = 0$ is satisfied.

The closed-loop system, in the absence of external inputs d, r and assuming that $DD_r = 0$, is given by

$$\begin{cases} \dot{x}_{CL}(t) = A_{CL}x_{CL}(t), & x_{CL}(t) \notin \mathcal{M}(t) \\ x_{CL}(t^+) = A_R x_{CL}(t), & x_{CL}(t) \in \mathcal{M}(t) \\ y_{CL}(t) = C_{CL}x_{CL}(t) \end{cases} \tag{8.3}$$

where $x_{CL} = \begin{bmatrix} x & x_r \end{bmatrix}^T$, the reset surface $\mathcal{M}(t)$ defines states triggering reset and is defined

$$\mathcal{M}(t) = \{\xi \in \mathbb{R}^{n+n_r} : \rho(t) = 0, (I - A_R)\xi \neq 0\}, \tag{8.4}$$

and

$$A_{CL} = \begin{bmatrix} A + BD_rC & BC_r \\ B_rC & A_r + B_rDC_r \end{bmatrix}, \qquad A_R = \begin{bmatrix} I & 0 \\ 0 & A_\rho \end{bmatrix}, \qquad C_{CL} = \begin{bmatrix} C & DC_r \end{bmatrix}.$$

The ordered set of reset time instants is

$$\mathcal{T}(x_0) \triangleq \{t_i \in \mathbb{R} : t_i < t_{i+1}; x_{CL} \in \mathcal{M}(t_i), i \in \mathbb{N}\}. \tag{8.5}$$

Note that, different from most available results, the subsystems may have multiple inputs and outputs and are not assumed to be strictly proper.

The stability of the unforced system can be concluded using the Lyapunov-like condition.

Theorem 1 ([27]). *Let $V(x) : \mathbb{R}^{n+n_r} \to \mathbb{R}$ be a continuously-differentiable, positive-definite unbounded function such that*

$$\dot{V}(x) \triangleq \left[\frac{\partial V}{\partial x}\right] A_{CL}x_{CL} < 0, x_{CL} \neq 0, \tag{8.6}$$

$$\Delta V \triangleq V(A_R x_{CL}) - V(x_{CL}) \leq 0, x_{CL} \in \mathcal{M}. \tag{8.7}$$

Then,

1. *there is a left-continuous function $x_{CL}(t)$ satisfying (8.3) for all $t \geq 0$,*

2. *the equilibrium point $x_{CL} = 0$ is globally uniformly asymptotically stable.*

In practice, the existence and uniqueness of the solution of reset systems are assured by time-regularization [34, 35]. Time-regularization is a modification of reset system, such that reset instants happen only if a minimum time between resets $\Delta_m > 0$ has lapsed. Any discrete-time implementation inherently features time regularization with Δ_m equal to the sampling time [36]. Therefore, in the remainder of this note, it is assumed that solutions of R are well defined [15].

8

8.2.2 Negative Imaginary Systems

Below, to make this note self-contained, we summarize key results from the literature on the negative imaginary systems theory.

8.2.2.1 LTI systems

Definition 2 ([1, 3]). *A square transfer matrix $G(s)$ is negative imaginary (NI) if*

1. $G(s)$ *has no pole at the origin and in $\Re\{s\} > 0$;*

2. $j(G(j\omega) - G^*(j\omega)) \geq 0$ *for all $\omega \in (0, \infty)$ such that $j\omega$ is not a pole of $G(s)$;*

3. *If $j\omega_0, \omega_0 \in (0, \infty)$ is a pole of $G(s)$, it is at most a simple pole and the residue matrix $K_0 = \lim_{s \to j\omega_0}(s - j\omega_0)jG(s)$ is positive semi-definite Hermitian.*

Definition 3 ([1]). *A square real-rational proper transfer function matrix $G(s)$ is strictly negative imaginary (SNI) if*

1. $G(s)$ *has no poles in $\Re\{s\} \geq 0$;*

2. $j(G(j\omega) - G^*(j\omega)) > 0$ *for all $\omega \in (0, \infty)$.*

In the single-input single-output (SISO) case, a transfer function is NI if and only if it has no poles in the open right half plane or the origin and its phase is in $[-180°, 0°]$ at all frequencies.

Lemma 4 ([4]). *Let (A, B, C, D) be a minimal state-space realization of transfer function matrix $G(s)$. Then, $G(s)$ is negative imaginary if and only if $\det(A) \neq 0, D = D^T$ and there exist matrices $P = P^T > 0, W \in \mathbb{R}^{m \times m}$ and $L \in \mathbb{R}^{m \times n}$ such that the following LMI is satisfied:*

$$\begin{bmatrix} PA + A^T P & PB - A^T C^T \\ B^T P - CA & -(CB + B^T C^T) \end{bmatrix} = \begin{bmatrix} -L^T L & -L^T W \\ -W^T L & -W^T W \end{bmatrix} \leq 0. \tag{8.8}$$

Remark 5 ([3]). *The linear matrix inequality (8.8) can be simplified to $AP + PA^T \leq 0$ and $B + APC^T = 0$.*

Lemma 6 ([3]). *Let (A, B, C, D) be a minimal state-space realization of transfer function matrix $G(s)$. Then $G(s)$ is strictly negative imaginary if and only if:*

1. $\det(A) \neq 0, D = D^T$;

2. *there exists a matrix $P = P^T > 0, P \in \mathbb{R}^{n \times n}$, such that $AP + PA^T \leq 0$ and $B + APC^T = 0$.*

3. *the transfer function matrix $M(s) \sim LP^{-1}A^{-1}(sI - A)^{-1}B$ has full column rank at $s = j\omega$ for any $\omega \in (0, \infty)$, where $L^T L = -AP - PA^T$.*

8.2.2.2 Nonlinear systems

Consider now the MIMO nonlinear system of the form

$$\begin{cases} \dot{x} = f(x, u), \\ y = h(x), \end{cases} \tag{8.9}$$

where $f : \mathbb{R}^n \times \mathbb{R}^m \to \mathbb{R}^n$ is a Lipschitz continuous function and $h : \mathbb{R}^n \to \mathbb{R}^m$ is continuously differentiable function such that $h(0) = 0$. Note that the reset system (8.2) does not fit in this definition.

Definition 7 ([11]). *The system (8.9) is nonlinear negative imaginary (NNI) if there exists a positive definite continuously differentiable storage function $V : \mathbb{R}^n \to \mathbb{R}$ such that*

$$\dot{V}(x(t)) \leq \dot{y}(t)^T u(t), \forall t \geq 0. \tag{8.10}$$

The dissipative inequality of the Definition 7 can also be given in the integral equivalent form

$$V(x(t)) \leq V(x(t_0)) + \int_0^t \dot{y}^T(\tau) u(\tau) \mathrm{d}\tau, \forall t \geq 0. \tag{8.11}$$

Note, that the supply rate used in the definition of an NNI system involves a derivative of the output of the system. This is a major difference when compared with the definition of passive systems. There exist also stronger notions of the NNI properties that are used in the stability analysis of feedback systems.

Definition 8 ([11]). *The system (8.9) is marginally strictly nonlinear negative imaginary (MS-NNI) if the dissipativity inequality (8.11) is satisfied, and in addition, if u, x are such that*

$$\dot{V}(x) = \dot{y}^T(t) u(t) \quad \forall t > 0, \tag{8.12}$$

then $\lim_{t \to \infty} u(t) = 0$.

Definition 9 ([11]). *The system (8.9) is said to be weakly strictly nonlinear negative imaginary (WS-NNI) if it is MS-NNI and globally asymptotically stable when $u \equiv 0$.*

For an LTI system (8.1) the NNI property reduces to the NI property and the WS-NNI property reduces to the SNI property. This equivalence has been shown for systems with the feedthrough term $D = 0$ in [10, 11]. The relationship between dissipativity and the NI property is also explored in [6, 7]. Note that the notions MS-NNI and WS-NNI are restrictive due to the constraint on the input signal $u(t)$ included in their definitions.

8

8.3 Nonlinear Negative Imaginary Reset Systems

In this section, we present the contribution of this note. The reset system (8.2) does not fit in the definition (8.9). Therefore, we propose a new suitable definition of the NI property, enforcing that the storage function does not increase due to the reset actions. Subsequently, we provide two lemmas to characterize NI reset systems. Finally, we provide the internal stability theorem for closed-loop reset systems based on the introduced property.

Definition 10. *The system (8.2) is reset negative imaginary (RNI) if there exists a positive definite continuously differentiable storage function* $V : \mathbb{R}^{n_r} \to \mathbb{R}$ *such that*

$$\dot{V}(x_r(t)) \le \dot{y}_r(t)u_r(t), \quad t_k < t \le t_{k+1}, \tag{8.13}$$

$$\Delta V(x_r) = V(x_r(t_k^+)) - V(x_r(t_k)) \le 0, \quad t_k \in \mathcal{T}. \tag{8.14}$$

Definition 11. *The system (8.2) is reset strictly negative imaginary (RSNI) if it is RNI, and in addition, if* u_r, x_r *are such that*

$$\dot{V}(x_r) = \dot{y}_r^T(t)u_r(t) \quad \forall t > 0, \tag{8.15}$$

then $\lim_{t \to \infty} u_r(t) = 0$.

A reset system R is characterized by base linear dynamics R_{bls} and the reset law. Moreover, NNI properties are reduced to NI properties for LTI systems. Therefore, to conclude that a reset system R is RNI (RSNI) it is sufficient to show that R_{bls} is NI (SNI), which can be done using Lemmas 4 and 6, and assure that the storage function does not increase after reset. This is formally expressed in the following two lemmas.

Lemma 12. *Consider a reset system R defined by (8.2) with the base linear system R_{bls} being a minimal realization of a transfer function. Then, R is RNI if and only if there exists matrix* $P = P^T > 0$ *such that the conditions of Lemma 4 are satisfied by R_{bls} and* $A_\rho^T P A_\rho - P \le 0$.

Proof. The conditions related to the properties of the base linear system R_{bls} follow from the equivalence of the NI and the NNI properties for LTI systems and the Lemma 4 and its proof in [3]. Consider now the change of the quadratic storage function $V(x_r) = \frac{1}{2}x_r^T P x_r$ due to a reset

$$\Delta V(x_r) = \frac{1}{2}x_r^T(A_\rho^T P A_\rho - P)x_r,$$

which is non-positive for arbitrary x_r if and only if $A_\rho^T P A_\rho - P \le 0$, which is a condition of the lemma.   □

Lemma 13. *Consider a reset system R defined by (8.2) with the base linear system R_{bls} being a minimal realization of a transfer function. Then, R is RSNI if and only if there exists matrix* $P = P^T > 0$ *such that the conditions of Lemma 6 are satisfied by R_{bls} and* $A_\rho^T P A_\rho - P \le 0$.

Proof. The conditions related to the properties of the base linear system R_{bls} follow from the equivalence of the SNI and the WS-NNI properties for LTI systems and the Lemma 6 and its proof in [3]. The rest of the proof follows as in the previous lemma.   □

The feedback system presented in Fig. 8.1 consists of an LTI plant (8.1) and a reset controller (8.2). We have two possible cases: the interconnection of SNI plant and RNI controller or NI plant and RSNI controller. Additionally, it is possible to obtain results independent on the reset condition or to assume specific reset conditions. Stability results for some of the possible combinations are presented in separate theorems.

To be able to prove the stability, we introduce restrictions either on the structure of the reset controller or on the reset condition. This is necessary due to the structure of the Lyapunov functions used in the available literature for NI systems [37]. Nevertheless, the results we obtain are sufficiently general to design practical controllers. In Theorem 14, the structure of the reset controller is restricted to allow for the use of any reset condition. For example, the reset can be triggered by a signal from an additional shaping filter [30].

Theorem 14. *Consider an LTI SNI $G(s)$ with the minimal realization (8.1) and an RNI systems R defined by (8.2) with a base linear system $R_{bls}(s)$, such that $G(\infty)R_{bls}(\infty) = 0$ and $G(\infty) \geq 0$. Assume that the output of the reset system does not depend directly on the reset state $y_r(t_k^+) = y_r(t_k)$ (which means $C_r A_\rho = C_r$) and that $\lambda_{max}(G(0)R_{bls}(0)) < 1$. Then, the positive feedback interconnection of $G(s)$ and R is internally stable for any reset condition.*

Proof. Let $V_g(x) = x^T P_g x$ and $V_r(x_r) = x_r^T P_r x_r$, where $P_g = P_g^T > 0$, $P_r = P_r^T > 0$ are matrices of appropriate dimensions, and consider the Lyapunov candidate function for the feedback system

$$V(x, x_r) = x_{CL}^T \begin{bmatrix} P_g - C^T D_r C & -C^T C_r \\ -C_r^T C & P_r - C_r^T D C_r \end{bmatrix} x_{CL}.$$

From Lemma 4 in [37] we have that $V(x, x_r)$ is positive definite if and only if $\lambda_{max}(G(0)R_{bls}(0)) < 1$. In the proof of Theorem 1 in [37] we find that if the conditions on the subsystems stated here are satisfied, we have $\dot{V}(x, x_r) \leq 0$. This implies that the base linear system of the closed loop (8.3) is at least Lyapunov stable. Moreover, the authors of [37] show that the A_{CL} matrix does not have eigenvalues on the imaginary axis, which implies the asymptotic stability of the base linear system of (8.3).

To show the stability of the complete reset system, we consider the change of $V(x, x_r)$ due to the reset

$$\Delta V(x, x_r) = V(x, x_r^+) - V(x, x_r)$$
$$= x_{CL}^T \begin{bmatrix} 0 & -(C^T C_r A_\rho - C^T C_r) \\ -(A_\rho^T C_r^T C - C_r^T C) & A_\rho^T (P_r - C_r^T D C_r) A_\rho - (P_r - C_r^T D C_r) \end{bmatrix} x_{CL} \quad (8.16)$$
$$= -x_r^T (A_\rho^T C_r^T C - C_r^T C) x - x^T (C^T C_r A_\rho - C^T C_r) x_r$$
$$\quad + x_r^T A_\rho^T (P_r - C_r^T D C_r) A_\rho x_r - x_r^T (P_r - C_r^T D C_r) x_r$$

Using $C_r A_\rho = C_r$ we obtain

$$\Delta V(x, x_r) = x_r^T (A_\rho^T P_r A_\rho - P_r) x_r, \quad (8.17)$$

which, as can be seen in the Lemma 12, is smaller or equal to 0 for any x_r.   □

Remark 15. *The stability of a feedback connection of an LTI NI $G(s)$ and an RSNI R, assuming that the output of the reset system does not depend directly on the reset state, can be proven in analogue to the Theorem 14.*

Remark 16. *The requirement that the output of the reset system does not depend directly on the reset state $y_r(t_k^+) = y_r(t_k)$, which is equivalent to $C_r A_\rho = C_r$, is satisfied by any reset control system connected in series with an LTI low-pass filter. The complete series interconnection should then satisfy the conditions of the Lemma 12 in the case of the Theorem 14, or Lemma 13 if an LTI NI plant is considered.*

In Theorem 17, the classical zero-crossing reset condition is assumed to remove the restrictions on the structure of the controller.

Theorem 17. *Consider an LTI SNI $G(s)$ with the minimal realization (8.1) and an RNI systems R defined by (8.2) with a base linear system $R_{bls}(s)$, such that $G(\infty)R_{bls}(\infty) = 0$ and $G(\infty) \geq 0$. Assume the reset condition $\rho(t) = u_r(t)$ is set and that $\lambda_{max}(G(0)R_{bls}(0)) < 1$. Then, the positive feedback interconnection of $G(s)$ and R is internally stable.*

Proof. The first part of the proof, related to the base linear systems, is the same as in the proof of Theorem 14. Consider $\Delta V(x, x_r)$ given by (8.16). Using the knowledge of the reset condition at the reset instant we have $u_r(t_k) = y(t_k) = 0$, that is

$$y(t_k) = Cx(t_k) + D(C_r x_r(t_k) + D_r y(t_k)). \tag{8.18}$$

Using the assumption $G(\infty)R_{bls}(\infty) = DD_r = 0$ we have $Cx(t_k) = -DC_r x_r(t_k)$. Substituting to (8.16) we obtain

$$\Delta V(x, x_r) = -x_r^T \left((I - A_\rho^T)C_r^T DC_r (I - A_\rho) \right) x_r - x_r^T \left(A_\rho^T P A_\rho - P_r \right) x_r \tag{8.19}$$

which is smaller of equal to 0 for any x_r if R is RNI (see Lemma 12). $\qquad\square$

8.4 Illustrative examples

In this section, we demonstrate the applicability of the stability results by presenting an example of a reset controller for damping an LTI plant with a resonance that achieves a finite-time convergence.

The plant represented by a transfer function

$$G(s) = \frac{1/k}{s^2/\omega_0^2 + 2\zeta s/\omega_0 + 1} \tag{8.20}$$

can be seen as an approximation of a flexible mechanical structure with stiffness k, natural frequency ω_0 and damping ratio ζ. As a controller, a second-order reset element given by the (8.2) with

$$A_r = \begin{bmatrix} 0 & 1 \\ -\frac{7}{3}\omega_0^2 & -2\zeta\omega_0 \end{bmatrix}, \quad B_r = \begin{bmatrix} 0 \\ \omega_0^2 \end{bmatrix}, \quad A_\rho = \begin{bmatrix} 1 & 0 \\ 0 & 0 \end{bmatrix}, \quad C_r = \begin{bmatrix} \frac{4}{3}k & 0 \end{bmatrix}, \quad D_r = 0. \tag{8.21}$$
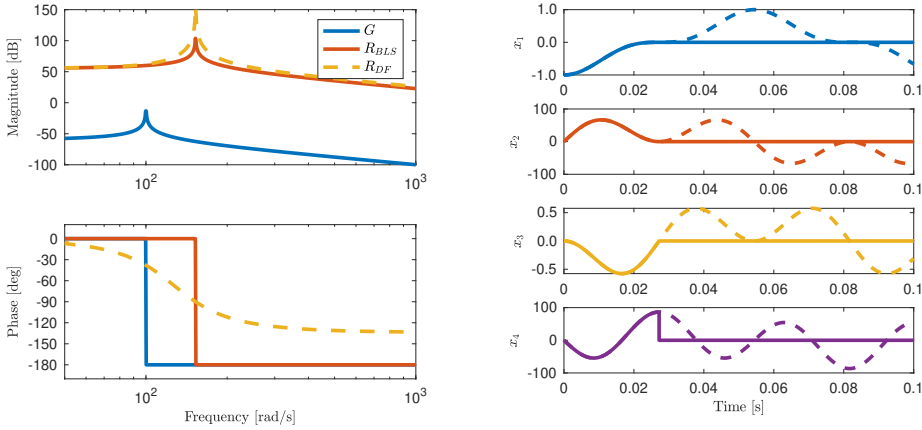
(a) Frequency response of the plant and the baseline system of the controller and describing function prescription of the reset controller.

(b) State trajectories for the closed-loop interconnection. Dashed lines correspond to the base-linear system and solid lines to the system with reset.

Figure 8.2: Frequency and time-domains simulation results for a reset control system.

and with reset triggered by the derivative of the input signal $\rho = \dot{u}_r$. The controller is a reset version of the positive position feedback (PPF) [33], commonly used in active vibration control, as the transfer function of the base linear system is

$$R_{bls}(s) = \frac{4k}{3s^2/\omega_0^2 + 6\zeta s/\omega_0 + 7}.$$

In the remainder of the paper, values $k = 10^3$, $\omega_0 = 10^2\,$rad/s and $\zeta = 10^{-6}$ are used for demonstration.

Figure 8.2a presents the frequency responses of the plant, the base-linear system of the controller and its describing function description [23]. Since the considered subsystems are SISO, we can conclude that the plant (8.20) is SNI. The same can be concluded for the base linear system of the controller. To show that the complete reset element is RNI, we use the linear matrix inequalities that follow from Lamma 12, which are satisfied by

$$P = \begin{bmatrix} 0.0003 & 0 \\ 0 & 7.5000 \end{bmatrix}.$$

For the reset controller we have $C_r A_\rho = C_r$, $|G(\infty)R_{bls}(\infty)| = 0$ and $|G(0)R_{bls}(0)| = 4/7$, so the stability can be concluded using the Theorem 14.

Figure 8.2b shows the state in response to initial condition $x_{CL}(0) = [-1 \quad 0 \quad 0 \quad 0]^T$ for the closed-loop interconnection for both the reset control system (solid lines) and its base linear dynamics (dashed lines). In the reset case, the state x_1, which corresponds to the position of the plant, converges 0 in finite time. This behaviour can be understood by observing that at the reset instant, the only non-zero state is the state to be reset. It can be said, all the energy of the system is associated with that state and is dissipated by the reset action. Similar effect can be seen in [38].

8.5 Conclusions

In this paper, the NI systems theory has been extended to a class of reset control systems. We introduced definitions for reset negative imaginary (RNI) and reset strictly negative imaginary (RSNI) systems. Moreover, we established necessary and sufficient conditions for a system to exhibit RNI and RSNI behaviours in the form of linear matrix inequalities. We considered positive feedback interconnections of an LTI plant and a reset controller and proven internal stability in the absence of external inputs in three different cases. Due to the structure of the Lyapunov functions used currently for NI systems, it was necessary to introduce restrictions either on the structure of the reset controller or on the reset condition. Relaxing these conditions is a remaining challenge. What is more, the definition of the RSNI system is based on the MS-NNI and, in consequence, also restrictive due to the conditions on the input signal. To increase the applicability of this result, finding an alterative definition for the RSNI would be necessary.

To exemplify the applicability of the derived stability results, we provide an illustration involving a flexible plant controlled by a second-order reset element. The obtained results can be used to show the stability of reset controllers providing finite-time convergence. The developed theory is important from a practical point of view since it allows us to conclude the stability of feedback systems consisting of a known nonlinear reset controller and an LTI plant without the need for a parametric model of the plant, as the NI properties may be concluded base on measured frequency response functions.

8

References

[1] A. Lanzon and I. R. Petersen, "Stability robustness of a feedback interconnection of systems with negative imaginary frequency response," *IEEE Transactions on Automatic Control*, vol. 53, pp. 1042–1046, 5 2008.

[2] I. R. Petersen and A. Lanzon, "Feedback Control of Negative-Imaginary Systems," *IEEE Control Systems*, vol. 30, no. 5, pp. 54–72, 2010.

[3] J. Xiong, I. R. Petersen, and A. Lanzon, "A Negative Imaginary Lemma and the stability of interconnections of linear negative imaginary systems," *IEEE Transactions on Automatic Control*, vol. 55, pp. 2342–2347, 10 2010.

[4] M. A. Mabrok, A. G. Kallapur, I. R. Petersen, and A. Lanzon, "Stability analysis for a class of negative imaginary feedback systems including an integrator," in *ASCC 2011 - 8th Asian Control Conference - Final Program and Proceedings*, pp. 1481–1486, 2011.

[5] P. Bhowmick and A. Lanzon, "Time-domain output negative imaginary systems and its connection to dynamic dissipativity," in *Proceedings of the IEEE Conference on Decision and Control*, vol. 2020-Decem, pp. 5167–5172, 2020.

[6] P. Bhowmick and S. Patra, "On LTI output strictly negative-imaginary systems," *Systems and Control Letters*, vol. 100, pp. 32–42, 2 2017.

[7] P. Bhowmick and A. Lanzon, "Output strictly negative imaginary systems and its connections to dissipativity theory," in *Proceedings of the IEEE Conference on Decision and Control*, vol. 2019-Decem, pp. 6754–6759, Institute of Electrical and Electronics Engineers Inc., 12 2019.

[8] A. Lanzon and P. Bhowmick, "Characterization of Input-Output Negative Imaginary Systems in a Dissipative Framework," *IEEE Transactions on Automatic Control*, vol. 68, pp. 959–974, 2 2023.

[9] I. R. Petersen, "Negative imaginary systems theory and applications," *Annual Reviews in Control*, vol. 42, pp. 309–318, 1 2016.

[10] A. G. Ghallab, M. A. Mabrok, and I. R. Petersen, "Extending Negative Imaginary Systems Theory to Nonlinear Systems," in *Proceedings of the IEEE Conference on Decision and Control*, vol. 2018-Decem, pp. 2348–2353, Institute of Electrical and Electronics Engineers Inc., 7 2018.

[11] A. G. Ghallab and I. R. Petersen, "Negative Imaginary Systems Theory for Nonlinear Systems: A Dissipativity Approach," *ArXive preprint*, 1 2022.

[12] K. Shi, I. G. Vladimirov, and I. R. Petersen, "Robust Output Feedback Consensus for Networked Identical Nonlinear Negative-Imaginary Systems," in *IFAC-PapersOnLine*, vol. 54, pp. 239–244, Elsevier, 1 2021.

[13] K. Shi, I. R. Petersen, and I. G. Vladimirov, "Nonlinear Negative Imaginary Systems with Switching," in *IFAC-PapersOnLine*, vol. 56, pp. 3936–3941, Elsevier, 1 2023.

8

[14] S. Kurawa, P. Bhowmick, and A. Lanzon, "Negative Imaginary Theory for a Class of Linear Time-Varying Systems," *IEEE Control Systems Letters*, vol. 5, no. 3, pp. 1001–1006, 2021.

[15] A. Barreiro and A. Bãnos, *Reset Control Systems.* London: Springer-Verlag, 2012.

[16] Y. Guo, L. Xie, and Y. Wang, *Analysis and design of reset control systems.* Institution of Engineering and Technology, 1 2016.

[17] C. Prieur, I. Queinnec, S. Tarbouriech, and L. Zaccarian, "Analysis and synthesis of reset control systems," *Foundations and Trends in Systems and Control*, vol. 6, no. 2-3, pp. 119–338, 2018.

[18] O. Beker, C. V. Hollot, and Y. Chait, "Plant with integrator: An example of reset control overcoming limitations of linear feedback," *IEEE Transactions on Automatic Control*, vol. 46, pp. 1797–1799, 11 2001.

[19] D. Wu, G. Guo, and Y. Wang, "Reset integral-derivative control for HDD servo systems," *IEEE Transactions on Control Systems Technology*, vol. 15, pp. 161–167, 1 2007.

[20] G. Zhao, D. Nešić, Y. Tan, and C. Hua, "Overcoming overshoot performance limitations of linear systems with reset control," *Automatica*, vol. 101, pp. 27–35, 2019.

[21] N. Karbasizadeh, A. A. Dastjerdi, N. Saikumar, D. Valerio, and S. H. Hossein Nia, "Benefiting from linear behaviour of a nonlinear reset-based element at certain frequencies," in *2020 Australian and New Zealand Control Conference, ANZCC 2020*, pp. 226–231, Institute of Electrical and Electronics Engineers Inc., 11 2020.

[22] N. Karbasizadeh, N. Saikumar, and S. H. HosseinNia, "Fractional-order single state reset element," *Nonlinear Dynamics*, vol. 104, pp. 413–427, 3 2021.

[23] Y. Guo, Y. Wang, and L. Xie, "Frequency-domain properties of reset systems with application in hard-disk-drive systems," *IEEE Transactions on Control Systems Technology*, vol. 17, no. 6, pp. 1446–1453, 2009.

[24] N. Saikumar, K. Heinen, and S. H. HosseinNia, "Loop-shaping for reset control systems: A higher-order sinusoidal-input describing functions approach," *Control Engineering Practice*, vol. 111, p. 104808, 6 2021.

[25] A. A. Dastjerdi and S. H. Hosseinnia, "A Frequency-Domain Tuning Method for a Class of Reset Control Systems," *IEEE Access*, vol. 9, pp. 40950–40962, 2021.

[26] X. Zhang, M. B. Kaczmarek, and S. H. HosseinNia, "Frequency response analysis for reset control systems: Application to predict precision of motion systems," *Control Engineering Practice*, vol. 152, p. 106063, 11 2024.

[27] O. Beker, C. V. Hollot, Y. Chait, and H. Han, "Fundamental properties of reset control systems," *Automatica*, vol. 40, pp. 905–915, 6 2004.

8

[28] C. V. Hollot, Y. Zheng, and Y. Chait, "Stability analysis for control systems with reset integrators," in *Proceedings of the IEEE Conference on Decision and Control*, vol. 2, pp. 1717–1719, IEEE, 1997.

[29] A. A. Dastjerdi, A. Astolfi, and S. H. Hosseinnia, "A Frequency-Domain Stability Method for Reset Systems," in *Proceedings of the IEEE Conference on Decision and Control*, vol. 2020-Decem, pp. 5785–5791, Institute of Electrical and Electronics Engineers Inc., 12 2020.

[30] A. A. Dastjerdi, A. Astolfi, and S. H. HosseinNia, "Frequency-domain stability methods for reset control systems," *Automatica*, vol. 148, p. 110737, 2 2023.

[31] S. J. L. M. van Loon, K. G. J. Gruntjens, M. F. Heertjes, N. van de Wouw, and W. P. M. H. Heemels, "Frequency-domain tools for stability analysis of reset control systems," *Automatica*, vol. 82, pp. 101–108, 8 2017.

[32] J. Carrasco, A. Baños, and A. van der Schaft, "A passivity-based approach to reset control systems stability," *Systems and Control Letters*, vol. 59, pp. 18–24, 1 2010.

[33] J. L. Fanson and T. K. Caughey, "Positive position feedback control for large space structures," *AIAA Journal*, vol. 28, pp. 717–724, 5 1990.

[34] D. Nesic, L. Zaccarian, and A. R. Teel, "Stability properties of reset systems," *Automatica*, vol. 44, no. 8, pp. 2019–2026, 2008.

[35] L. Zaccarian, D. Nešić, and A. R. Teel, "First order reset elements and the Clegg integrator revisited," *Proceedings of the 2005, American Control Conference, 2005.*, pp. 563–568 vol. 1, 2005.

[36] M. F. Heertjes, K. G. J. Gruntjens, S. J. L. M. van Loon, N. van de Wouw, and W. P. M. H. Heemels, "Experimental Evaluation of Reset Control for Improved Stage Performance," *IFAC-PapersOnLine*, vol. 49, no. 13, pp. 93–98, 2016.

[37] A. G. Ghallab, M. A. Mabrok, and I. R. Petersen, "Lyapunov-based Stability of Feedback Interconnections of Negative Imaginary Systems," in *IFAC-PapersOnLine*, vol. 50, pp. 3424–3428, Elsevier, 7 2017.

[38] R. T. Bupp, D. S. Bernstein, V. S. Chellaboina, and W. M. Haddad, "Finite settling time control of the double integrator using a virtual trap-door absorber," *IEEE Transactions on Automatic Control*, vol. 45, pp. 776–780, 4 2000.

8

9
Conclusion

This final chapter discusses the outcomes presented in this thesis, including the limitations and the possible improvements. The insights obtained during the work are also summarized and synthesized, leading to recommendations for new research directions.

9.1 Summary of the thesis

In the presented work, we explored the possibilities created by using frequency-domain loop-shaping techniques to design feedback controllers in AVC systems and active metamaterials for bandgap generation. In Chapter 2, the desired controller characteristics were derived based on the knowledge of plant dynamics and the desired closed-loop transfer functions. The approach was demonstrated in an experimental evaluation of an ultra-hard mount system.

The loop-shaping approach for AVC systems was further related to the design for bandgap in active metastructures in Chapter 3. We have shown that using sensors, actuators, and feedback control is a feasible strategy for bandgap generation in metamaterials. Thanks to the frequency-domain design approach, it is possible to obtain low-frequency bandgaps in practice without the meticulous, analytical modeling of all the details of the experimental setup.

To relate the bandgap generation in finite structures to the loop shaping, we used the approach based on modal expansion. We also assumed an infinite number of infinitesimally small transducer pairs placed on the structure. Chapter 4 showed that the number of transducers required for this approximation to be accurate is often low and is closely related to the dominant vibration mode in the targeted frequency range.

The fractional-order control was shown to be an effective way to explore new design opportunities in AVC and metamaterials. In Chapters 5 and 6, it was employed as a step towards the ideal controller dynamics dictated by the loop-shaping analysis. In the metamaterial case, the greater design freedom offered by FO systems led to results unachievable with standard second-order resonators or controllers, like the deep bandgaps, without introducing additional resonance peaks. The FO systems approach enabled analytical analysis of the system's behavior, which is not possible when high integer order systems represent similar dynamics.

The performance of AVC systems can be improved with reset control beyond the limitations bounding the LTI controllers, as demonstrated in Chapter 7. The challenges posed by wide-band disturbances and multiple lightly damped resonance peaks in the system dynamics were overcome by analyzing and filtering the reset triggering signal. We used the best linear approximations (BLA) of the nonlinear controller since the describing functions used in the loop-shaping for reset systems cannot completely represent the system's behavior.

To complete the frequency-domain design framework for reset systems in AVC, we extended the Negative Imaginary Systems theory to a class of reset systems in Chapter 8. The proposed theory allows the determination of the stability of the closed-loop reset control system based only on the knowledge of controller dynamics and the frequency response of the plant, which can be measured in experiments. We hope that the availability of such tools may facilitate the practical use of reset systems and enable the shift in research from the study of stability to performance improvements.

9

9.2 Discussion

In the following subsections, we relate the results presented above to the research gaps identified in the introduction of this thesis. We discuss the discoveries, limitations of the approach taken, and possible avenues of future research related to each of the issues considered in this work.

9.2.1 Presenting AVC in line with the current control practice

The frequency-domain loop-shaping, often used for controller design in motion-control applications, is also suitable for AVC controller design. The efficiency of this approach was shown for both the single-mode vibration isolation system and continuous structures with multiple resonance peaks and multiple input-output pairs. The approach can also be used to motivate the use of nonlinear controllers for AVC.

The presented approach is only effective for the initial system design. Such a design can be further improved using optimization techniques, especially in the case of LTI systems, when the response of a system can be easily calculated. Nevertheless, the frequency domain perspective can still provide the rationale behind specific designs and intuition as to why a certain result performs well (or not). Loop-shaping has the potential to be a universal approach for the rational design of dynamical systems, at least for motions with small amplitudes. The key points of the approach are that the system is presented as an interconnection of subsystems operating in feedback and that the specific requirements are defined at different frequency ranges. As such, it could also be used to design mechanical or electronic systems.

An example of a mechanical design motivated by loop-shaping could be a fractional-order resonator. Based on chapters 5 and 6, FO resonators are a promising solution for vibration attenuation and isolation. Could such a resonator be constructed as a component that may be added to an existing structure as an alternative to a conventional tuned mass damper? A possible solution would be to combine several smaller resonators, in an analogue to approximating FO transfer functions by high integer order systems. Alternatively, could such a device be constructed by leveraging the properties of viscoelastic materials, often modeled with FO dynamics? Would the practical use of such FO resonators lead to the benefits expected based on the theoretical derivations?

In the case of electronic systems, the frequency domain approach could be used for the practical design of shunt circuits for vibration control with piezoelectric transducers. Such a shunt system can be seen as a voltage-controlled current source, with the dynamics implemented in a digital controller. Abstracting away from electronics and focusing on the inputs and outputs of the system could make the analysis and design more accessible. The next step in this research direction would be to explore the link between switched shunts for AVC and reset control. There is a possibility of demonstrating the equivalence between systems with switched shunts, variable stiffness members and constant-in-gain, lead-in-phase reset controllers. Could the DF analysis, techniques for shaping nonlinearity, and insights from Chapter 7 be effectively used for the switched shunt circuit design? This approach could revitalize this neglected yet highly promising research field.

9.2.2 Connecting metamaterials and conventional AVC

When we started working on this topic, the idea of using sensors, actuators and feedback to change the dynamics of the systems, in this case by creating the bandgap, appeared evident to us. This, however, did not seem apparent in the field. Using feedback and control insights in metamaterials for vibration is effective and promising, yet it is underexplored. Presenting bandgap generation in active structures coherently with the rest of the control research is a contribution of this work.

The issue that often arises in discussions on metamaterials and bandgap is their definitions. In this work, our focus was not on creating metamaterials (fitting the scope of physics or material science), but on creating structures with a bandgap in their frequency response. When the bandgap is defined as attenuation of vibration transmissibility at a specific limited frequency range, using a lattice of repeated identical unit cells is not optimal for obtaining it.

Better results can be obtained with an optimization of the entire finite structure. The existing results from metamaterial research (including the ones presented in this thesis) could provide the rationale behind the design and decent initial design for the algorithms. Using non-collocated sensors and actuators may yield better results when considering a finite structure and a specific range of frequencies. Moreover, the techniques from active vibration isolation, like disturbance feedforward, should be related to bandgap generation and extended to continuous structures.

To improve the experimental results on bandgap generation presented in Chapter 3, attention should be paid to the electronics used to implement the feedback loops and techniques used for bandgap measurements. The noise greatly influences the bandgap generation in active systems, as in the approaches used so far, a controller with a high resonance peak is required. This may lead to amplification of disturbances appearing in the system and poor robustness, e.g. in the presence of time delays. To address this problem, it would be interesting to see if creating bandgaps with controllers without resonance peaks is possible.

While we have shown the potential of metamaterials with FO resonators, reset metamaterials are a topic we did not explore in this work. In the context of creating bandgaps with controllers with resonance peaks, reset elements do not appear well-suited, as the reset is a strong energy dissipation mechanism, and creating high resonance peaks in reset systems is often impossible. However, as reset allows for breaking the Bodes magnitude and phase relationship, new reset-based designs for bandgap generation may be possible.

9.2.3 Designing non-conventional AVC controllers with a systematic approach

Loop shaping allows the design of non-conventional, possibly non-linear controllers for AVC not purely by trial and error but in a rational manner. Optimization (which can be seen as automated trial and error) is still a key part of the design process and contributes greatly to the final performance improvements. However, its role is to fine-tune the initial design provided and well-understood by the designer. This understanding is crucial when debugging a control system in experimental implementation.

Reset control systems are an augmentation for linear control (not their replacement), making it possible to improve the performance not only of motion control systems but also

vibration isolation systems. The two problems in the design of reset systems are related to performance prediction and stability analysis. For each of these problems, we introduced new tools to the field.

The design tools for reset control systems provide only approximate results and offer limited possibilities for predicting the system's performance. The use of best linear approximations (BLA) proposed in this thesis provides yet another approximation that, together with the currently used tools, gives a more complete view of the system behavior. The use of BLA in the case of reset systems should be justified with theory, as the tool has been developed for a different class of systems. Moreover, the work presented in Chapter 7 is only the first attempt at using this approach, and a complete analysis of different types of reset architectures is still required.

In the case of the negative imaginary (NI) systems approach for stability analysis, it was clear that it would apply to reset systems. Therefore, we could directly work on formally extending the method to this class. The drawback of the method (similar to the dissipative approach) is that it forces restrictions on the structure of the control system to prove the stability formally. However, if the dissipative or NI approaches are applicable, they allow us to conclude stability in an elegant, simple and practical way (using a frequency-domain model of the plant), which is a big advantage compared to other methods suitable for reset systems. This should be considered when new reset control architectures are developed.

In reset control, we face a situation similar to the classical chicken and egg problems. On the one hand, the theory is not advanced, as it does not have practical applications. On the other hand, the use of existing tools in practice is often not justified by the theory. To advance the field, we had to accept the discomfort caused by this situation and proceed with work despite it. The same can be said of any other field of research in engineering.

9.2.4 Final remarks

The rapid advances in metamaterials research and the field of control, especially their possible implications for designing better mechatronic systems and improving active vibration control, inspired the research presented in this thesis. Although the problems studied within these disciplines share clear similarities, the insights gained from each have not been combined or fully exploited. With this thesis, we furthered the understanding of the connections between active vibration control, motion control and the metamaterials for bandgap generation. This allowed us to develop a new framework for the design of active metamaterials and advance the techniques for the design of reset controllers.

By introducing a common design approach, we facilitate the practical use of AVC, including the nonlinear control methods and active metamaterial-based techniques. Those approaches can be used to diminish the influence of the high-frequency resonances and disturbances, which currently limit the mechatronics systems' performance. Drawing inspiration from metamaterial research in machine component design could lead to the creation of compact, tuneable structures that effectively dampen vibrations while maintaining high stiffness. While often not directly visible, precision mechatronics systems profoundly influence our daily lives. Enhancing their performance can lead, for example, to more powerful and affordable computing devices (due to advancements in the semiconductor field) and more efficient transportation methods (thanks to improved manufacturing of propulsion and transmission systems).

Curriculum Vitæ

Marcin Brunon Kaczmarek

1994/03/24	Born in Poznań, Poland

Education
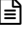
2020-2024	PhD. in Mechatronic System Design
	Department of Precision and Microsystems Engineering
	Delft University of Technology, Delft, The Netherlands
Dissertation:	Frequency-domain Design for Non-conventional Active Vibration Control
Promotors:	Dr. S.H. HosseinNia, Prof.dr.ir. J.L Herder
2017-2020	MSc. in Mechanical Engineering and MSc. in Systems and Control
	Department of Precision and Microsystems Engineering
	Delft Center for Systems and Control
	Delft University of Technology, Delft, The Netherlands
Thesis:	Hybrid Passivity and Finite-Gain Properties of Reset Systems
Supervisors:	*Dr. S.H. HosseinNia, Dr.ir. E. Steur*
2013-2017	BSc. in Mechatronics
	Faculty of Mechanical Engineering and Management
	Poznań University of Technology
Thesis:	The Electrohydraulic Workpiece Orienting System for a Machine Tool
Supervisor:	*Dr.inż. M. Pelic*
2010-2013	Lyceum ad Sanctam Mariam Magdalenam, Poznań

Experience
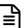
2024-Present	NVH Consultant
	Atlas Copco via Engibex, Antwerp, Belgium
2017-2017	Mechanical Engineer
	LAB Motion Systems, Leuven, Belgium

Publications published during the PhD project:

Journal publications:

5. **M.B. Kaczmarek**, S.H. HosseinNia, *Negative imaginary reset control systems*, IEEE Transactions on Automatic Control, 10.1109/TAC.2024.3487798, 2025. 📄

4. **M.B. Kaczmarek**, S.H. HosseinNia, *Creating bandgaps in active piezoelectric slender beams through positive position feedback control*, Smart Materials and Structures, 33 125039, 2024. 📄

3. X. Zhang, **M.B. Kaczmarek**, S.H. HosseinNia, *Frequency response analysis for reset control systems: Application to predict precision of motion systems*, Control Engineering Practice, 152, 106063, 2024.

2. **M.B. Kaczmarek**, S.H. HosseinNia, *Elastic metamaterials with fractional-order resonators*, Fractional Calculus and Applied Analysis 26 (6), 2522-2539, 2023. 📄

1. **M.B. Kaczmarek**, S.H. HosseinNia, *Fractional-order negative position feedback for vibration attenuation*, Fractal and Fractional 7 (3), 222, 2023. 📄

📄 Included in this thesis.

Peer-reviewed conference publications:

12. R.A.C. van den Berg, **M.B. Kaczmarek**, A. Natu, S.H. HosseinNia, *Reset control for active vibration isolation in the presence of wide-band disturbances*, Joint 10th IFAC Symposium on Mechatronic Systems and 14th Symposium on Robotics, 2025. 🗎

11. **M.B. Kaczmarek**, V. Gupta, S.H. HosseinNia, *Active Piezoelectric Metastructures: Relationship of Bandgap Formation with Unit Cell Number and Modal Behaviour*, ASME International Mechanical Engineering Congress & Exposition (IMECE), 2024. 🗎

10. **M.B. Kaczmarek**, V. Gupta, S.H. HosseinNia, *Bandgap modulation in active metamaterial beams through feedback control*, 2024 Eighteenth International Congress on Artificial Materials for Novel Wave Phenomena (Metamaterials), 2024.

9. M.J. Neele, **M.B. Kaczmarek**, J. Reiser, M. Winter, S.H. HosseinNia, *Experimental evaluation of ultra hard mount vibration control systems*, euspen's Special Interest Conference: Precision Motion Systems & Control, 2024. 🗎

8. C. Verhoog, **M.B. Kaczmarek**, M. van den Hurk, S.H. HosseinNia, *Optimal active damping of a wafer gripper in presence of multiple disturbances*, euspen's 24th International Conference & Exhibition, 2024.

7. A.M. Natu, **M.B. Kaczmarek**, S.H. HosseinNia *Overactuation for active damping in compliant positioning stage using piezoelectric transducers*, 4th IFAC Conference on Advances in Proportional-Integral-Derivative Control, 2024.

6. S.A. Hosseini, L.F. van Eijk, **M.B. Kaczmarek**, S.H. HosseinNia, *Higher-order sinusoidal-input describing function analysis of fractional-order hybrid integrator-gain systems*, 4th IFAC Conference on Advances in Proportional-Integral-Derivative Control, 2024.

5. V.F. Buskes, **M.B. Kaczmarek**, J.C. Veenstra, C. Coulais, S.H. HosseinNia, *Control architectures for metamaterials in vibration control*, IEEE International Conference on Mechatronics (ICM), 2023.

4. P.E. de Bruin, **M.B. Kaczmarek**, M. Kok, S.H. HosseinNia, *Evaluation of recursive Bayesian filters for modal contribution estimation in high-tech compliant mechanisms*, 22nd IFAC World Congress, 2023.

3. M. El Ajjaj, **M.B. Kaczmarek**, M.A.C.C. van den Hurk, S.H. HosseinNia, *Vibration suppression of a state-of-the-art wafer gripper*, euspen's Special Interest Group Meeting: Precision Motion Systems & Control, 2022.

2. **M.B. Kaczmarek**, X. Zhang, S.H. HosseinNia, *Steady-state nonlinearity of open-loop reset systems*, IEEE Conference on Control Technology and Applications (CCTA), 2022.

1. M.A. Mohan, **M.B. Kaczmarek**, S.H. HosseinNia, *Resetting velocity feedback: reset control for improved transient damping*, European Control Conference (ECC), 2022.

🗎 Included in this thesis.

MSc thesis projects supervised:

- R. van den Berg, *Reset control for active vibration isolation in the presence of wideband disturbances*, 2024.

- M.J. Neele, *Ultra hard mount active vibration control*, 2024.

- C. Verhoog, *Optimal active damping performance in presence of disturbance and electronic noise sources*, 2023.

- F. Coatto, *Metastructures in a sensor-actuator configuration: the practical issues in bandgap generation*, 2023.

- A.M. Natu, *Overactuation for active damping in compliant positioning stage using piezoelectric actuators*, 2023.

- S. Fan, *Data-based modal space control for active damping*, 2023.

- M. El Ajjaj, *Vibration suppression of a state-of-the-art wafer gripper*, 2022.

- G. Marega, *Mechanical design for out-of-plane mode attenuation in flexure mechanisms*, 2022.

- V. Buskes, *Distributed vibration control for robotic cantilever beams*, 2022.

- T. Kouwenhoven, *Design of a nonlinear stiffness unit cell aided magnetic gravity compensator*, 2022.

- P. de Bruin, *Input and state estimation for compliant motion stages*, 2022.

- L. Bosscher, *Hybrid vibration control with concurrent active piezoelectric and passive viscoelastic damping*, 2022.

- B. Rotteveel, *Active unit-cell structures for vibration control*, 2022.

- T. Godfroid, *Multiplexing piezo electric transducers to reduce the number of amplifiers in an AVC-system*, 2022.

- T. van der Graaf, *Active vibration control using distributed sensors and actuators*, 2021.

- H.I.M. Alhasni, *Adaptive multimodal damping of flexible structures*, 2021.

- M.A. Mohan, *Resetting velocity feedback: reset control for active damping*, 2021.

Acknowledgments